Fiber laser system for the detection of trace gas

By
Jonas Kestutis Valiunas

A dissertation submitted to the Faculty of Graduate Studies
Lakehead University
In partial fulfillment of the requirements for the degree of
Doctor of Philosophy
Chemistry and Materials Science

Department of Physics
Lakehead University
© Jonas Kestutis Valiunas 2017

Abstract

The research presented in this thesis is on the development of a trace gas detection system based on intracavity absorption spectroscopy (ICAS). The developed system was capable of detecting nitrous oxide (N_2O) and acetylene (C_2H_2) gas at sub-ppmv levels. The P (12) rotational line of N_2O at ~1522.20 nm, and the R (5) and R (4) rotational lines of C_2H_2 at ~1522.22 nm were used for detection. A fiber Bragg grating was incorporated into the ICAS cavity to enhance the system sensitivity by allowing the selection of strong absorption lines for detection. By operating the fiber laser based ICAS system at threshold, multiple circulations of the amplified spontaneous emission inside the cavity enhanced the system detection sensitivity. Further, the laser wavelength contained multi-longitudinal modes, which improved the system sensitivity. The system sensitivity was explored for two intra-cavity gas cells: a multi-pass Herriott cell and a gas cell based on a hollow-core photonic crystal fiber (HC-PCF). The system operated at room temperature and a polarization-maintaining erbium-doped fiber was used as a saturable absorber to help eliminate mode hopping in the laser cavity.

Publications and Contributions

PUBLICATIONS

Jonas K. Valiunas, Mario Tenuta, and Gautam Das, "A gas cell based on Hollow-Core Photonic Crystal Fiber (PCF) and its application for the detection of Greenhouse Gas (GHG): Nitrous Oxide (N_2O)", *Journal of Sensors*, vol. 2016, (2016).

Jonas K. Valiunas, George Stewart, and Gautam Das, "Detection of Nitrous Oxide (N_2O) at sub-ppmv using Intracavity Absorption Spectroscopy (ICAS)", *IEEE Photon. Technol. Lett.*, vol. 28, no. 3, pp. 359-362, 2016.

CONFRENCES

J. Valiunas and G. Das, "Detection of C_2H_2 at a concentration of ppmv levels using a fiber laser system", *CAP Conference, University of Ottawa, Ottawa*, 12-17 June, 2016.

G. Das and **J. Valiunas** " Detection of Greenhouse Gas (N2O) using Intracavity Absorption Spectroscopy (ICAS)", *CLEO 2016*, San Jose, USA, June 5-10, 2016.

J. Valiunas and G. Das, "Detection of Trace Gases using Fiber Laser Technology- Part 1", *CAP Congress, University of Alberta, Edmonton, Canada*, June 13 - 19, 2015.

J. Valiunas and G. Das, "Detection of Trace Gas (N2O) using Fiber Laser Technology", *CAP Congress, University of Alberta, Edmonton, Canada*, June 13 - 19, 2015.

To my nephew, Henri.

Acknowledgements

So much time and effort has been spent performing the research and compiling this dissertation, both of which would not have been possible if it was not for all the wonderful people which surround me.

I would like to first thank my supervisor, Professor Gautam Das, who gave me this great opportunity to pursue my PhD with the Photonics Research Group. I will be forever grateful for the motivation, encouragement, and endless hours he invested in helping me throughout these years of study.

Thank you to all the past and current members of the Photonics Research Group I had the pleasure of working with. My sincere thanks goes to Joshua Trevisanutto for helping to make sure my thesis was readable, and to Ivy Anderson for helping to collect soil gas samples on those horribly hot summer days.

I would like to express my gratitude to everyone in the Lakehead University Physics Department with a special thank to Kristine Carey for always being unbelievably helpful and to my committee members, Dr. Mark Gallagher and Dr. Apichart Linhananta.

A sincere thanks to Ray Dowbenko, Dr. Mario Tenuta, and Dr. Tarlok Sahota for the time spent teaching me about soil science and agriculture research and to Professor George Stewart for the helpful discussions on spectroscopy techniques.

Thank you to my wonderful family and the friends that help to fill my life with laughter and to Zachari Medendorp for starting me down this path all those years ago.

Finally, for my partners in crime, Kathleen Beda, Snowbell, and Dino, thank you for always being there when I need it and giving me your love, support, and company throughout these years.

Contents

List of Figures

XIII

List of Tables

Chapter 1

Introduction

Since Corning demonstrated the feasibility of a low loss optical fiber in 1970, passive and active optical components based on fibers have become the backbone of modern optical technology [1]. Their relatively low cost, low maintenance, and high chemical durability make optical fibers well suited for a number of applications including telecommunications, remote sensing, and medicine [2]. Despite the many potential applications, interest in this field has only truly started to grow in the last decades.

1.1   OPTICAL FIBER

In its simplest form, optical fiber is constructed from two concentric dielectric cylinders, one encompassing the other. The internal dielectric medium is referred to as the core and has a marginally higher index of refraction than the surrounding dielectric, known as the cladding (**Figure 1.1**). The slight contrast in the refractive indices allows light to be guided through the core of the fiber via total internal reflection. This simple type of fiber is referred to as a step-index fiber because of the abrupt change in the refractive index from the core to the cladding, which results in a refractive index profile resembling a step. One common method used to fabricate an optical fiber begins with the development of a glass preform by a vapor-

phase oxidation deposition and vitrification process. The resulting preform will have the glass composition of the desired fiber. The glass preform is then heated and drawn into the optical fiber, and covered in a protective layer [3]. The protective layer, referred to as the buffer, is typically a polymer coating and improves the overall flexibility and durability of the fiber.
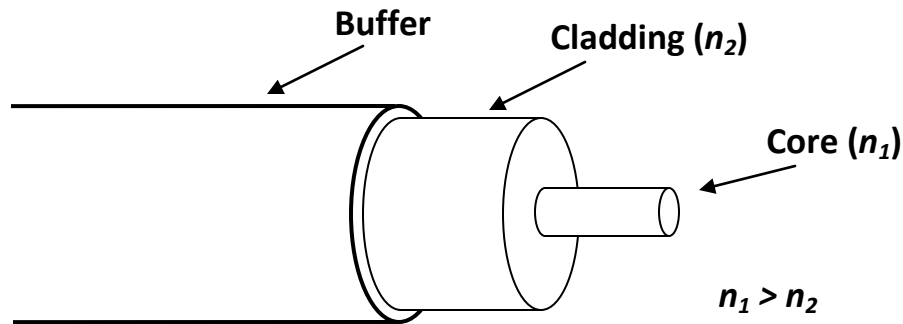
Figure 1.1: Basic optical fiber structure, n_1 and n_2 represent the refractive indices of the core and cladding, respectively.

The most common optical fiber is formed using silica (SiO_2) as the dielectric and germanium dioxide (GeO_2) as the index modifying dopant (i.e. to increase the refractive index of the core). However, other dopants, such as phosphorus oxide (P_2O_5), can be used to increase the refractive index of the core, while fluorine or boron trioxide (B_2O_3) can be used to lower the index of the cladding [3]. Optical fibers constructed using SiO_2 with the GeO_2 dopant have an extremely low loss, ~0.2 dB/km at 1550 nm, the majority of this loss is due to Rayleigh scattering of the light as it propagates through the fiber [4]. Though optical fibers can be constructed from materials other than silica, such as chalcogenide glass, halide glass or plastic, these fibers typically serve a specific purpose, e.g. chalcogenide glass fiber, which has a very high non-linear coefficient, is used in the development of Raman fiber lasers [5].

Under the weakly guiding approximation the modes supported by an optical fiber are known as linearly polarized modes (LP) [6]. Based on the number of transverse modes supported by an optical fiber, it can be classified into two main categories: single mode fiber (SMF) or multimode fiber (MMF). As implied by their names, SMF only supports the propagation of radiation in the fundamental (LP_{01}) transverse mode, while MMF can support many transverse modes beyond that of the fundamental mode. In addition, there are numerous types of optical fibers that can have polarization maintaining, high nonlinearity, or wide transmission bandwidth properties, which are related to the structure and material of the fiber [7].

The index of refraction of silica glass is independent of the polarization of the electromagnetic (EM) wave propagating through it, as amorphous silica is not naturally birefringent. Polarization is defined as the direction in which the electric field of an electromagnetic wave oscillates. A circularly symmetric SMF does not exhibit any natural birefringence, resulting in the propagation of a randomly polarized fundamental mode. However, any anisotropy in the core geometry due to bending or manufacturing defects at the core-cladding interface produces a birefringence in a SMF resulting in random fluctuations between the two orthogonal polarization modes, LP_{01}^{x} and LP_{01}^{y}. Polarization maintaining fibers (PMF) are an important fiber type used to address these random polarization fluctuations that occur in circular core optical fiber. PMFs are designed to maintain the polarization state of the propagating wave over a long distance by introducing a linear birefringence into the fiber [8]. The induced birefringence forces the electromagnetic wave to propagate as the two distinct polarization modes, LP_{01}^{x} and LP_{01}^{y}, which beat as they propagate along the fiber. The induced birefringence is achieved by creating an anisotropy in

the fiber core by including stress elements along the length of the core, or by modifying the core to be elliptic in shape [9].

Another important class of fiber is the rare-earth doped fibers, which are used as gain media in fiber lasers and amplifiers. The cores of these fibers are doped with rare-earth ions (e.g. erbium). Different laser wavelengths can be produced depending on which rare-earth element is used for doping the optical fiber. Some common rare-earth ions used as a dopant in a silica fiber and their respective emission wavelengths are erbium (Er^{3+}) at 1500 nm - 1600 nm, ytterbium (Yb^{3+}) at 1030 nm – 1100 nm, neodymium (Nd^{3+}) at 1064 nm – 1088 nm, thulium (Tm^{3+}) at 1750 nm – 2100 nm, and holmium (Ho^{3+}) at 2050 nm – 2170 nm [10-12].

Important in the scope of this dissertation is hollow-core photonic crystal fiber (HC-PCF) which is a specialty fiber. HC-PCF has a large hollow core surrounded by smaller air holes in a honey comb like structure that runs along the length of the hollow-core fiber and forms the cladding (**Figure 1.2**). In a HC-PCF light propagates through the core by the photonic band gap effect, this differs from conventional optical fiber which guides light via total internal reflection [13]. The periodic structure of high and low dielectric constants formed by the honey comb structured cladding imitates a 2-dimensional photonic crystal. A line defect in this structure forms the core of the fiber. This structure results in a range of forbidden energies corresponding to a narrow range of wavelengths, *i.e.* a photonic band gap. Similar to an electronic band gap where electron states corresponding to a range of energies cannot exist, a photonic band gap represents a range of wavelengths that cannot exist in the photonic crystal structure. This leads to a narrow band of wavelengths which can not propagate through the cladding and are confined to the core [14].

Hollow core photonic crystal fibers are appealing for their high damage threshold, low nonlinear effects, and low propagation loss since the vast majority of radiation is confined to the air filled hollow-core region. The unique properties of HC-PCF allow the fiber to be filled with different gases, leading to a variety of applications such as stimulated Raman scattering [15;16], producing mid- infrared output [17], or gas detection [18].
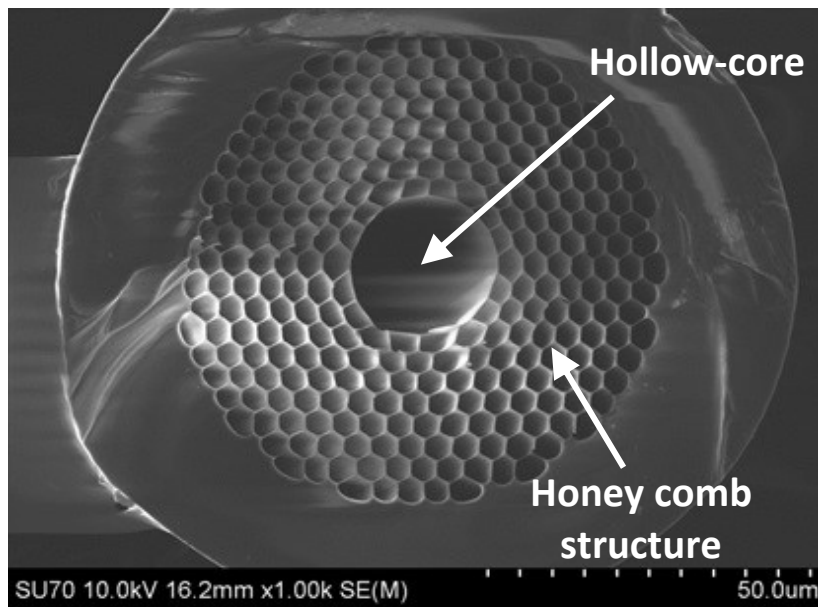
Figure 1.2: Scanning electron microscope image of a hollow-core photonic crystal fiber, showing the hollow-core surrounded by the honey comb structure of the cladding.

1.2 FIBER LASERS

A fiber laser uses a rare-earth doped fiber as the gain medium and a semiconductor diode-laser is typically used as the pump source. In general, fiber lasers can be grouped into two main categories based on the configuration of the resonant cavity: ring resonators (**Figure 1.3**), and linear resonators (**Figure 1.4**) [19;20]. A fiber ring resonator is formed by splicing optical components together to form a ring. The radiation in a ring resonator propagates around the cavity, passing through the gain medium multiple times. A ring resonator

eliminates the need for any reflectors and prevents any spatial hole-burning as seen in a linear cavity due to standing wave patterns formed by the interference of counter propagating waves.

Linear resonators, also known as Fabry-Perot resonators, are generally formed by using two end mirrors, which reflect the radiation back and forth through the gain medium forming a standing wave pattern by interference. In a fiber laser system, a fiber Bragg grating (FBG) or fiber loop mirrors are most commonly used as the reflectors.
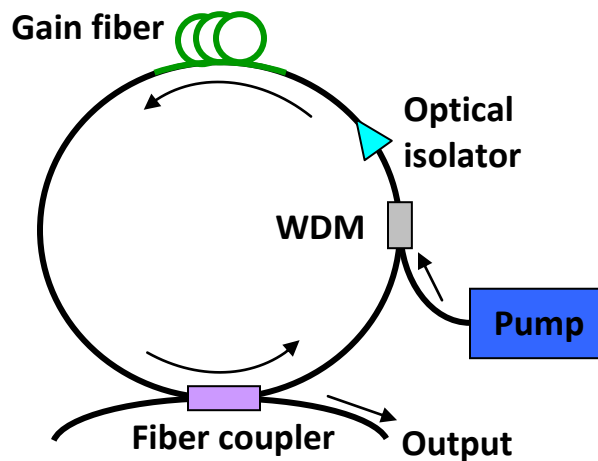
Figure 1.3: Ring cavity configuration. Pump radiation is coupled into the cavity through the wavelength division multiplexer (WDM) coupler, coupled out through a fused fiber coupler, and an optical isolator maintains unidirectional propagation of the light.
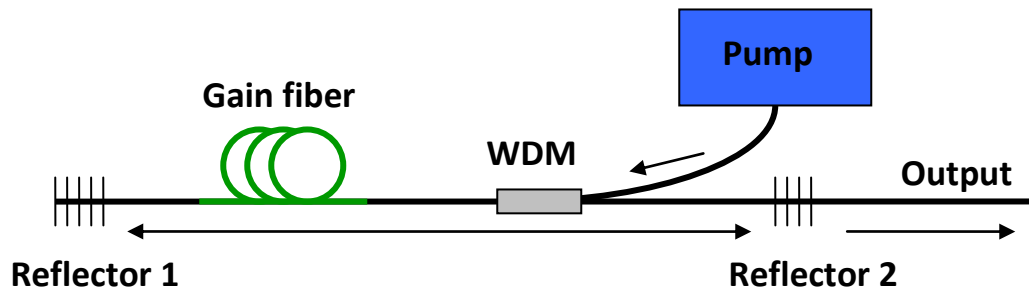
Figure 1.4: Linear cavity configuration, Reflector 1 and Reflector 2 forms the cavity.

Depending on the application, a fiber laser can be designed to operate in either the continuous-wave (CW) or PULSED regime. Continuous wave operation refers to a continuous laser output, while a pulsed laser will produce an output in pulses typically in the nanosecond range, though techniques have been demonstrated that can produce ultrashort pulses in the picosecond and femtosecond regimes [21].

Based on the number of transverse modes supported, fiber lasers can be further categorized as single-mode or multimode. The number of transverse modes supported by the laser is determined by the characteristics of the fiber used for the design of the cavity. Single-mode lasers are used when diffraction-limited beam quality is desired. Further, a single-mode fiber laser can operate in the single-longitudinal mode or multi-longitudinal mode regime, which is determined by the cavity length. Both single-longitudinal mode and multi-longitudinal mode fiber lasers are attractive for applications in sensing, telecommunications, and in material processing [10]. Lasers with multiple transverse modes are commonly implemented for applications where a higher output power is desired [22].

Some of the greatest benefits provided by fiber laser systems are their compact size, low power consumption, and no need for any external cooling as the large ratio of the fiber surface to core volume allows for excellent heat dissipation. Furthermore, fiber components are spliced together eliminating the need for alignment of optical components.

1.3   OPTICAL FIBER COMPONENTS

A fiber laser cavity can contain several passive optical components, such as optical fiber isolators (OI), wavelength division multiplexers (WDM), polarization controllers (PC), fiber

couplers (FC), optical circulators (OC), saturable absorbers (SA), or fiber Bragg gratings (FBG).

An all fiber polarization controller (PC) is used to alter the polarization state of the light propagating inside the laser cavity. By adjusting the polarization of the propagating radiation, the stability of the fiber laser output can be improved. An all fiber PC is formed by looping optical fiber around three circular plates (e.g., aluminum plates with a groove around the edge), in such a way that a quarter-wave (λ/4) plate, half-wave (λ/2) plate, and a second quarter-wave (λ/4) plate are formed, as shown in **Figure 1.5**. The fiber is looped so that the half-wave plate will have twice the number of loops as a quarter-wave plate [23]. The bending of fiber in the PC creates a bending-induced birefringence. This birefringence occurs over the length of the coiled fiber resulting in a significant effect that alters the polarization of the propagating electromagnetic waves. The smaller the bending radius the larger the induced birefringence, however, a smaller radius will also increase the attenuation of the propagating radiation, which is undesirable. The induced birefringence due to bending is given by [4]

$$\Delta n_{eff} = n_{ex} - n_{ey} = -C \left(\frac{b}{R} \right)^2 \tag{1.1}$$

where n_{ex} and n_{ey} are the effective refractive indices parallel and perpendicular to the bend, respectively, b is the radius of the fiber, R is the radius of the loop, and C is a constant determined from the elasto-optic properties of fiber material.
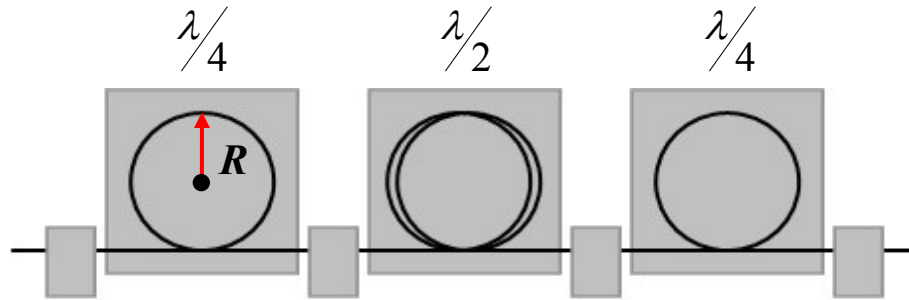
Figure 1.5: Simple configuration of a fiber polarization controller.

An optical isolator (OI) is a non-reciprocal device whose function is to allow radiation to propagate in one direction and prevent it from traveling in the other. OI's can be either polarization dependent or independent, however polarization independent OI are more commonly used in a fiber laser or amplifier system. A polarization independent OI is composed of a Faraday rotator sandwiched between two birefringent wedges (polarizers), as shown in **Figure 1.6**. Incident radiation passes through the wedge and is spatially split into orthogonal polarization components due to the fast and slow axes of the polarizer. The radiation then passes through the Faraday rotator and the polarized radiation is rotated such that the light polarized along the fast axis in the first wedge will be aligned with the slow axis in the second wedge and vice versa for the other polarization component. Thus, when the radiation propagates through the second wedge it is recombined and coupled back into the system. When light travels in the reverse direction the same process occurs, however due to the nature of a Faraday rotator, when the radiation enters the second wedge the light polarized along the fast axis is again aligned with the fast axes and the slow is aligned with the slow axis. This results in a further spatial separation between polarized components, which are not recombined nor coupled back into the system. OIs are often used to prevent

feedback to the laser diode, which can result in an unstable output or damage to the laser source, and to maintain unidirectional propagation in ring cavity laser configurations.

Birefringent wedge   **Faraday rotator**   **Birefringent wedge**
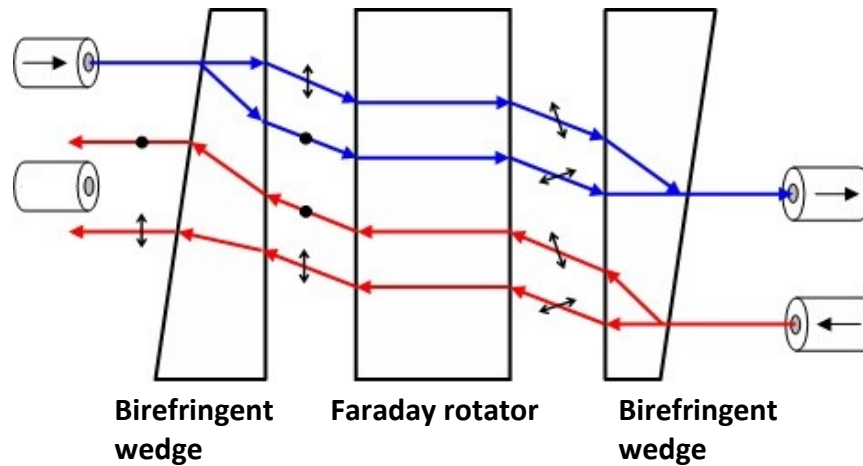
Figure 1.6: Radiation propagation in an optical isolator. Forward travelling radiation (BLUE) is coupled back into the fiber core while radiation propagating in the backward direction, in the same optical fiber, (RED) will not be coupled back into the fiber. As the light travels through the OI the changes in polarization are indicated.

A circulator is essentially the same as an optical isolator; they are non-reciprocal devices which allow light to propagate in a specific direction. Circulators are commonly made with three-ports (**Figure 1.7**). Radiation incident into port 1 will be transmitted out of port 2, following the same principle as with the optical isolator (OI), however when radiation enters port 2 it becomes spatially separated as shown with the backwards propagating radiation in **Figure 1.6**. The spatially separated polarization components are recombined using optical components (e.g., reflection prism and beam splitter) and transmitted out of port 3. Circulators can be used to form a broad band reflector by splicing the port 1 and port 3 fibers together.
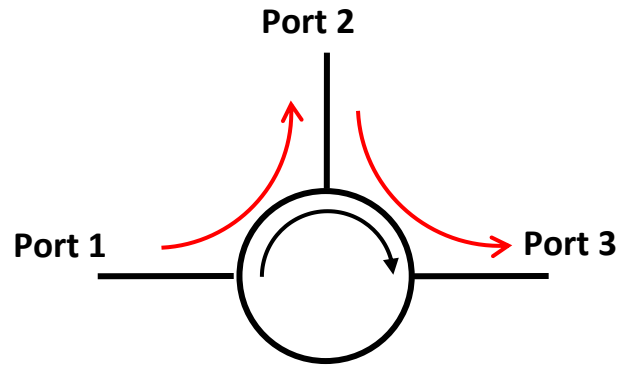
Figure 1.7: Radiation propagating in an optical circulator; red arrows indicate the direction of the propagating radiation.

One of the most important passive optical components is the fiber coupler (FC). A FC has applications as a power splitter, power combiner and wavelength division multiplexer (WDM). A FC can be thought of as the optical fiber equivalent of a beam splitter. A coupler can be either a core or surface interaction type. A core interaction type coupler transfers power directly through the end of one fiber into another. By adjusting the lateral offset of the two fibers the desired coupling power ratio can be achieved. The more commonly used surface interaction type couplers can be formed using either of two methods: either by fusing and pulling the fibers together along the axis of propagation, or by polishing the fiber sides along the length and keeping them in contact with an index matching fluid. A fused fiber coupler (FFC) has the benefit of being highly stable and robust, while polished fiber couplers have the advantage of being tunable by adjusting the lateral position between the two polished fibers [24]. The fiber coupler functions by transferring energy from one fiber core to the other. The mode field distribution of the propagating light in a fiber core extends past the core-cladding interface. By placing two fiber cores in parallel and in close proximity, the radiation can couple from one fiber core to the other resulting in optical power being transferred between fibers. The amount of power exchanged between the fibers is

determined by the coupling coefficient of the fiber coupler which is dependent on the radiation wavelength, fiber characteristics, the cores separation, and coupling length [4].

Similar to a fused fiber coupler, a wavelength division multiplexer (WDM) coupler is designed using coupled mode theory. A WDM is designed to combine a number of wavelengths from multiple optical fibers into a single fiber. A WDM is often implemented when developing a fiber laser or amplifier as a 2 x 1 (2-to-1) structure where two fibers carrying two different wavelengths are coupled into a single fiber. Depending on the wavelengths being multiplexed different input fibers can be used for the WDM. The wavelength selectivity and power transfer of a WDM is dependent on variations between the coupling fibers and the coupling length of the WDM [4]. WDMs are used in telecommunications for mixing multiple wavelength signal channels into a single optical fiber and vice versa (demultiplexing). This allows for an increase in the effective bandwidth of the system and reduces the cost of data transmission by greatly decreasing the number of carrier fibers [25]. The fiber laser system presented in this dissertation uses a WDM to couple 980 nm radiation from a pump laser into the single mode fiber of the resonant cavity.

Fiber Bragg gratings (FBG) are all-fiber reflectors formed by writing periodic or aperiodic variations in the refractive index of the core of an optical fiber. A typical FBG has a uniform variation in the refractive index with a constant depth of modulation (**Figure 1.8**). There are various types of FBGs which include: long period gratings whose periodicity spans a larger fiber length, tilted gratings which are written at an angle to the optical axis, and chirped

gratings, which are aperiodic gratings that have a linearly decreasing variation in grating period.
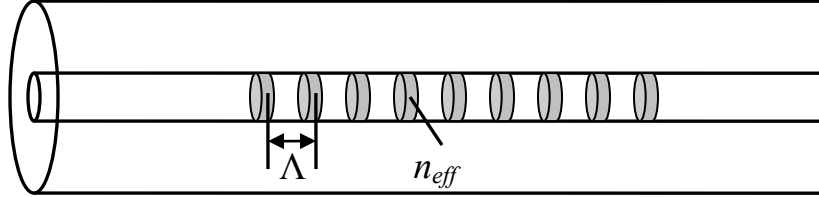
Figure 1.8: General fiber Bragg grating structure where Λ represents the separation between index variations and n_{eff} is their effective refractive index.

The main mechanism behind making a FBG is referred to as photosensitivity and was first reported in 1978 by Ken O. Hill et al. [26]. Photosensitivity is the nonreversible change a material experiences when it interacts with certain wavelengths of radiation. Pure silica has a very weak photosensitivity which can be greatly increased by doping the core of the silica fiber with germanium oxide (GeO_2) [27]. A FBG is written into the core of a Ge-doped silica fiber through the cladding using a UV light source and a grating mask, the change in the cladding refractive index is minimal, as it is made of pure silica. The FBG will have a maximum reflectivity for the wavelength which satisfies the Bragg condition, given by,

$$\lambda_{FBG} = 2\Lambda n_{eff} \tag{1.2}$$

where Λ is the periodicity of the index variation and n_{eff} is the effective refractive index of the grating.

Saturable absorbers (SA) are optical materials that exhibit an intensity dependent loss, i.e. as light intensity increases, loss decreases. Radiation is absorbed by the SA ions in the ground state and become excited to a higher energy state. Once they are in an excited state

they will no longer absorb incident light. Hence, as more ions become excited, less absorption occurs. Unpumped rare-earth doped fibers are commonly used as a SA. They are used to increase the stability of a fiber laser output, and as a passive mode locking element to produce short high intensity pulses in a Q-switched or mode-locked lasers [28;29].

Reference [30] describes the application of a SA in the laser cavity to stabilize the lasing wavelength. In the laser cavity, the counter propagating waves within a Fabry-Perot cavity segment produce a standing wave pattern which leads to periodic variations in the light intensity within the SA. This results in a modulation of the refractive index in the SA. This variation in the refractive index adapts to changes in the lasing wavelength and produces a transient Bragg reflection grating. In general, a laser that contains multiple longitudinal modes is susceptible to instabilities due to mode-hopping, which results from environmental fluctuations such as temperature or vibrations. The transient grating acts as a tracking filter which reduces the laser linewidth and stabilizes the laser by helping to eliminate mode-hopping [28;31]. The expression for the reflection bandwidth of the transient grating is given by [32],

$$\delta v = \frac{c}{2\pi n} \sqrt{\left(\frac{\pi}{L}\right)^2 + \frac{|\kappa|^2}{1 + (\widetilde{g}L/\pi)^2}} \approx \frac{c}{2nL} \qquad (1.3)$$

where L is the length of the SA, c is the speed of light, n is the refractive index, $\widetilde{g}$ is the saturated gain factor, and κ is the coupling coefficient. The reflection bandwidth of the transient grating is inversely proportional to the length of the SA and by increasing the length of the SA a very narrow-band transient grating can be obtained. However, an increased SA length results in an increased threshold pump power for the laser.

1.4 OPTICAL SENSORS

Optical fiber systems have been able to address many of the drawbacks associated with other sensing technologies, such as high costs, design complexity, and space requirements; making them appealing for a variety of applications. The majority of fiber sensors have found applications in strain, temperature, and pressure measurements with many being based on fiber Bragg gratings [33]. A FBG sensor responds to any thermally or mechanically induced expansion or contraction, with a change in the reflected wavelength. The resulting change in the reflected wavelength gives information about changes in the sensors environment. As photonic technology advances, fiber sensors have found applications in more complex problems, such as biosensors in medicine, chemical sensors in industrial settings, and trace gas detection in environmental monitoring [34].

The focus of this dissertation is on the detection of gaseous analytes using an optical fiber laser system. Gas sensors based on optical fiber technology can be designed for remote sensing applications that require a high sensitivity and real time measurements of individual gas species. Absorption spectroscopy is a nondestructive method for monitoring gas concentrations. The biggest challenge in developing a gas sensor is achieving high sensitivity without sacrificing the fast response or simplicity in the design inherent with optical fiber systems. As the concentration of gas decreases, a system with a higher sensitivity would be required. Though spectroscopy techniques exist with extremely high sensitivities (e.g., fluorescence spectroscopy) the scope of this dissertation will remain on absorption spectroscopy and more specifically on near infrared (NIR) absorption spectroscopy.

1.5 ABSOPRTION SPECTROSCOPY

Quantum mechanics dictates that molecular energy is quantized and when a molecule gains or loses energy it can only make a transition between discrete energy levels. Absorption spectroscopy (AS) techniques measure the electromagnetic radiation absorbed by molecules when an allowed transition is occurs. Depending on the wavelength of the absorbed radiation a molecule can make a transition to a higher electronic state, vibrational level, rotational level or any combination of the three.

Rotational transitions are the result of a change in the rotational state of a molecule in the gaseous phase. The changes in rotational levels in the same vibrational level and electronic state will typically occur with the absorption or emission of microwaves. Since the energy required for a transition between different rotational levels is very small, at room temperature rotational energy levels are populated as described by the Boltzmann distribution [35].

Vibrational transitions will occur if an incident photon has an energy which corresponds to the difference between vibrational energy levels and results in a change in the vibrational motion of the molecular bonds. The changes between vibrational levels in the same electronic state are typically due to the absorption or emission of infrared radiation. The separation between vibrational energy levels is much greater than rotational levels and molecules tend to be in their vibrational ground state at room temperatures [36].

Electronic transitions are related to a change in the molecular orbital energy of a molecule. These transitions are typically due to the absorption or emission of visible and ultraviolet radiation. By absorbing a photon with an energy which corresponds to the difference between two electronic states, a molecule will enter an excited state, i.e. a higher electronic state. An excited state is related to the promotion of an electron from a ground state

molecular orbital (i.e., highest occupied molecular orbital) to a higher energy molecular orbital. Likewise, an electronic transition can occur when a molecule decays from an excited state to a lower electronic state [37].

Figure 1.9 shows a simple energy level diagram which depicts the rotational, vibrational, and electronic energy levels. As radiation is transmitted through absorbing molecules, absorption will occur at discrete frequencies which correspond to an energy difference between the allowed molecular transitions. The frequency (v) of the absorbed radiation is related to the difference in energy levels by,

$$h v = |E_1 - E_2| \tag{1.4}$$

where h is the Planck constant, and E_1 and E_2 are the initial and final energy levels, respectively. These initial and final energy levels can correspond to any rotational, vibrational, or electronic level as long as the transition between them is not forbidden by the selection rules which are related to electric and magnetic dipole transitions [38]. The absorption at these frequencies is referred to as absorption lines and varies in strength depending on which transition is occurring. The intensity of each absorption line is determined by the relative population of different energy levels of the molecules, as defined by the Boltzmann distribution, and the transition probability between the initial and final energy level. The collection of absorption lines makes up the absorption spectrum of a molecule. Hence, individual absorption lines may overlap for different molecules, but the whole absorption spectrum formed for a specific molecule is unique.
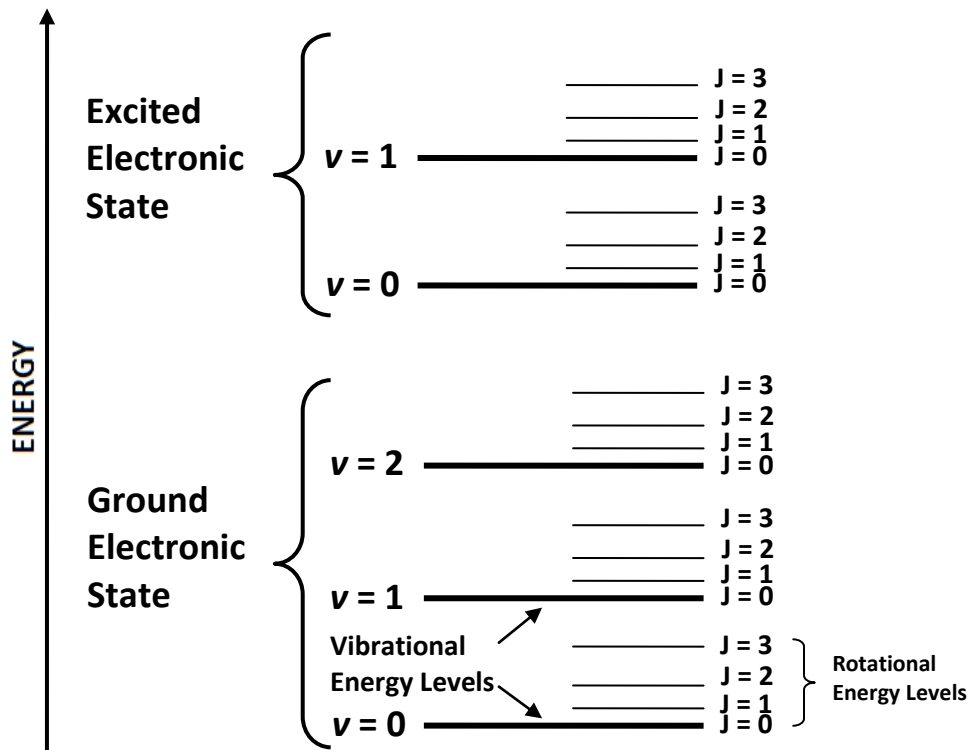
Figure 1.9: Energy level diagram depicting the various molecular energy bands, where *v* represents vibrational levels and *J* represents rotational levels.

Since AS measurements are quantitative, concentrations of an analyte can be directly determined. Further, the AS measurements allow for the identification of the absorbing molecules from their recovered spectrums which has lead to an abundance of applications spanning medicine, astronomy, and environmental monitoring. This section will focus on infrared absorption spectroscopy, or more precisely, near-infrared (NIR) absorption spectroscopy. The NIR region includes wavelengths from ~0.7 μm to 3 μm which are related to vibrational and ro-vibrational transitions. Vibrational transitions occur when a transition to another vibrational level is induced, and a ro-vibrational transition is defined as a change in both the vibrational energy level and the rotational energy level [39].

The normal modes of vibration for a molecule are determined by the molecular structure and the number of atoms it is composed of. Each atom has 3 degrees of freedom related to its position in Cartesian coordinates (x, y, and z). The motion of these atoms will describe the translational, rotational, and vibrational motion of the molecule. Hence, a molecule consisting of N atoms will have 3N degrees of freedom. However, for three translational and three rotational degrees of freedom the internuclear distances between the atoms remain constant in the molecule which results in a total of $3N-6$ fundamental (or normal) vibrational modes for nonlinear polyatomic molecules. For linear molecules there are only two redundant rotational motions since rotations along the molecular axis are not distinguishable, this results in $3N-5$ vibrational modes. In general, a normal vibrational mode will be infrared active if the resulting vibrational motion of the molecule leads to a change in its dipole moment. Vibrational modes which do not change the dipole moment of the molecule are said to be infrared inactive. These changes in the dipole moment can be either parallel or perpendicular to the main axis of symmetry. Once a molecule has been excited to a higher vibrational energy state, it will quickly dissipate the vibrational and rotational energy either by non-radiative process (e.g., through collisions), or by emission of a photon in a random direction. This process takes less then 10^{-6} seconds [35].

Fundamental transitions are those from the ground vibrational state to the first excited vibrational state ($v=0 \rightarrow v=1$) and overtone transitions are those from the ground state to the second or higher excited vibrational level (i.e. $v=0 \rightarrow v=2,3,4...$). Overtone transitions have a much lower probability of occurring than fundamental transitions. Combinations of vibrational transitions can also exist; these bands are referred to as combination bands. These vibrational transition bands can be a combination between any of the fundamental and

overtone transitions. For example, a hydrogen sulfide (H_2S) molecule has three fundamental vibration frequencies ($v_1 = 2614\,cm^{-1}$, $v_2 = 1183\,cm^{-1}$, $v_3 = 2628\,cm^{-1}$) with linear combinations of these and overtones in the NIR (i.e. $2v_1 + v_2 = 6288\,cm^{-1} \sim 1.59\mu m$, $v_1 + v_2 + v_3 = 6289\,cm^{-1} \sim 1.59\mu m$, and $v_2 + 2v_3 = 6386\,cm^{-1} \sim 1.56\mu m$) [40]. Combination and overtone bands are usually at a lower frequency than expected as a result of anharmonic oscillations.

An absorption band is composed of the vibrational and ro-vibrational transitions which are related to that particular vibrational transition. The absorption band can be divided into three different sections, referred to as the P, Q, and R branches. These are related to the specific rotational transitions within the particular vibrational transition **(Figure 1.10)**. The Q-branch represents a pure vibrational transition where no change in rotational energy take place, e.g., $v \rightarrow v+1$ and $\Delta J = 0$. Vibrational modes which results in dipole moment changes parallel to the main axis of symmetry will not display a Q-branch. The P and R branches arise when a vibrational transition $v \rightarrow v+1$ occurs with a change in the rotational quantum number of $\Delta J = \pm 1$. The P-branch coincides with transitions $\Delta J = -1$ and the R-branch coincides with $\Delta J = +1$ transitions.
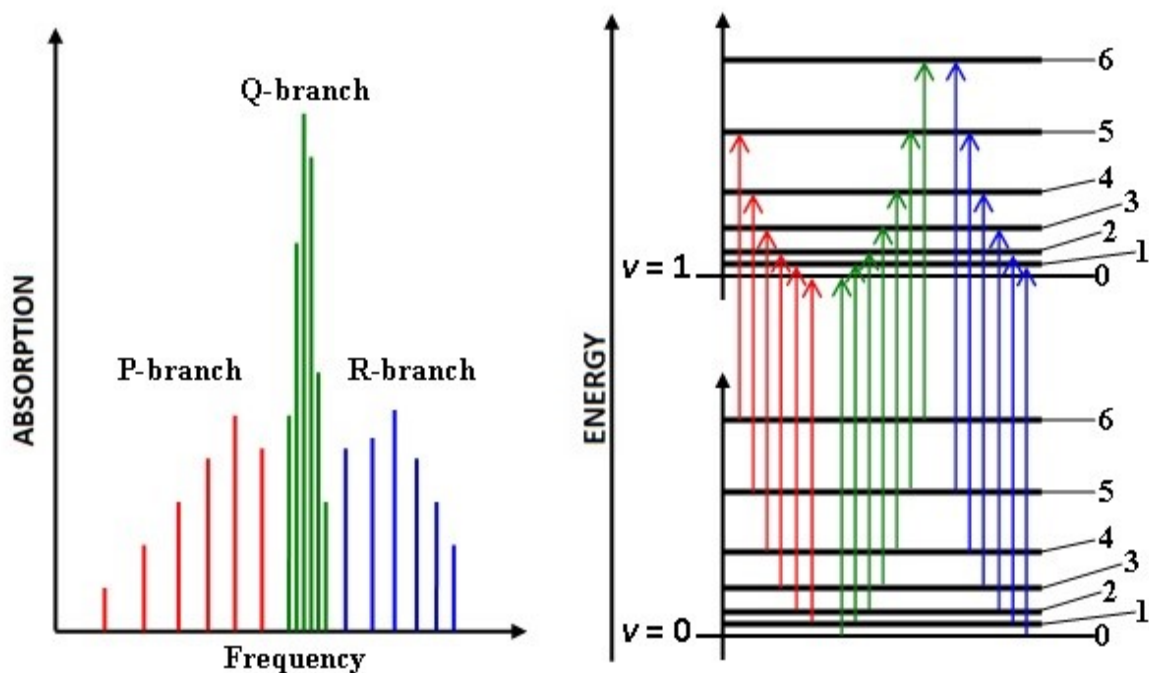
Figure 1.10: Left image is the P-branch (RED), Q-branch (GREEN), and R-branch (BLUE) in an absorption spectrum. Right image is the corresponding energy level transitions for each branch.

NIR spectroscopy benefits from low cost laser sources and detectors that can be operated at room temperature. Unfortunately, the weak absorption lines that reside within the NIR region are typically 2 to 3 orders of magnitude below those of the fundamental transitions that are in the Mid-IR region (~ 3 - 8 µm; **Figure 1.11**). In general, Mid-IR lasers are more expensive than those in the NIR with equivalent or greater output power. Furthermore, a Mid-IR laser detector needs cooling below -40^0 C, compared to a NIR laser detector, which can be operated at room temperature.

21
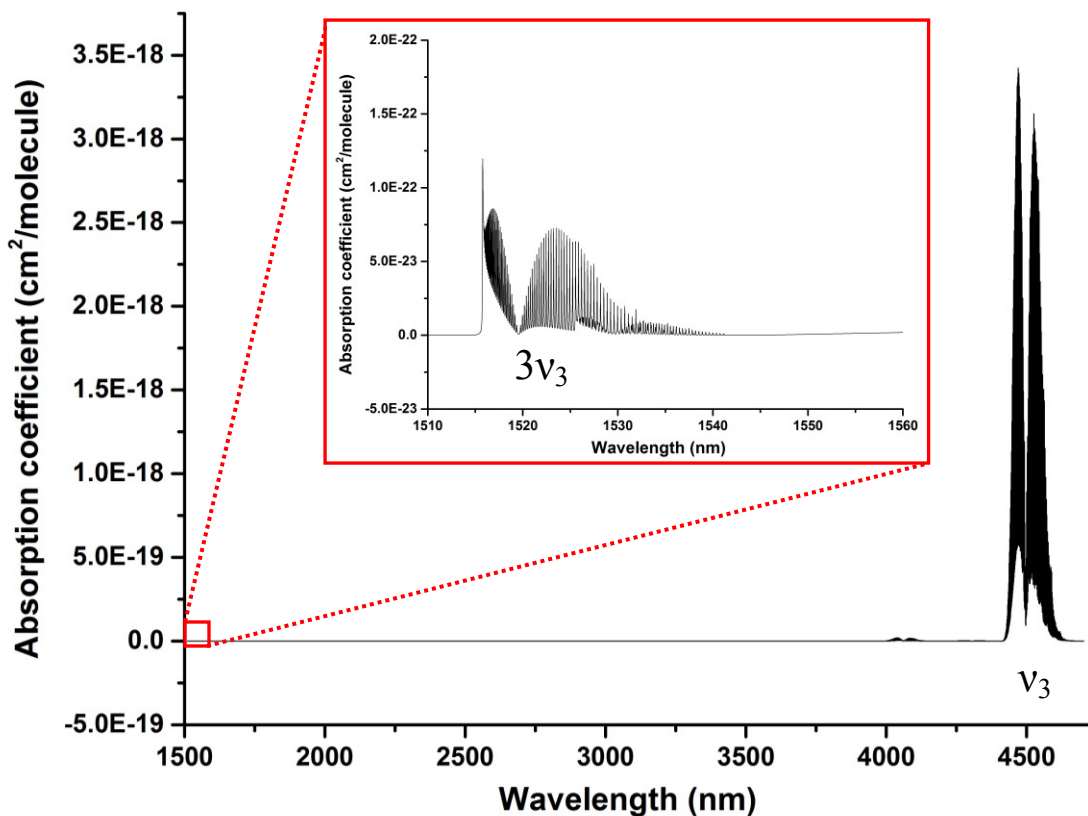
Figure 1.11: N_2O absorption spectrum from 1500 to 4750 nm (1.5 to 4.75 μm) obtained from HITRAN [41]. As can be seen, the $3\nu_3$ overtone absorption band at 1522 nm in the NIR is extremely weak compared to the fundamental (ν_3) vibrational mode at 4496 nm.

Some of the important characteristics of NIR spectroscopy systems which affect the applications of the devices are their selectivity, design complexity, and sensitivity. Selectivity is the ability to measure a specific analyte in the presence of other absorbing species. In absorption spectroscopy, selectivity is determined by the laser linewidth, since a laser with a broad linewidth could potentially overlap with multiple absorption lines. The selectivity is also affected by the spectral width of the absorption lines, which become broader with increasing pressure and overlap with neighboring absorption lines [42]. Selectivity is an important aspect for applications that involve sample detection in the presence of different molecules, e.g., detection of a particular gas in the atmosphere.

System complexity refers to how simple the detection technique is in regard to maintenance, operation, and overall structure. For example, a system that operates at room temperature will typically be considered less complex compared to a system which operates at cryogenic temperatures.

Sensitivity is one of the most important parameters for any AS system, and refers to the minimum detectable change in concentration that can be measured by the system. A noisy background can severely limit the sensitivity of a technique. Noises which limit an AS system sensitivity are pink noise, thermal noise, and shot noise [43].

Pink noise is inherent in laser systems, and is commonly referred to as *1/f* noise. It is more prominent at low frequencies and decreases with increasing frequency. This type of noise can be reduced through techniques that modulate the laser source at a high frequency. Wavelength modulation (WM) and frequency modulation (FM) are commonly used modulation techniques for reducing *1/f* noise [44].

Thermal noise (also known as Johnson noise or Nyquist noise) is electronic noise that is frequency independent and occurs within the load resistor of the photodiode circuit as a result of thermal fluctuations. These thermal fluctuations produce a random motion of the electrons in the resistor, which in turn results in random fluctuations in photo current. Thermal noise can be expressed by the mean square current which is related to the detector temperature (T), the bandwidth ($\Delta \nu$), and load resistance (R_L),

$$\overline{i_N^2}(\nu) = \frac{4kT\Delta\nu}{R_L} \tag{1.5}$$

where k is the Boltzmann constant. Thermal noise can be decreased by reducing the absolute temperature of the detector and/or by increasing the load resistor [45]. However, since the

frequency bandwidth of a photodetector, which is given by **Equation 1.6**, is related to the load resistor, a balance must be met.

$$\nu_{BW} = \frac{1}{2\pi R_L C_j} \tag{1.6}$$

where R_L is the load resistor and C_j is the junction capacitance of the photodiode.

Shot noise is a quantum noise effect which is used to describe the random intensity fluctuations due to the discrete nature of the incident photons, and thus generation of electron-hole pairs [4]. Shot noise can be expressed as a mean-square current amplitude,

$$\overline{i_N^2}(\nu) \equiv 2e\bar{I}\Delta\nu \tag{1.7}$$

where $\Delta\nu$ is the bandwidth, e is the charge of an electron, and $\bar{I}$ is the average current generated by the detector, which includes the dark current and the photo current due to the incident light on the detector. The averaged current is related to the number of electrons generated as predicted by Poisson statistics [45].

A number of techniques have been demonstrated to improve the minimum detection limit by reducing noise, enhancing the signal, or a combination of both. The most common AS methods are direct absorption spectroscopy (DAS), wavelength modulation spectroscopy (WMS), frequency modulation spectroscopy (FMS), cavity ring-down spectroscopy (CRDS), photoacoustic absorption spectroscopy (PAS), and intracavity absorption spectroscopy (ICAS).

1.5.1   BEER-LAMBERT LAW

If the light passing through a sample has an energy which corresponds to a molecular transition, the transmitted light will experience a reduction in intensity and follow an

exponential law. This phenomenon governs absorption spectroscopy techniques and the transmitted intensity is determined by the Beer-Lambert Law, defined as [46],

$$I(\lambda) = I_o(\lambda)e^{-A} = I_o(\lambda)e^{-\alpha(\lambda)CL} \tag{1.8}$$

where $I_o(\lambda)$ is the incident intensity, $I(\lambda)$ is the transmitted intensity, and A is the absorbance. The absorbance of a medium is wavelength dependent and is related to the absorption coefficient ($\alpha(\lambda)$), sample concentration (C), and interaction length (L).

1.5.2 DIRECT ABSORPTION SPECTROSCOPY (DAS)

DAS is a simple laser absorption spectroscopy technique used to determine an analyte concentration by allowing incident radiation to make a single pass through the gas cell [47]. The transmitted intensity is measured and the absorbance can be directly calculated using the Beer-Lambert law (**Figure 1.12**). The sensitivity of DAS systems is very low compared to other AS methods.
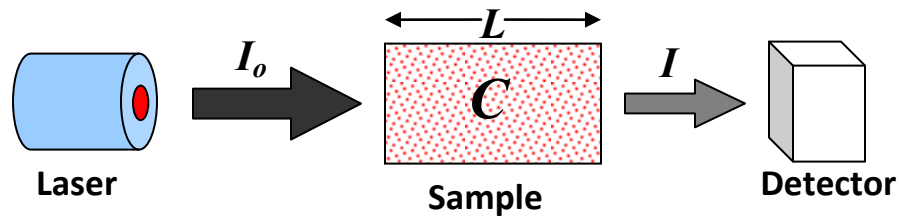
Figure 1.12: Example of the DAS technique. Laser intensity propagates through a sample and is attenuated due to wavelength-dependent absorption of the molecules. The transmitted intensity is then detected.

A longer path length can increase sensitivity. However, the gas cell can only be increased to a reasonable length. In the DAS technique, fluctuations of the laser intensity and noise in the circuit reduce the signal-to-noise ratio limiting its performance for the detection of analytes at low concentration. The sensitivity of DAS is typically on the order of 10^{-3} [48], which has led to the continued desire to improve the spectral resolution and sensitivity through the development of new methods. Newer techniques include modulation of the laser diode to reduce noise, and increasing the effective path (or interaction) length without physically increasing the cell size. It is also clear from the Beer-Lambert law (**Equation 1.8**) that the minimum detectable concentration could also be improved by selecting the transition with the largest absorption coefficient, which corresponds to the fundamental vibrational bands. Since the frequency of fundamental vibrational modes reside in the Mid-IR spectral region, this would increase the cost and complexity of the system.

1.5.3 WAVLENGTH MODULATION SPECTROSCOPY (WMS) AND FREQUENCY MODULATION SPECTROSCOPY (FMS)

WMS and FMS are spectroscopy techniques that improve the detection limit of DAS measurements by reducing the noise in the recovered signal. These modulation techniques increase the signal-to-noise ratio by modulating the laser wavelength at a high frequency which results in the measured signal being shifted to that higher frequency and away from the common low frequency system noise, i.e. *1/f* noise. Modulation spectroscopy (MS) requires the use of a laser that has a wavelength dependent relationship with current/temperature, such as a distributed feedback (DFB) laser diode [49]. As the input current to the laser diode is increased, temperature will also increase which leads to the

internal grating of the DFB expanding and, consequentially, changing the DFB laser output to a longer wavelength. By exploiting this relationship, the output wavelength will be modulated at the same frequency as the modulating current frequency. The output frequency is given by,

$$\nu(t) = \nu_L + d\nu \cos(\omega_m t) \tag{1.9}$$

where ν_L is the center frequency, $d\nu$ is the modulation amplitude, and ω_m is the modulation frequency. Due to the interaction between the modulated laser output and the nonlinear absorption lineshape, the transmitted signal will contain harmonic components at multiples of the modulation frequency. These harmonic components can be identified by using a lock-in amplifier, and the absorption signal can be recovered [50]. WMS and FMS measurements can either be taken at a fixed position, which is centered on the absorption line, or by scanning across the absorbing lines. Scanning MS is performed by simultaneously ramping and modulating the laser current, as shown in **Figure 1.13**. It provides the advantages of measuring multiple absorption lines at a time, as well recovering the absorption lineshape which is related to the temperature and pressure of the sample [51]. The main difference between WMS and FMS is the frequency of the modulation. A MS system is usually considered to be WMS when the modulation frequency is less than linewidth of the absorption line, whereas for FMS the modulation frequency is equal to or greater than the linewidth of the absorption line. The sensitivity of MS systems can be on the order of 10^{-7} [52].
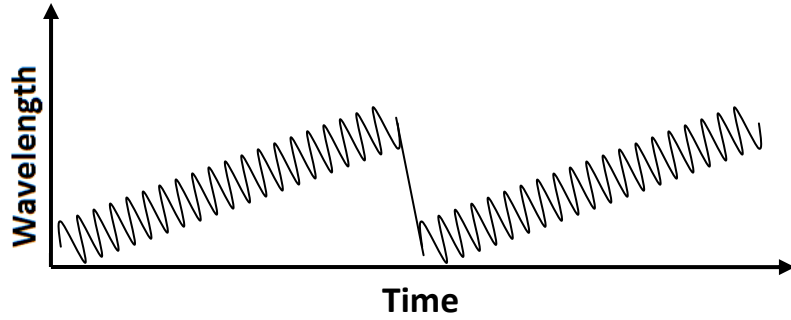
Figure 1.13: Diode-laser output wavelength versus time when the input current is modulated sinusoidally and ramped.

1.5.4 CAVITY RING-DOWN SPECTROSCOPY (CRDS)

CRDS determines sample concentrations based on the rate of intensity decay as opposed to the change in intensity. A CRDS system consists of an input laser and a high finesse ring-down cavity (RDC), which houses the absorbing sample in a gas cell. Depending on the mode of laser operation, one can have a PULSED-CRDS or continuous wave-CRDS (CW-CRDS). In a CRDS system with a PULSED laser, a laser pulse is injected into the RDC. For an empty ring-down cavity, the injected pulse will exponentially decay as a small fraction of its intensity is coupled out of the cavity with each round trip inside. When an absorbing sample is included in the RDC, the rate of decay of the pulse intensity will increase due to the presence of additional loss following the relation [53],

$$\frac{I}{I_o} = e^{-t\sigma/\tau}$$

(1.10)

I_o is the initial intensity, I is the transmitted intensity, t is the duration of the number of roundtrips being measured, σ is the net cavity loss, and τ is the roundtrip time. The time required for the intensity to reduce to 1/e of its initial value is referred to as the ring-down time, t_r, and given by,

28

$$t_r = \frac{\tau}{\sigma} \tag{1.11}$$

The net cavity loss (σ) includes the loss due to the absorption by the gas sample [53]. As the absorbing medium concentration decreases the ring-down time increases and approaches that of the empty RDC. Since the sensitivity of this technique is dependent on the lifetime of the propagating radiation, either a ring-down cavity with very low intrinsic loss or a ring down cavity with a gain medium to balance cavity loss is required [53]. In general, a CW laser is modulated externally to produce pulses with the desired width that are used as the source of the CW-CRDS [54]. This can be done by interrupting the CW input into the RDC with a chopper or by quickly sweeping the laser frequency across the cavity modes of the RDC. The decay of the light intensity in the RDC is then monitored using a high-speed detector and an oscilloscope. A hypothetical illustration of the output power versus time for a CW-CRDS system is shown in **Figure 1.14**. One of the major benefits of a CRDS system is that it is not affected by fluctuations in the lasers output intensity, since the radiation being monitored is no longer in resonance. However, the drawbacks of this technique are the requirement of high speed electronics and a very high finesse ring-down cavity. A CRDS system operated in the NIR has demonstrated a minimum detectable absorption coefficient on the order of 10^{-10} cm^{-1} [55].
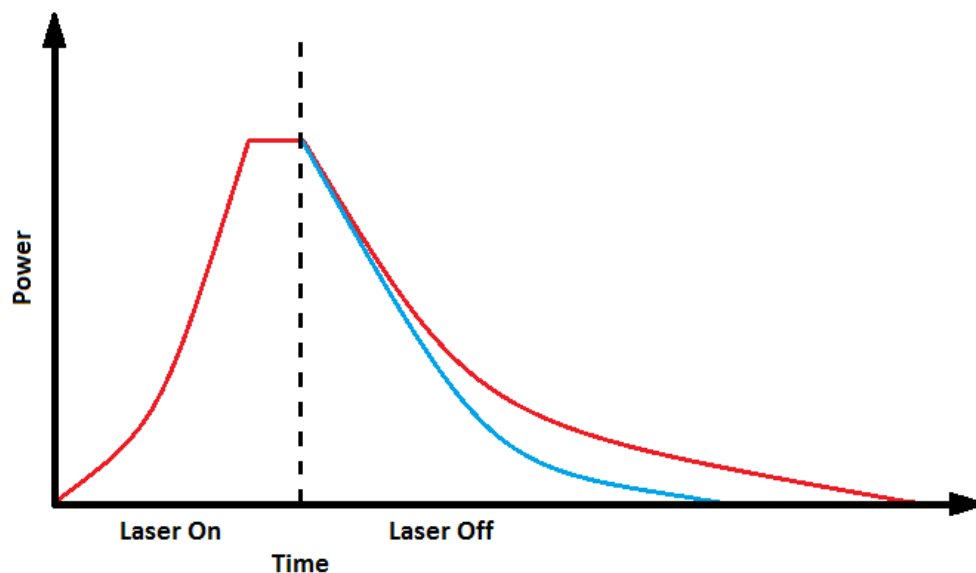
Figure 1.14: CW-CRDS system - the RED line represents the initial intensity build up and the cavity ring down time without a sample and the BLUE line represents the cavity ring-down time with a sample present.

1.5.5   PHOTOACOUSTIC SPECTROSCOPY (PAS)

Photoacoustic spectroscopy is a high sensitivity detection technique commonly used for trace gas detection. PAS determines the concentration of an analyte by detecting the pressure waves produced as a result of the photoacoustic effect. The photoacoustic effect occurs when radiation is incident on an absorbing medium. The molecules which absorb the light are induced into a higher thermal state. The resulting increase in temperature (local heating) leads to a change in pressure. Once the incident radiation is interrupted or blocked the thermal energy is quickly dissipated. The molecules will then return to their initial thermal state as will the density. The expansion and contraction due to the abrupt change in localized temperature produces a pressure wave. As a consequence of photoacoustic effect, if the incident light is modulated, an acoustic signal will be produced at the modulation frequency [56].

A simple PAS system is formed with an acoustic resonator, which is the gas cell, and a highly sensitive microphone. A modulated CW laser source with a wavelength corresponding to one of the samples absorption lines is transmitted through the gas cell. The laser output can be modulated using a number of techniques which results in periodic laser pulses, such as a chopper, an external modulator, intensity modulation, etc. [57]. A pulsed laser with the desired repetition rate can also be used. The acoustic signal gets amplified, when the modulation frequency of the laser is tuned to one of the acoustic modes of the cavity. The resulting acoustic waves produced by the sample will have the same periodicity as the laser. The photoacoustic signal detected by the microphone is given by,

$$S = P(\lambda) \cdot C \cdot \alpha(\lambda)$$
(1.12)

where $P(\lambda)$ is the optical power, C is the cell constant, and $\alpha(\lambda)$ is the absorption coefficient. The cell constant is related to the microphone response, cell shape, modulation frequency, and acoustic mode of the cavity [56]. Since the absorption coefficient is directly related to the sample concentration, there is a linear relationship between the acoustic signal and the sample concentration. One of the main benefits of PAS is that the microphone only detects pressure waves. Hence, the same setup can be used with the laser source which best suits the gas being detected. PAS systems can achieve very high sensitivities, specifically quartz-enhanced photoacoustic spectroscopy (QEPAS) has demonstrated the detection of analytes in concentrations of pptv (parts-per-trillion by volume) [58]. The PAS technique has demonstrated a minimum detectable absorption coefficient on the order of 10^{-10} cm^{-1} [59].

1.5.6 INTRA-CAVITY ABSORPTION SPECTROSCOPY (ICAS)

Intra-cavity absorption spectroscopy (ICAS), is an AS technique, which improves detection sensitivity by increasing the effective path length of interaction with the sample. ICAS is among the simplest spectroscopic methods to implement, which is done by incorporating a gas cell inside the laser resonator. As the radiation intensity begins to build up in the cavity, resonant modes will begin to oscillate and be amplified. However, the modes which coincide with absorbing features will experience a lower gain as a result of the additional absorption loss. The light makes multiple passes in the laser cavity, which leads to the absorption spectrum being imprinted onto the output spectrum of the laser. The multiple passes in the cavity result in an increase in the effective interaction length of the light with the sample. For ICAS systems it is sometimes convenient to express the sensitivity of the system in terms of the effective path length (L_{eff}) [48],

$$L_{eff} = \frac{A}{\alpha_{min}} \qquad (1.13)$$

where α_{min} is the minimum detectable absorption coefficient, and A is the absorbance,

$$A = \ln\frac{I_o}{I} \approx \frac{\Delta I}{I_o} \qquad (1.14)$$

where I_o is the incident intensity and I is the transmitted intensity. An optimized ICAS system reported using a dye laser in the visible spectrum by Baev et al., demonstrated an effective path length of 70,000 km for a gas cell with a physical length of 1.9 m [48]. Furthermore, one of the benefits of ICAS is the capability of detecting many analytes whose absorption features fall within the laser gain medium [60]. The ICAS technique has demonstrated a minimum detectable absorption coefficient on the order of 10^{-10} cm^{-1} [61].

1.5.7 NOISE-IMMUNE CAVITY-ENHANCED OPTICAL HETERODYNE MOLECULAR SPECTROSCOPY (NICE-OHMS)

The NICE-OHMS technique combines both a cavity enhancement method, to increase the interaction length, and a frequency modulation (or wavelength modulation) technique to reduce the noise in the detected signal. The combination of these two methods results in a greatly improved sensitivity over other AS techniques, more specifically, it has been demonstrated that using the frequency modulation technique allows for shot-noise limited detection [62]. However, the technique is difficult to implement since the laser frequency must be locked to a cavity mode while performing measurements. So despite having a very high sensitivity the NICE-OHMS technique has found limited application outside of laboratory settings due to the relatively complex setup and operation. Recent developments have shown that implementing this technique with fiber optics has improved its performance and somewhat helped to reduce the complexity. The NICE-OHMS technique has demonstrated a minimum detectable absorption coefficient on the order of 10^{-11} cm^{-1} with an erbium fiber laser system [63].

1.6 CONCLUSION

As previously discussed, many of the NIR absorption spectroscopy techniques are capable of achieving similar sensitivities and prior to the selection of the ICAS technique the possibility of using a WMS-CRDS or WMS-ICAS combination system was explored. It was determined that roundtrip cavity losses, specifically losses associated with the gas cells, were much too high for the implementation of the CRDS technique, even if an attenuation compensation technique was employed [53]. Initial investigations into the proposed method for enhanced sensitivity were done for a combination WMS-ICAS system and basic

simulations for the WMS system were developed. However, due to technical problems with the development of the physical WMS component the focus was shifted to a system based purely on ICAS. Future investigations will look to include WMS with the ICAS system.

1.7   THESIS ORGANIZATION

This chapter was an overview of passive and active optical components, and different spectroscopy techniques. Chapter 2 describes the development, design, and characterization of the fiber laser system, as well as, its application for the detection of acetylene (C_2H_2) gas. Chapter 3 demonstrates the ability of the developed system to detect nitrous oxide (N_2O) gas at parts-per-billion by volume (ppbv). In Chapter 4 the application of a compact gas cell using a hollow-core photonic crystal fiber (HC-PCF) will be described. Chapter 5 describes preliminary work done with a system deployed for in field N_2O sample collection and Chapter 6 is the summary of the research performed and the future work.

CHAPTER 2

Development of an intracavity absorption spectroscopy system for the detection of acetylene (C_2H_2) gas

An intracavity absorption spectroscopy (ICAS) system based on an erbium doped fiber laser was investigated for the detection of acetylene (C_2H_2) gas. The ICAS system was developed for the detection of the R (5) and R (4) rotational lines in the $\nu_1 + \nu_3$ combination band of C_2H_2. The laser wavelength (1522.20 nm) was selected by a fiber Bragg grating (FBG) and was located between the R (5) and R (4) rotational lines, which correspond to 1522.060 nm and 1522.569 nm, respectively. The ICAS system was investigated using two different gas cells: a Herriott cell and a gas cell based on hollow-core photonic crystal fiber (HC-PCF). The sensitivity of the developed ICAS system was enhanced by including a fiber Bragg grating (FBG) in the cavity and by operating the laser at the threshold condition. A system for the detection of C_2H_2 will have applications in industrial process control, emissions monitoring, and chemical analysis, since the gas is commonly used in welding and the production of a number of chemicals [56;64].

This chapter will describe the basic principles behind the operation of the developed ICAS system and its application to detect C_2H_2 gas at different concentrations. The procedures

used to prepare different gas concentrations, as well as the method used for data analysis can be found in **Appendix A** and **Appendix B**, respectively.

2.1 ACETYLENE (C_2H_2) GAS

C_2H_2 is a symmetric linear molecule that has seven fundamental modes of vibration, two of those modes being doubly degenerate, which results in five unique vibrational modes: $v_1 = 3374$ cm^{-1} = 2963.841 nm, $v_2 = 1974$ cm^{-1} = 5065.856 nm, $v_3 = 3289$ cm^{-1} = 3040.438 nm, $v_4 = 612$ cm^{-1} = 16339.869 nm, $v_5 = 730$ cm^{-1} = 13698.630 nm [65]. Only the v_3 and v_5 vibrational modes are infrared (IR) active (**Figure 2.1**). Further, acetylene gas has a combination band, $v_1 + v_3$, of the fundamentals vibration bands v_1 and v_3 centered at 1525.212 nm, which overlaps with the ASE spectrum of the erbium-doped fiber (1520 nm to 1620 nm). **Figure 2.2** shows the P and R-branches of the absorption band spanning from about 1510 nm to 1540 nm [66]. Since the change in the dipole moment of the $v_1 + v_3$ band is parallel to the axis of symmetry there will be no Q-branch.
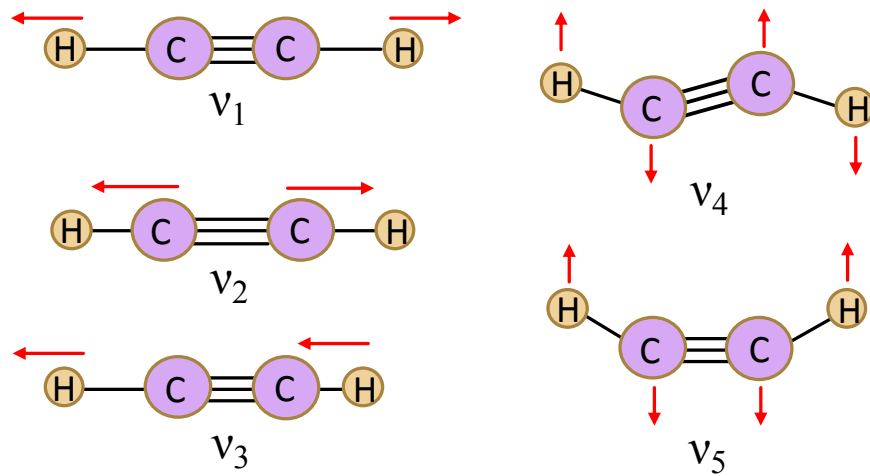
Figure 2.1: Fundamental vibrational modes of C_2H_2.
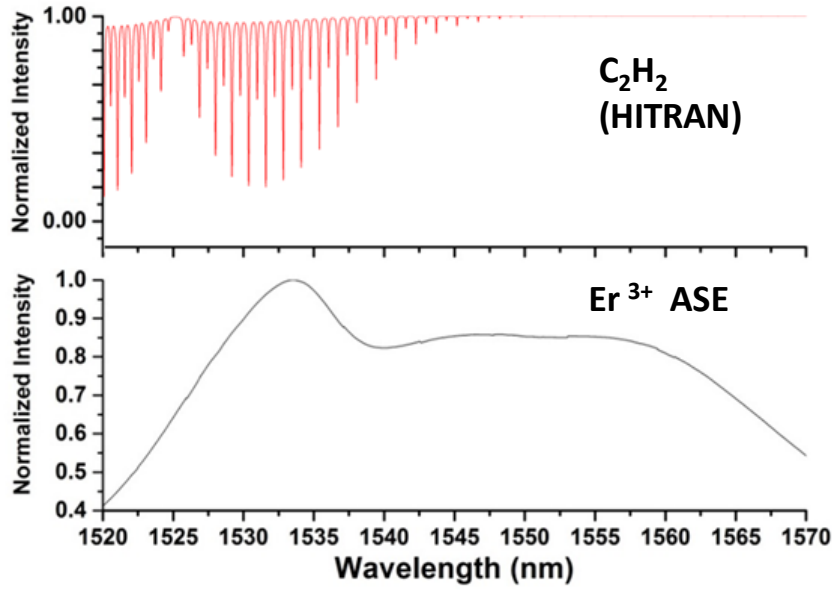
Figure 2.2: Theoretical $\nu_1 + \nu_3$ absorption band of C_2H_2 obtained from HITRAN [41] and the amplified spontaneous emission spectrum of erbium-doped fiber from 1520 nm to 1570 nm.

2.2 BACKGROUND THEORY

The fiber laser developed for this ICAS system was based on an erbium-doped fiber as the gain medium. Erbium-doped fiber lasers are commonly pumped with a 980 nm laser diode, and modeled as a quasi-three level laser system (**Figure 2.3**). The 980 nm laser radiation excites the erbium ions from their ground state manifold at $^4I_{15/2}$ to the upper state $^4I_{11/2}$ (pump band). The excited ions quickly relax from the $^4I_{11/2}$ level to $^4I_{13/2}$ manifold (metastable level) which is a non-radiative process [67]. The pump band ($^4I_{11/2}$ level) has a very short lifetime (~7 μs) in a silica host. The $^4I_{13/2}$ level is known as a metastable energy level because of the relatively long lifetime of ions, ~10 ms [68]. The transition from the $^4I_{13/2}$ level back to the ground state, results in an emitted photon with a wavelength in the 1.55 μm band [69].
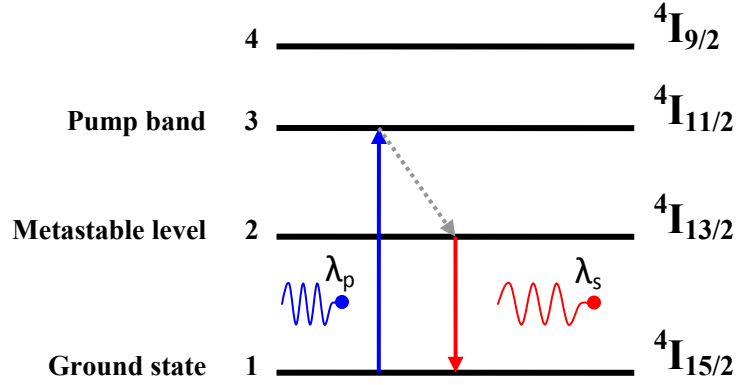
Figure 2.3: Energy levels of an erbium ion where the blue up-arrow signifies the excitation of the ion from the ground state to the pump band by a 980 nm photon (λ_p), the grey dotted downward-arrow indicates the nonradiative decay from the pump band to the metastable level, and the red down-arrow represents a decay with emission (λ_s) back to the ground state.

It has been demonstrated by Arsad et al. [46] that for an ICAS system using an erbium-doped fiber the change in intensity due to the absorption near the lasing wavelength can be improved under certain conditions. More specifically, Arsad et al. [46] demonstrated that when a laser is operated near threshold (cavity losses and gain are nearly equal) the absorption by low gas concentrations will have an enhanced effect. The laser rate equations can be used to describe the dynamics of an erbium-doped fiber laser and predict the pump rate required to reach the threshold condition of the laser. As previously mentioned the laser system can be modeled as a quasi-three level system, which implies the use of three rate equations,

$$\frac{dN_3}{dt} = -A_{32}N_3 + W_p(N_1 - N_3) \tag{2.1}$$

$$\frac{dN_2}{dt} = A_{32}N_3 - A_{21}N_2 - W_s(N_2 - N_1) \tag{2.2}$$

$$\frac{dN_1}{dt} = A_{21}N_2 - W_p(N_1 - N_3) + W_s(N_2 - N_1) \tag{2.3}$$

where A_{jk} is the decay rate per atom from level j to k, N_j represents the population per unit volume of the jth level manifold, W_p is the probability per unit time that an atom will be stimulated to transition from the ground energy level to the pump energy level or vice versa, and W_s is the probability per unit time that an atom will be stimulated to transition from the meta-stable level to ground level or vice versa. Further, the decay rate (A_{jk}) is inversely related to the lifetime, τ_{jk} by the relation,

$$A_{jk} = \frac{1}{\tau_{jk}} \tag{2.4}$$

Each term in the rate equations account for a change in that levels population, such as spontaneous and stimulated transitions. As previously shown in **Figure 2.3**, the three levels are comprised of the ground state, N_1, the metastable state, N_2, and the pump band, N_3. The total number of ions will remain constant and are expressed as,

$$N = N_1 + N_2 + N_3 \tag{2.5}$$

The rate equations at steady-state are,

$$\frac{dN_1}{dt} = \frac{dN_2}{dt} = \frac{dN_3}{dt} = 0 \tag{2.6}$$

and solving for the populations at the steady-state condition gives,

$$N_3 = \frac{W_p N_1}{A_{32} + W_p} \tag{2.7}$$

$$N_2 = \left(\frac{W_s(W_p + A_{32}) + W_p A_{32}}{(W_s + A_{21})(W_p + A_{32})} \right) N_1 \tag{2.8}$$

The high phonon energy in a silica glass allows for a multi-phonon transition to easily bridge the energy gap, resulting to very short lifetime for ions excited to the pump band. This leads

to a rapid, non-radiative decay from N_3 to N_2 which occurs much quicker than the pump rate into N_3, especially near or above threshold operation. Hence, for $A_{32} \gg W_p$ the population of N_3 is essentially zero.

$$N_3 = \frac{W_p N_1}{A_{32} + W_p} \approx \frac{W_p N_1}{A_{32}}$$ (2.9)

and N_2 becomes

$$N_2 = \left(\frac{W_p + W_s}{W_s + A_{21}} \right) N_1$$ (2.10)

thus the total population can be expressed as,

$$N = N_1 + N_2 + N_3 \approx N_1 + N_2$$ (2.11)

In order for laser action to occur population inversion must be reached, that is the population in the metastable state must be greater than the ground state, $N_2 > N_1$. Similarly, the threshold condition is reached when $N_2 = N_1$. It is convenient to express the difference in the populations of N_2 and N_1 in the form,

$$\frac{\Delta N}{N} = \frac{N_2 - N_1}{N} = \frac{W_p - A_{21}}{A_{21} + 2W_s + W_p}$$ (2.12)

and the difference in population levels describes: amplification ($N_2 > N_1$), threshold condition ($N_2 = N_1$), or decay ($N_2 < N_1$) within the cavity. Substituting **Equation (2.11)** in to **Equation (2.12)**, and assuming that below threshold the laser signal will be very small, $W_s \approx 0$ results in,

$$W_p N_1 = A_{21} N_2$$ (2.13)

Hence, under steady-state the threshold condition is reached when the pump rate is equal to the decay rate of the metastable level. The stimulated transition probability by the pump photons can be expressed as [45],

$$W_p = B_{13}\rho(v_p) = \frac{A_{21}c^2 I_{v_p}}{8\pi n^2 h v_p^{\,3}} g(v_p) \tag{2.14}$$

where B_{13} is absorption probability, $\rho(v_p)$ is the spectral energy density, n is the refractive index of the medium, I_v is the intensity, v_p is the pump photon frequency, and $g(v)$ is the lineshape function. A more general expression for the stimulated transition probability is,

$$W = \frac{c^2 I_v}{8\pi n^2 h v^3 \tau} g(v) \tag{2.15}$$

where the level lifetime was substituted in for the spontaneous decay rate using relation **Equation (2.4)**. The net ASE power at the end of the gain fiber from the induced transitions, can be expressed as,

$$P_{ASE}(v) = (N_2 - N_1)W h v V = (N_2 - N_1)\frac{c^2 I_v}{8\pi n^2 h v^3 \tau} g(v) h v V = \gamma(v) I_v V \tag{2.16}$$

$$\gamma(v) = (N_2 - N_1)\frac{c^2}{8\pi n^2 v^2 \tau} g(v) \tag{2.17}$$

where V is the volume which the radiation mode occupies and $\gamma(v)$ is the gain constant. With each roundtrip the ASE power in the cavity will be affected by the gain medium, cavity loss, and absorption loss. Cavity losses can be attributed to different sources in fiber laser cavities, such as fiber splices, scattering, or bends in the fiber. The amplification experienced from each pass through the gain fiber is given by the gain constant,

$$G(v) = e^{\gamma(v)l} \tag{2.18}$$

The cavity losses can be combined into a single loss term, an attenuation factor, k, which is expressed as,

$$k = e^{-\alpha_L L} = e^{-\alpha_c} \tag{2.19}$$

where α_L is the attenuation per unit length (dB/length), L is the length of the cavity, and α_c is the total cavity loss. Further, when a light absorbing sample is placed within the cavity, as in an ICAS system, a term for absorption must be included. From the Beer-Lambert's law the loss due to absorption from each trip is,

$$\Lambda_{gas} = e^{-A(v)} = e^{-\alpha_g(\lambda)CL_{cell}} \tag{2.20}$$

where $A(v)$ is the frequency dependent absorbance of the analyte, which is related to gas absorption coefficient, $\alpha_g(\lambda)$, sample concentration, C, and length of the gas cell, L_{cell}. Further, a factor R can be included to represent the coupling loss due to mirrors, fiber Bragg gratings, and fiber couplers. The output power, including the terms after a single roundtrip is given by,

$$P(v) = R \cdot P_{ASE}(v) + [e^{\gamma(v)l} \cdot e^{-\alpha_c} \cdot e^{-A(v)}]R \cdot P_{ASE}(v) \tag{2.21}$$

For multiple roundtrips the expression for the output power is given by,

$$P(v) = R \cdot P_{ASE}(v)[1 + (e^{\gamma(v)l} \cdot e^{-\alpha_c} \cdot e^{-A(v)}) + (e^{\gamma(v)l} \cdot e^{-\alpha_c} \cdot e^{-A(v)})^2$$
$$+ (e^{\gamma(v)l} \cdot e^{-\alpha_c} \cdot e^{-A(v)})^3 + ...]$$

$$\tag{2.22}$$

Hence, by using the relation for a geometric power series, $\sum_{n=0}^{\infty} ar^n = \dfrac{a}{1-r}$, the output power from the cavity can be written as,

$$P(v) = \frac{R \cdot P_{ASE}(v)}{1 - e^{\gamma(v)l} \cdot e^{-\alpha_c} \cdot e^{-A(v)}} = \frac{R \cdot P_{ASE}(v)}{1 - e^{\gamma(v)l - \alpha_c} \cdot e^{-A(v)}} \tag{2.23}$$

Following Arsad et al. [46], as the gain approaches threshold the difference between gain and cavity loss will approach zero and can be approximated as,

$$e^{\gamma(v)l - \alpha_c} \approx 1 - (\alpha_c - \gamma(v)l) \tag{2.24}$$

Likewise, when the absorbance due to the analyte is very small leads to,

$$e^{-A(v)} \approx 1 - A(v) \tag{2.25}$$

$$P(v) \cong \frac{R \cdot P_{ASE}(v)}{1 - [1 + (\gamma(v)l - \alpha_c)][1 - A(v)]} = \frac{R \cdot P_{ASE}(v)}{(\alpha_c - \gamma(v)l)[1 + \dfrac{A(v)}{\alpha_c - \gamma(v)l} - A(v)]} \tag{2.26}$$

The ratio of the output powers for an ICAS system with and without an absorbing sample, which is equivalent of P_{out} and P_{in} in the Beer-Lambert relation gives,

$$\frac{P_{gas}}{P_{without}} = \frac{P_{out}}{P_{in}} = \frac{1}{1 + \dfrac{A(v)}{\alpha_c - \gamma(v)l} - A(v)} \cong \frac{1}{1 + \dfrac{A(v)}{\alpha_c - \gamma(v)l}} \tag{2.27}$$

As the system approaches threshold the difference between the gain and cavity loss approaches, but never reaches, zero, $\alpha_c - \gamma(v)l \ll 1$, and a sample with a very low absorbance is present such that $\alpha_c - \gamma(v)l > A(v)$ and $\dfrac{A(v)}{\alpha_c - \gamma(v)l} \ll 1$ results in,

$$\frac{P_{out}}{P_{in}} \cong 1 - \frac{A(v)}{\alpha_c - \gamma(v)l} = 1 - \frac{\alpha_g(v)CL_{cell}}{\alpha_c - \gamma(v)l} \tag{2.28}$$

The Beer-Lambert's Law for low absorbance can be expressed as,

$$\frac{P_{out}}{P_{in}} = e^{-A(v)} \approx 1 - A(v) = 1 - \alpha_g(v)CL_{eff} \tag{2.29}$$

where L_{eff} is the effective interaction length. By equating **Equation (2.28)** and **Equation (2.29)** results in a relation for length enhancement,

$$1 - \alpha_g(v)CL_{eff} = 1 - \frac{\alpha_g(v)CL_{cell}}{\alpha_c - \gamma(v)l} \tag{2.30}$$

$$L_{eff} = \frac{L_{cell}}{\alpha_c - \gamma(v)l} \tag{2.31}$$

Further, operating an ICAS system at threshold allows the ASE radiation to make multiple round trips through the gas sample in the cavity and enhance the interaction length.

In general, the spectral sensitivity for an ICAS system can be defined by the increase in the interaction path length which is determined by [48],

$$L_{eff} = \frac{A(v)}{\alpha_g(v)} \tag{2.32}$$

The detection limit for an ICAS system can be calculated using,

$$\alpha_{g\,min}(v) = \frac{A_{min}(v)}{L_{eff\,max}} \tag{2.33}$$

where A_{min} is a noise equivalent absorbance and $L_{eff\,max}$ is the maximum spectral sensitivity length. For a very low concentration, or weak absorption, where a very small change in intensity occurs, the absorbance can be approximated by,

$$A(\nu) = \ln \frac{I_o}{I} \approx \frac{\Delta I}{I_o} = \frac{\Delta P}{P_o} \qquad (2.34)$$

By including a fiber Bragg grating in the cavity, see **Figure 2.4**, the feedback will be much stronger for the longitudinal modes present within the FBG bandwidth. This will further enhance the system sensitivity due to an improved finesse of the cavity. This results in a larger number of passes through the sample for the wavelengths reflected by the FBG compared to the rest of the erbium ASE wavelengths.
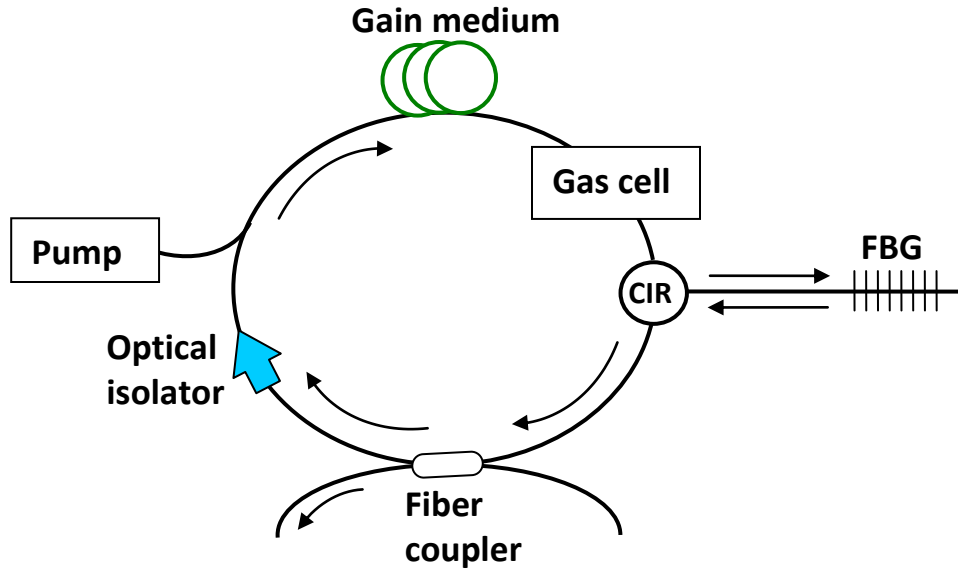
Figure 2.4: A simple ring-cavity with a fiber Bragg grating (FBG).

The reflection bandwidth of a FBG is defined by [70],

$$\Delta \nu_{FBG} = \frac{c}{\pi n_{eff} L_{FBG}} \sqrt{(\kappa L_{FBG})^2 + \pi^2} \qquad (2.35)$$

where κ is a coupling coefficient, L_{FBG} is the length of the grating, n_{eff} is the effective refractive index, and c is the speed of light in vacuum. In general, a fiber laser consists of a large number of longitudinal modes due to a long cavity length. The number of modes

present in the cavity increases with the cavity length, L, and the separation between longitudinal modes in a ring cavity is given in frequency domain by [3],

$$\Delta v = \frac{c}{nL} \tag{2.36}$$

and in wavelength domain by,

$$\Delta \lambda = \frac{\lambda^2}{nL} \tag{2.37}$$

Though the cavity can support many longitudinal modes, only the ones that exist within the gain bandwidth of the gain medium will be amplified, as shown in **Figure 2.5**.
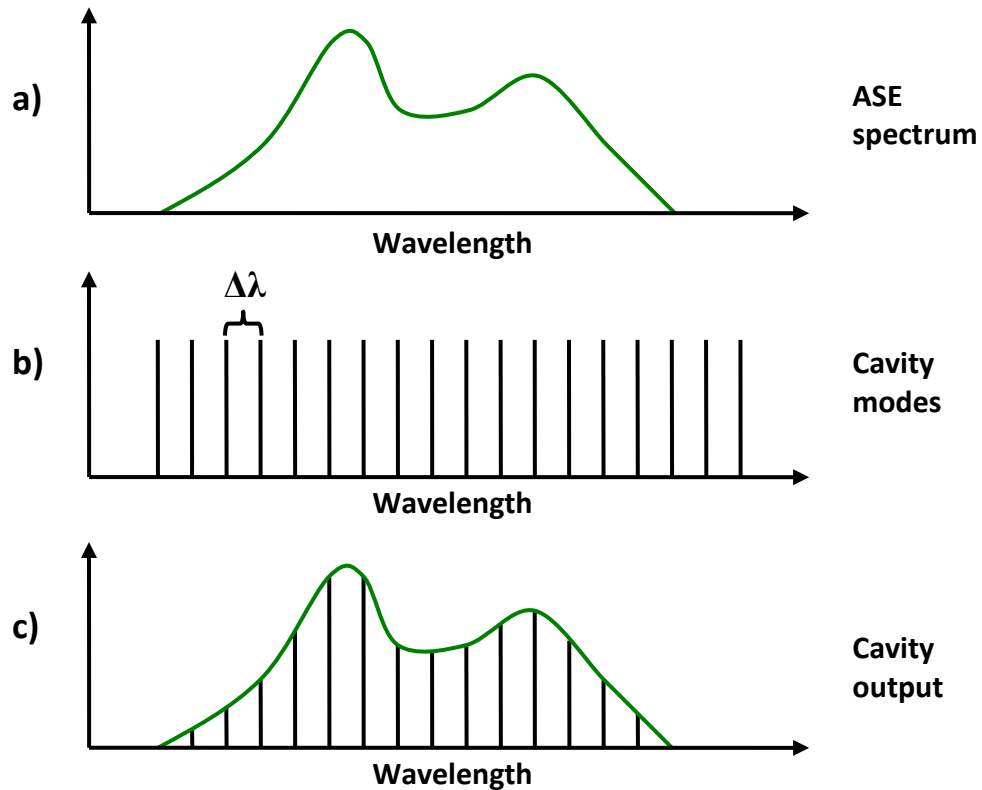
Figure 2.5: (a) is the emission spectrum of the gain medium, **(b)** shows the cavity modes and **(c)** the laser output will only amplify modes within the gain profile.

Furthermore, from **Equation (2.36)** the number of modes oscillating within the FBG bandwidth can be determined by,

$$M = \frac{\Delta \nu_{FBG}}{\Delta \nu}$$

(2.38)

These modes within the grating bandwidth will get maximum feedback and amplification compared to the other modes outside of the bandwidth. Since erbium-doped fiber is a homogenous gain medium all the modes within the low loss region of the grating bandwidth will be amplified. At threshold the number of longitudinal modes within the FBG bandwidth will have similar intensities, and form a relatively flat intensity region. The modes in this region are very sensitive to any change in the cavity resonant condition. When the laser operates at threshold and sample absorption occurs at or near the flat region, the modes will experience an increased loss even from very low concentrations [46]. The presence of the FBG inside the cavity increases the stability of the cavity modes within the FBG bandwidth, making it easier to operate the laser close to threshold. If the input pump crosses the threshold value the system will start lasing, and the laser will contain a single mode, or a few modes, which reduces the sensitivity.
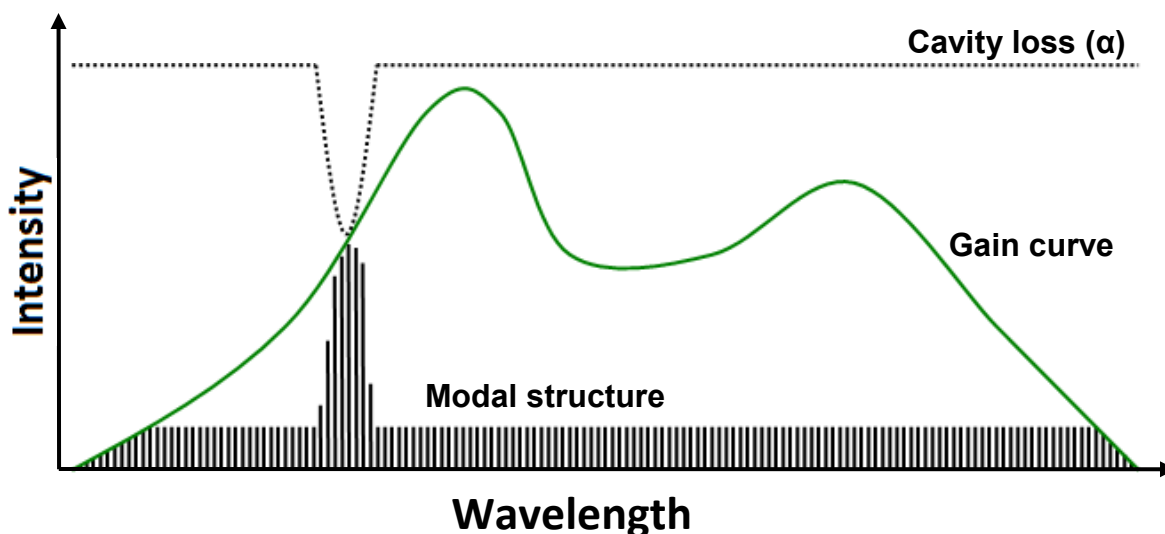
Figure 2.6: Modal output of the laser when a FBG is incorporated into the cavity. The dip in the cavity loss corresponds to the FBG.

2.3 GAS CELLS

Two different types of gas cells were used in the experiments throughout this dissertation: **(i)** a multi-pass Herriott cell and **(ii)** a gas cell based on hollow-core photonic crystal fiber (HC-PCF). The Herriott gas cell was formed with two spherical mirrors separated by ~ 0.42 m. There were 72 reflections between the mirrors that resulted in an effective path length of ~ 30 m. This cell required a sample volume of 0.9 L. The second cell was based on HC-PCF (HC19-1550, 20 µm core diameter, NKT Photonic crystal fibers), where the core of the fiber was filled with the gas analyte. Two variations of the HC-PCF cell were developed and will be discussed in the following section. The final design for the HC-PCF cell housed each end of the HC-PCF in aluminum cells. The aluminum cells had anti-reflection coated quartz windows for coupling the light into and out of the hollow core fiber while keeping it isolated from the atmosphere. The cells were equipped with gas inlets and outlets to allow the gas samples (e.g., acetylene) to be diffused into and evacuated out of the hollow-core fiber **(Figure 2.7)**. The experiments with C_2H_2 were performed using HC-PCF of two different

lengths, 6 m and 20 m. The volume of gas required for the HC-PCF cell was a few milliliters. Hollow-core fiber is appealing to use as a gas cell, since it allows for a very high degree of radiation–sample interaction while requiring very small sample volume.
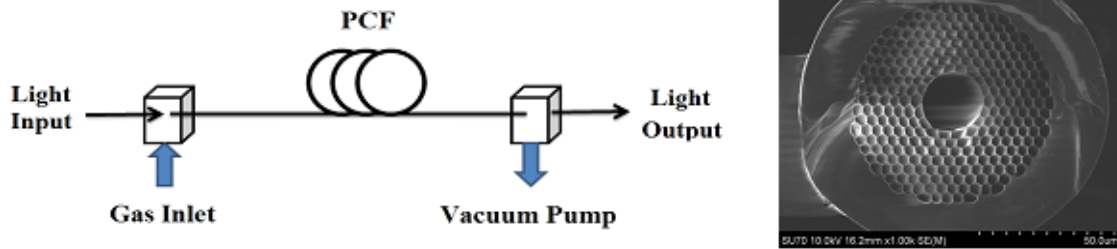
Figure 2.7: Schematic of the hollow-core photonic crystal fiber gas cell (left) and the scanning electron microscope image of the actual fiber used (right).

2.4 DEVELOPMENT OF HC-PCF GAS CELLS

2.4.1 GAS CELL 1

Two variations of a HC-PCF gas cells were constructed. The basic structure of the first HC-PCF gas cell was a 12" by 10" by 5" rectangular steel box which could house the entire photonic crystal fiber (**Figure 2.8**). The steel box was fitted with a gas inlet and outlet, and two anti-reflection (AR) coated quartz windows. An optical bread board was welded to the inside base of the gas cell so that optical components could be securely fastened inside the cell (**Figure 2.9**). The ends of the hollow-core fiber were mounted on optical fiber clamps [HFF003, Thorlabs, USA] close to the quartz windows such that the cavity radiation could be coupled into and out of the HC-PCF through the quartz windows. The amplified spontaneous emission (ASE) was coupled from a single mode fiber through a combination of lenses that were mounted on three-axis micro-translation stages outside of the cell through the quartz windows into the HC-PCF. The coupling efficiency for this gas cell was ~75%.
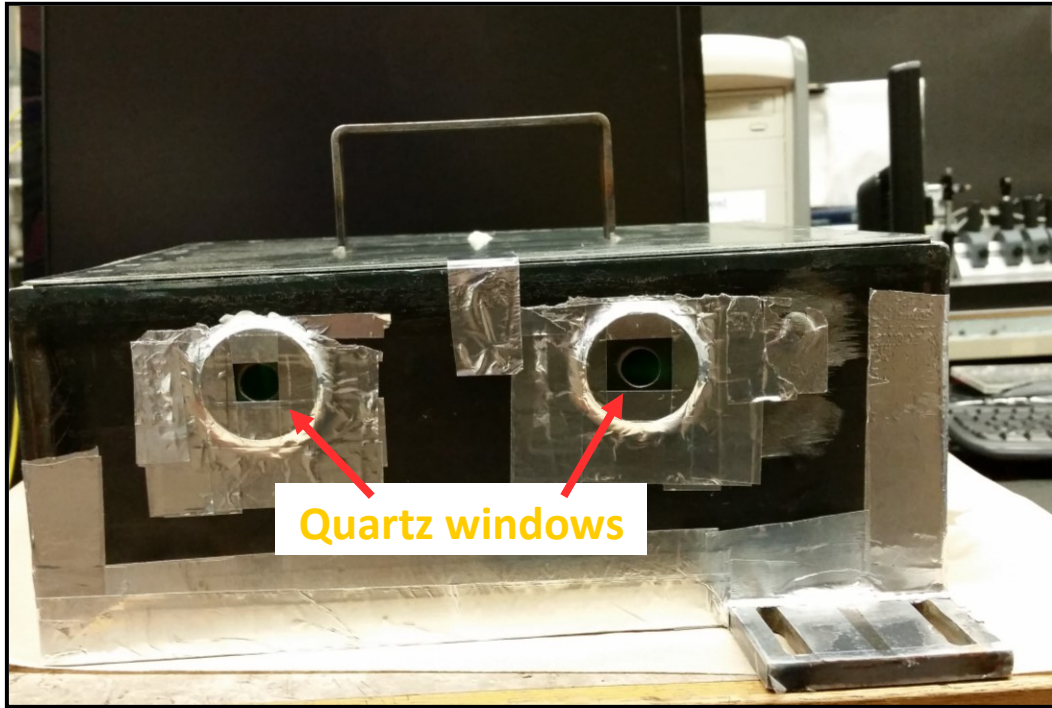
Figure 2.8: Front view of the steel gas cell with AR-coated quartz windows.
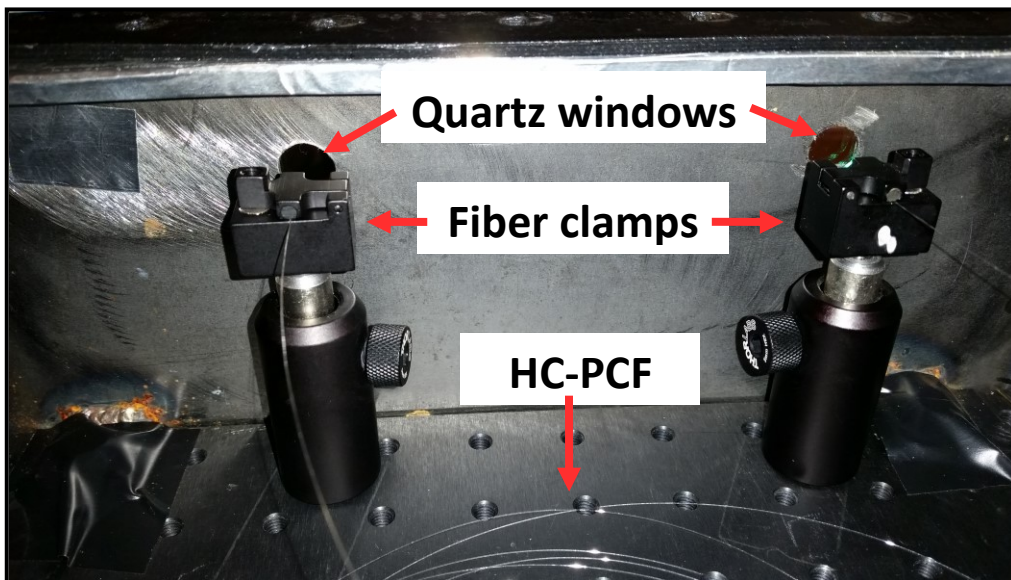
Figure 2.9: Internal view of steel gas cell with the HC-PCF mounted on the optical board in front of the transmission windows.

Since the HC-PCF was completely confined within the cell it was possible to evacuate and fill the HC-PCF from both ends. Gas samples were diffused into the hollow core fiber by evacuating the entire gas cell, and then filling it with the sample. This cell was used in a direct absorption spectroscopy (DAS) system to determine the evacuation and fill time for a 6 m long piece of HC-PCF (**Figure 2.10**).
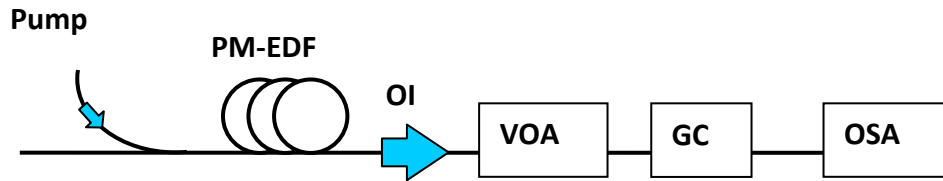
Figure 2.10: Experimental configuration of the DAS system. PUMP: 980 nm pump laser; PM-EDF: Polarization-maintaining erbium-doped fiber; VOA: Variable optical attenuator; GC: Gas cell; and OSA: Optical spectrum analyzer

The laser output from the DAS system was monitored while the cell was filled with 1% C_2H_2. As the gas sample would slowly diffuse through the fiber the absorption lines would become more prominent until the fiber was filled, and the loss at the absorbing wavelengths remained constant. It was found that evacuation and filling time of HC-PCF with this cell design was too long. The time required for the whole processes was approximately 3 hours for a 6 m long HC-PCF. This result was consistent with the fill times reported in the literature [71]. Further, the rectangular cell required a large sample volume to fill it, ~10 L. Since the entire HC-PCF is surrounded by the gas sample the diffusion rate into the core of the fiber could be increased by drilling holes into the length of the hollow core, which is one of the advantages of this cell design [72;73]. Experiments with this cell were only performed with 6 m long HC-PCF, as filling and evacuation time for longer lengths of fiber would be unreasonably long for the intended applications.

2.4.2 GAS CELL 2

In order to address the limitations presented with Gas Cell 1, a smaller gas cell configuration was developed which would allow for a faster filling and evacuation rate. This gas cell system was formed by two separate aluminum cells, which housed each end of the HC-PCF, as shown schematically in **Figure 2.11** and the actual system in **Figure 2.12**. The ASE was coupled into and out of the HC-PCF using a lens assembly formed with two lenses mounted on a 3-axis translation stage. One lens would collimate the cavity radiation and the other lens would focus the collimated beam into the core of the HC-PCF or vice versa **(Figure 2.11)**.
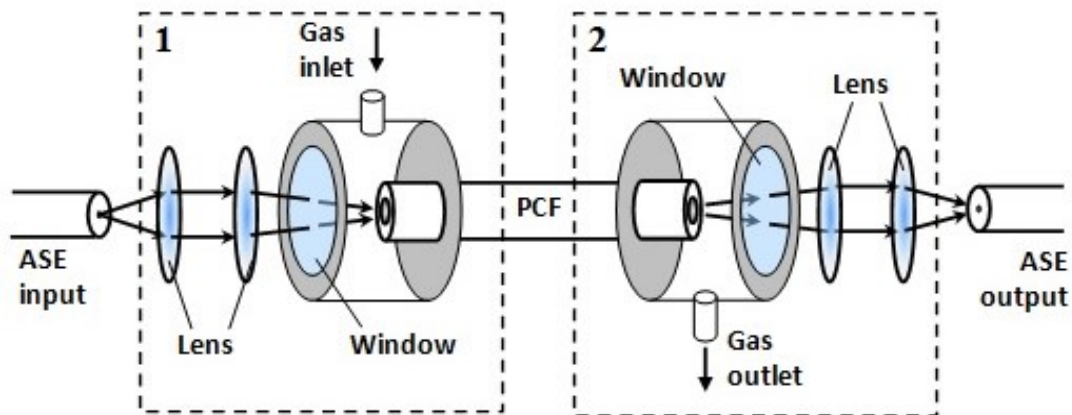
Figure 2.11: Schematic of the gas cell configuration for coupling light into and out of the HC-PCF.
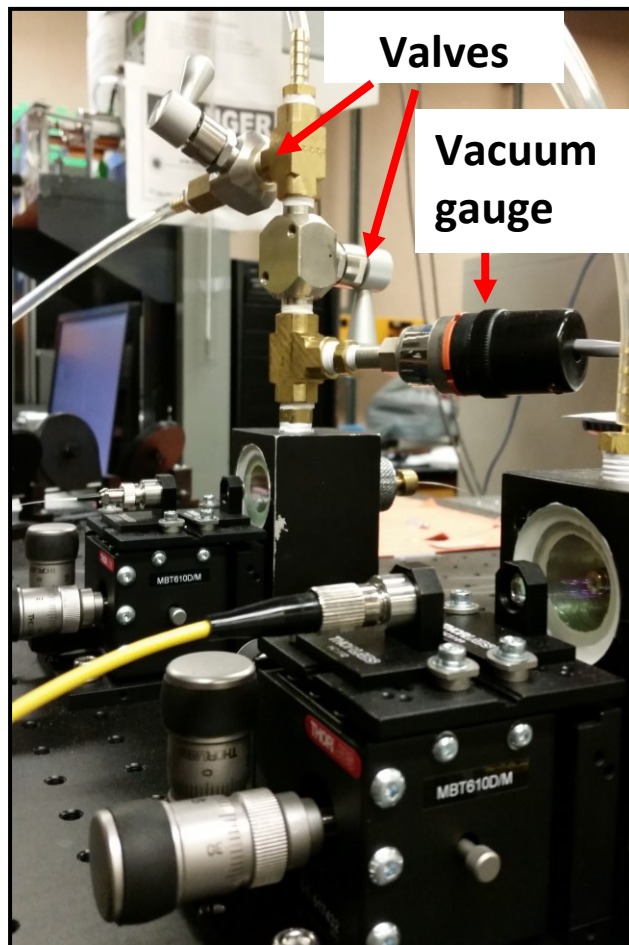
Figure 2.12: Gas cell configuration, showing both aluminium housing cells and the 3-axis micro-translation stages. The yellow cable is a single mode fiber connected to a collimating lens. A vacuum gauge and two ball valves are connected to the top of the further cell.

Each cell was machined from 2" by 2" by 4" aluminum block with two threaded inputs to accommodate a barbed tube fitting and the hollow-core fiber holder, as well as a 1" recessed hole to house the quartz window. The machining inside the cell was minimized so that the final internal volume would only be a few milliliters for each cell. The quartz windows had an AR coating so that losses would be minimized when the light was coupled into and out of the HC-PCF. One of the aluminum cells was fitted with two ball valves and a vacuum gauge (**Figure 2.12**). The valves prevented any back flow from occurring when the vacuum was

switched off and allowed the gas sample access to the cell. A specially designed O-ring and cap developed in house, was used to eliminate leakage through the fiber chuck at the back of the aluminum blocks. As the cap was threaded onto the end of the fiber holder the o-ring compressed around the fiber forming an air tight seal. **Figure 2.13** is a top down view of the actual fiber chuck with the cap and o-ring configuration.
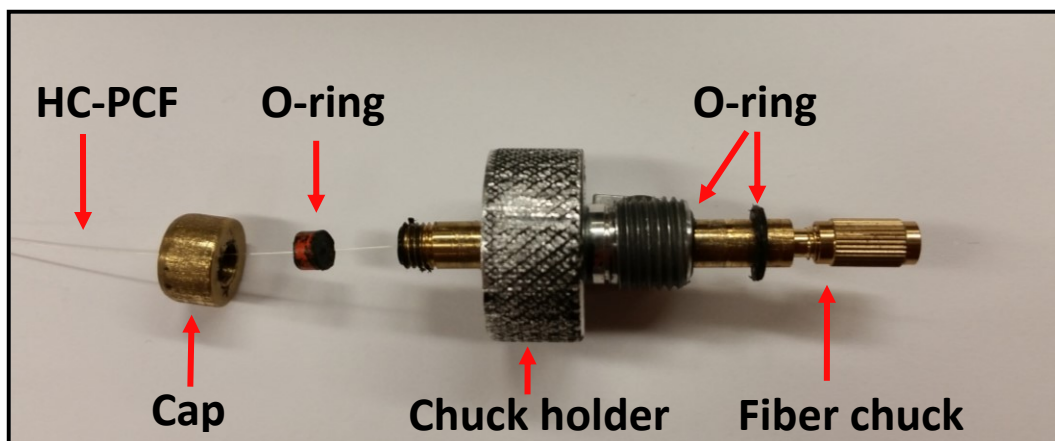
Figure 2.13: Top down view of HC-PCF holder disassembled.

The hollow-core fiber was evacuated using a Welch 8907 two-stage, rotary-vane vacuum pump. The filling time was improved by initially evacuating both cells and the HC-PCF, then maintaining a high vacuum level in one cell while the other cell was filled with the gas sample at atmospheric pressure. The configuration of the evacuation and filling system is shown in **Figure 2.14**. The advantage of this design was that both cells could be evacuated or filled simultaneously, or filled from one side and evacuated from the other.
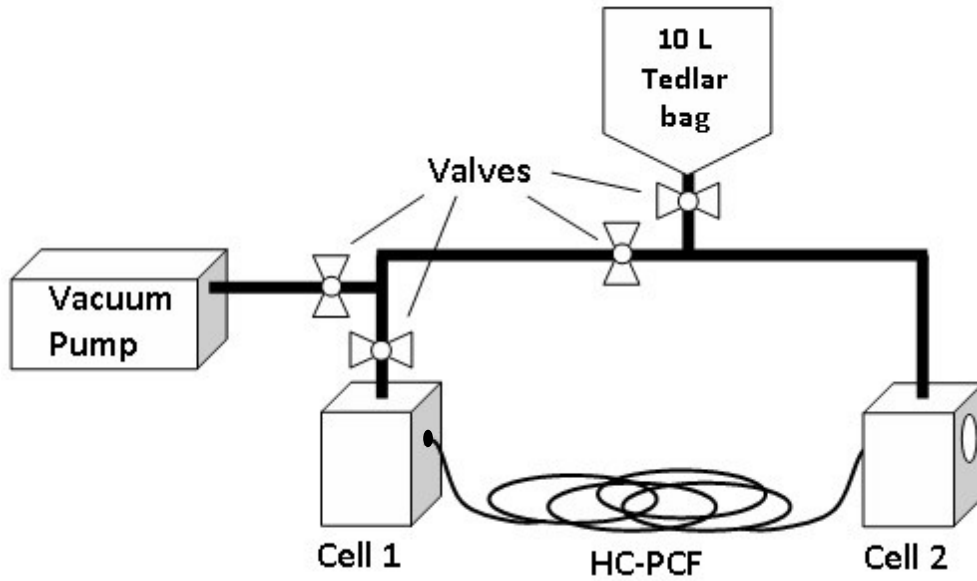
Figure 2.14: Configuration of the evacuation and filling system.

It was important to maintain a large pressure difference between the two cells so that a quick and steady gas flow through the hollow-core fiber could be achieved. Once the sample was pulled through the length of the fiber, the pump was shut off and the sample was allowed to diffuse into the fiber from the evacuated side and equilibrate to atmospheric pressure. The total time required to evacuate and fill a 20 m long PCF was approximately 80 minutes, meaning a fairly slow response time, but greatly improved from that of **Gas Cell 1**. The experiment was also performed with a 40 m long HC-PCF and total evacuation and filling time was ~4 hours.

2.5 RESULTS AND DISCUSSION

The experimental setup was formed in a ring cavity configuration (**Figure 2.15**) using a polarization-maintaining erbium-doped fiber (PM-EDF) as the gain medium and the HC-PCF based gas cell (**Gas Cell 2**) with a 6 m long fiber (**Figure 2.7**). It should be noted that all the

following HC-PCF experiments in this dissertation were performed with HC-PCF based **Gas Cell 2**, unless otherwise specified. The gain fiber was pumped using a 980 nm diode laser through a 980/1550 nm wavelength division multiplexer (WDM). Optical isolators insured unidirectional wave propagation and prevented spatial-hole burning effect within the cavity. A variable optical attenuator (VOA) was used to obtain the desired threshold condition by adjusting the total cavity loss. The polarization state of the light in the cavity was adjusted using an all fiber polarization controller to improve the stability.
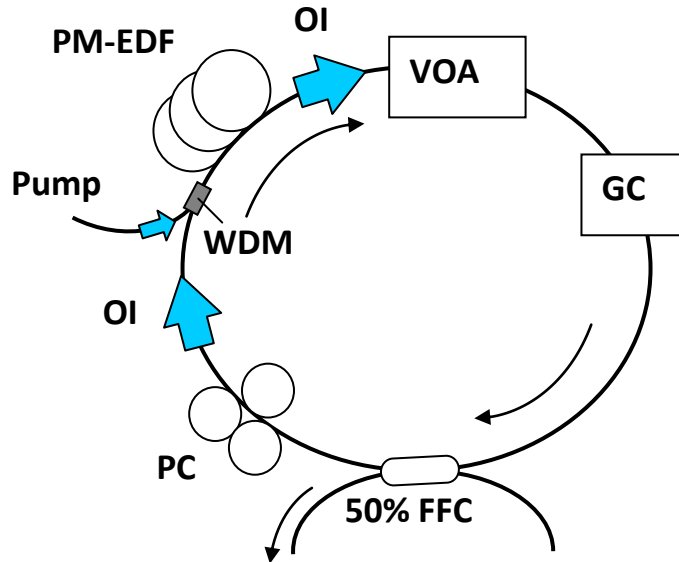
Figure 2.15: Schematic of the ICAS system. PUMP: 980 nm pump laser; PM-EDF: Polarization-maintaining erbium-doped fiber; VOA: Variable optical attenuator; FFC: 50% Fused fiber coupler; PC: All fiber polarization controller, GC: Gas cell, WDM: wavelength division multiplexer coupler, and OI: Polarization independent optical isolator.

The system was operated at a balanced condition as described by Arsad et al. [46]. The pump current was adjusted so that the system was operating near threshold condition. The VOA was then adjusted in order to obtain the balanced condition between the 1535 nm and 1555 nm region of the ASE spectrum. The balanced condition occurred when the gain in each region was nearly equal and occurs at approximately 60% population inversion in

erbium-doped fiber [46]. Once the cavity was at the balanced condition any small change in the attenuation would cause the laser wavelength to switch from the 1535 nm region to the 1555 nm region or vice versa. This technique takes advantage of the increased sensitivity when the system is operated near threshold. All longitudinal modes within the laser bandwidth are in competition to lase, if a loss is introduced to some of these longitudinal modes (e.g., due an absorption line) the cavity resonance condition will change and lasing will shift to different modes. At the balanced condition, by increasing the loss of the modes in the 1535 nm region with the VOA, the laser wavelength shifts to the 1555 nm region (**Figure 2.16**). The experiment was performed with a concentration of 5000 ppmv of C_2H_2 in the 6 m HC-PCF gas cell. This cell had a coupling efficiency of ~55%. The filling process began by evacuating the HC-PCF from both ends of the fiber using a Welch 8907 two-stage, rotary-vane vacuum pump for ~30 minutes down to ~0.2 mbar, the minimum vacuum levels the system could reach. After evacuating the system for 30 minutes, the sample or background gas was injected into the one cell while the other was continuously evacuated for ~30 minutes. The sample was then allowed to diffuse into the HC-PCF from both ends until the system reached equilibrium; this typically took ~20 minutes. Although techniques which reduce the evacuation and filling time have been demonstrated, such as drilling holes over the fiber length, they were not employed for this research [74]. **Figure 2.17** demonstrates that the loss due to absorption by C_2H_2 gas forced the laser oscillation to switch from 1535 nm region to the 1555 nm region. Absorption lines from transitions related to the P-branch were clearly visible in the output spectrum [75]. The spectra were recorded using an ANDO AQ6317B optical spectrum analyzer.
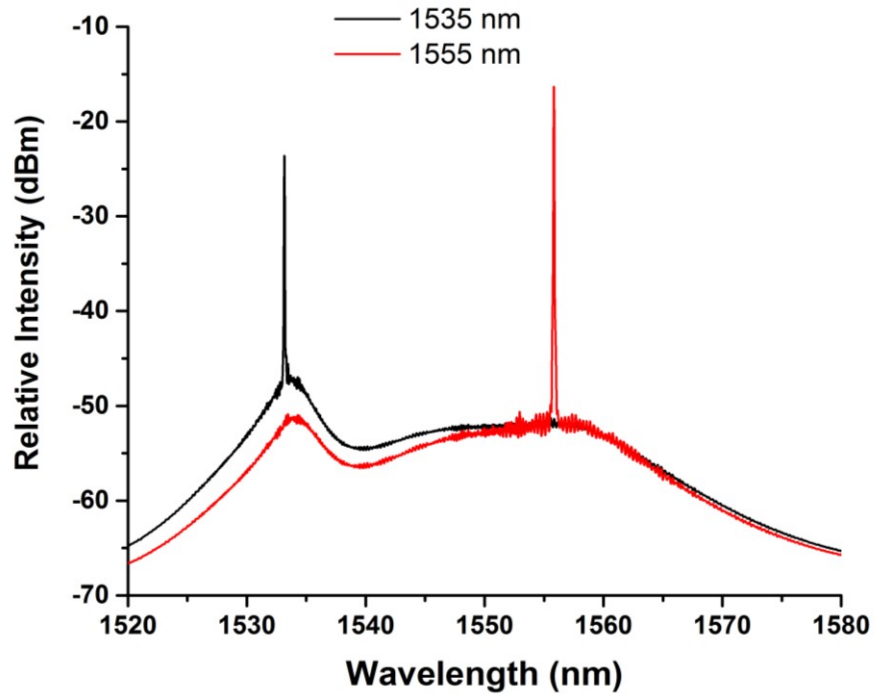
Figure 2.16: Cavity output before the attenuation has been increased in the 1535 nm region with the VOA (BLACK) and after the attenuation has been increased (RED).
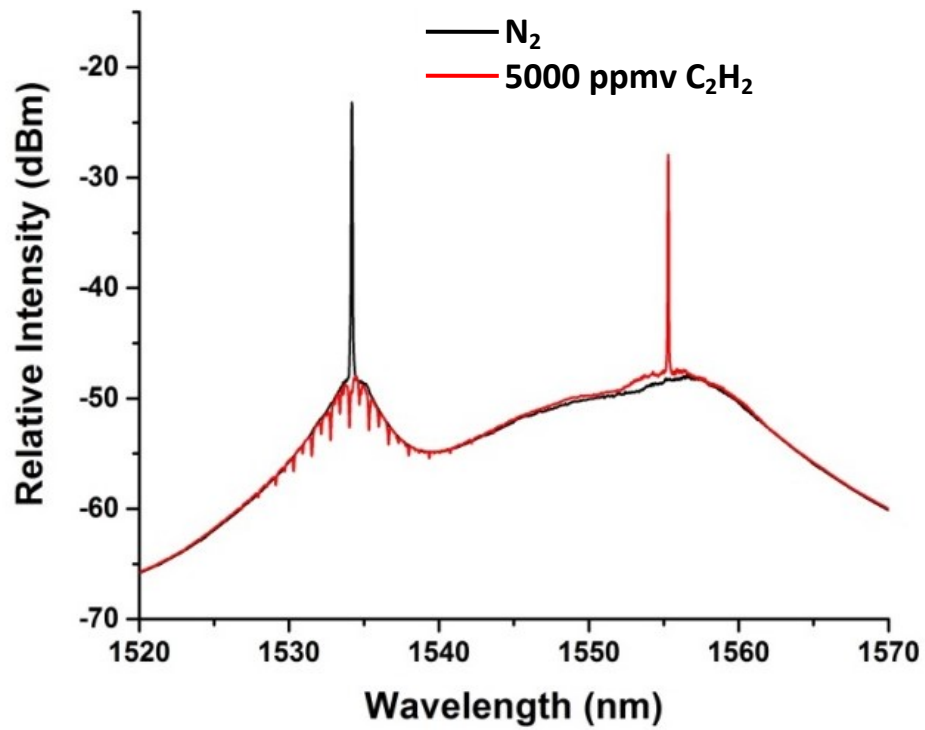
Figure 2.17: Output of the system obtained using the 6 m length of HC-PCF as the gas cell inside the cavity filled with 0.5% acetylene gas. The absorption in the 1535 nm region forced the laser wavelength to move to the 1555 nm region.

In general, the laser in this configuration was unstable and suffered from mode-hopping. This was due to the long cavity length which supported very closely spaced longitudinal modes. A method was developed which modified the above technique to improve sensitivity and stability at a specific region. **Figure 2.18** shows the modified laser resonator, which includes a fiber circulator, saturable absorber, fiber Bragg grating, and an optical isolator. The FBG which was incorporated had a center wavelength of 1522.22 nm, peak reflectivity of 85.16%, and a FWHM (full-width half-maximum) of 0.168 nm. The saturable absorber together with the FBG formed a dynamic transient grating resulting from the standing wave pattern formed in the new cavity portion that helped to reduce mode-hopping and improved the stability of the system [76].
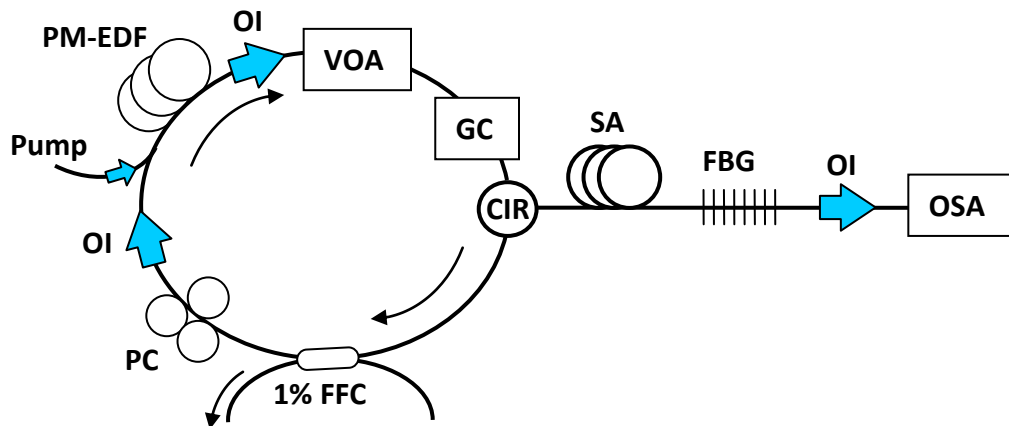
Figure 2.18: Schematic of the ICAS system. PUMP: 980 nm pump laser; PM-EDF: Polarization-maintaining erbium-doped fiber; VOA: Variable optical attenuator; SA: Saturable absorber; FBG: Fiber Bragg grating; OSA: Optical spectrum analyzer; CIR: Polarization independent optical circulator; FFC: 2×2 Fused fiber coupler; PC: All fiber polarization controller, GC: Gas cell, and OI: Polarization independent optical isolator.

As previously mentioned, an area with little variation between longitudinal mode intensities was created within the reflection bandwidth of the FBG in the ASE spectrum, similar in concept to the balanced condition described by Arsad et al. [46]. More

specifically, this area was centered at 1522.22 nm and between the rotational absorption lines R (5) and R (4) of C_2H_2, at 1522.060 nm and 1522.569 nm, respectively, in the R-branch of the acetylene $\nu_1 + \nu_3$ combination band (**Figure 2.19**) [75].
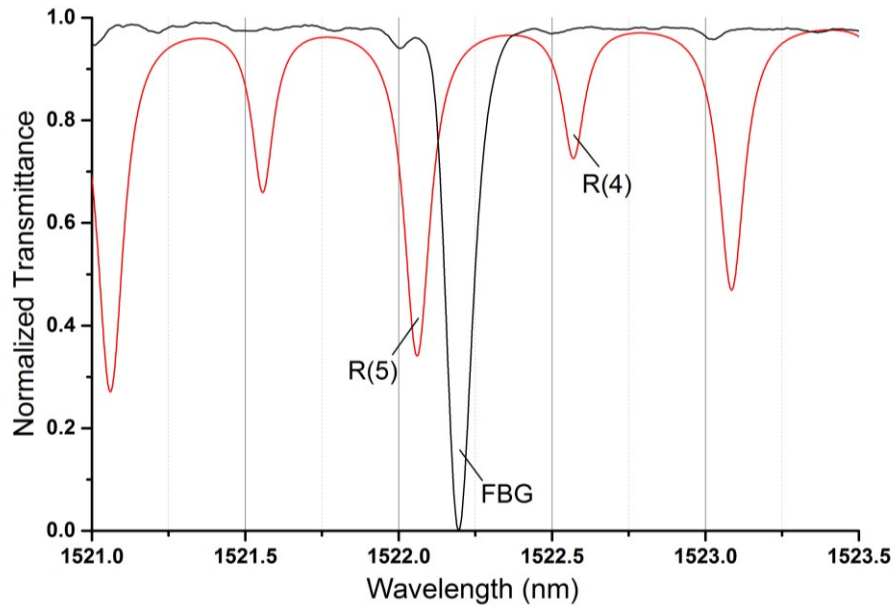
Figure 2.19: Theoretical C_2H_2 (RED) from HITRAN, with the experimental 10ppmv C_2H_2 data (BLACK), showing the overlap of the rotational absorption lines with the fiber Bragg grating.

When operated at threshold the longitudinal modes within the FBG bandwidth have a very high sensitivity to any losses caused by absorption of the R (5) rotational line and, to a lesser extent, the R (4) rotational line. As described above, the modes within the FBG bandwidth will make multiple passes inside the cavity, and thus through the acetylene sample. When the system was operated at the threshold position, as demonstrated in **Figure 2.20**, the gain and loss of the cavity at the FBG wavelength were in equilibrium. At this equilibrium position any losses occurring within the grating bandwidth become greatly enhanced.
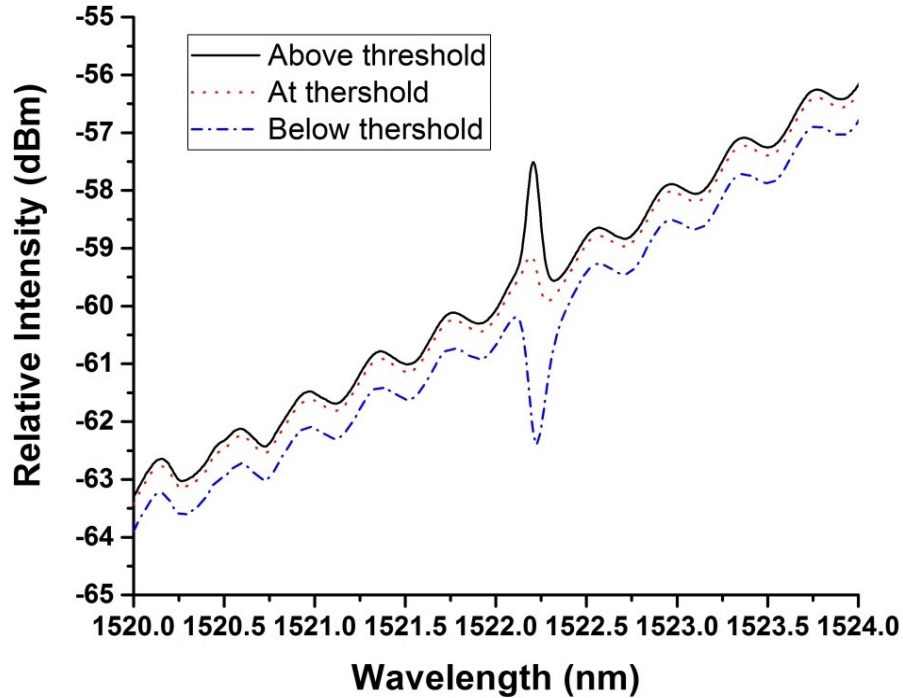
Figure 2.20: Output spectrum of the system with FBG in the cavity above, at, and below threshold condition for the Herriott cell filled with N_2 gas. An interference pattern resulting from the etalon effect at one of the cells quartz windows is visible.

The experiments were performed using the configuration shown in **Figure 2.18**, with the HC-PCF gas cell based and a 20 m length of HC-PCF. After filling the cell with N_2, the laser was adjusted to a stable threshold condition and 10 spectra were collected. The cell was then filled with a C_2H_2 sample, and 10 additional spectra were collected. C_2H_2 gas concentrations from 500 ppbv to 5000 ppmv were tested in the system, for higher concentrations (>1000 ppmv) the absorption signal appeared to be saturated with very little change in the absorption spectra. **Figure 2.21** is the spectra obtained with the optical spectrum analyzer for N_2 as background, and C_2H_2 of 100 ppmv concentrations (1515 nm to 1545 nm).
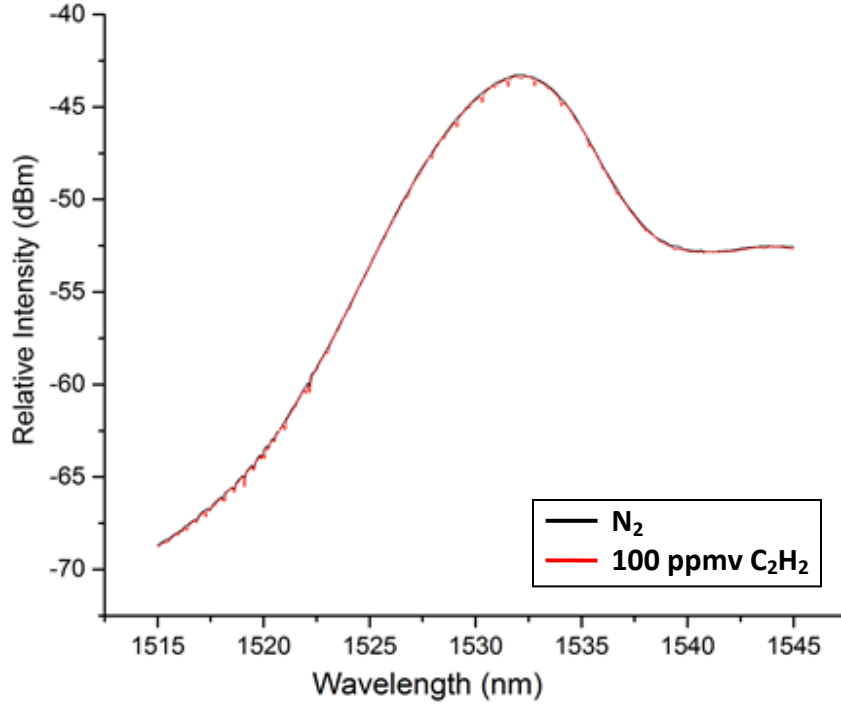
Figure 2.21: Averaged output spectrum of N_2 and of 100 ppmv C_2H_2 in the HC-PCF gas cell before subtraction.

Figure 2.22 and **Figure 2.23** are the absorption spectra obtained by subtracting averaged N_2 scans from averaged scans of C_2H_2 for concentrations of 10 ppmv and 100 ppmv, as described in **Appendix B**. It can be seen in **Figure 2.23** that as the concentration decreased the absorption at the rotational transition wavelengths also decreased, as expected. However, the losses experienced by the longitudinal modes within the grating bandwidth are amplified. As discussed earlier, both the 10 ppmv and 100 ppmv C_2H_2 plots were obtained by subtraction from the averaged N_2 background scans collected before and after scanning the sample. It was found that a minimum of 1 ppmv of C_2H_2 could be detected using the HC-PCF based gas cell. Noise fluctuations in the ASE intensity made the detection of 500 ppbv of C_2H_2 inconsistent, which could be resolved by using an active stabilization scheme.
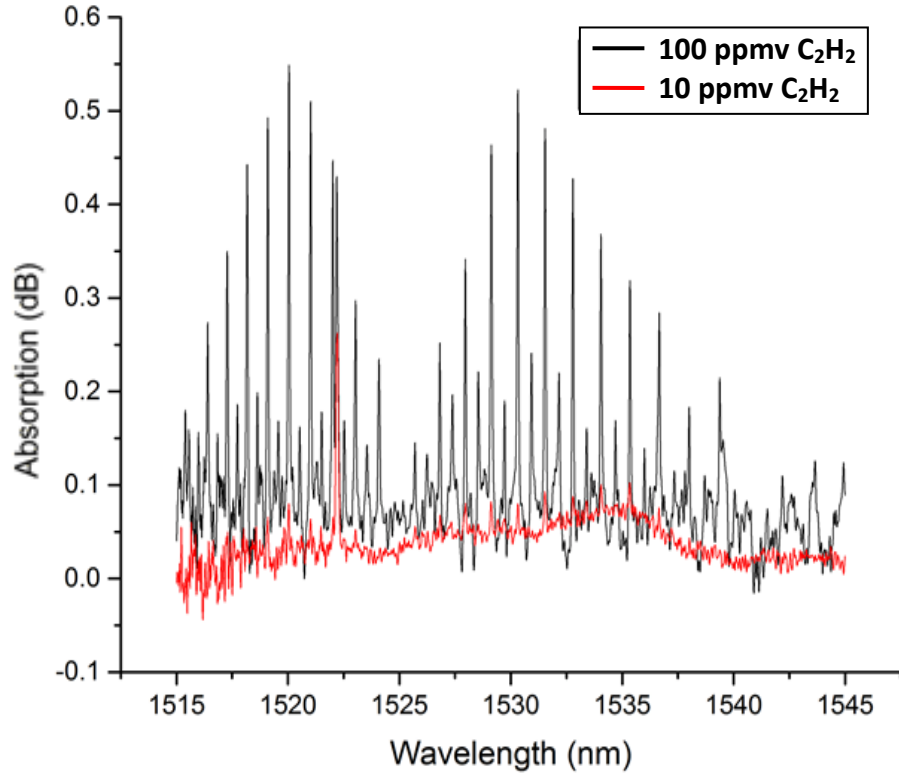
Figure 2.22: Overlay comparison between 10 ppmv and 100 ppmv C_2H_2 samples (after background subtraction) in the gas cell based on HC-PCF.
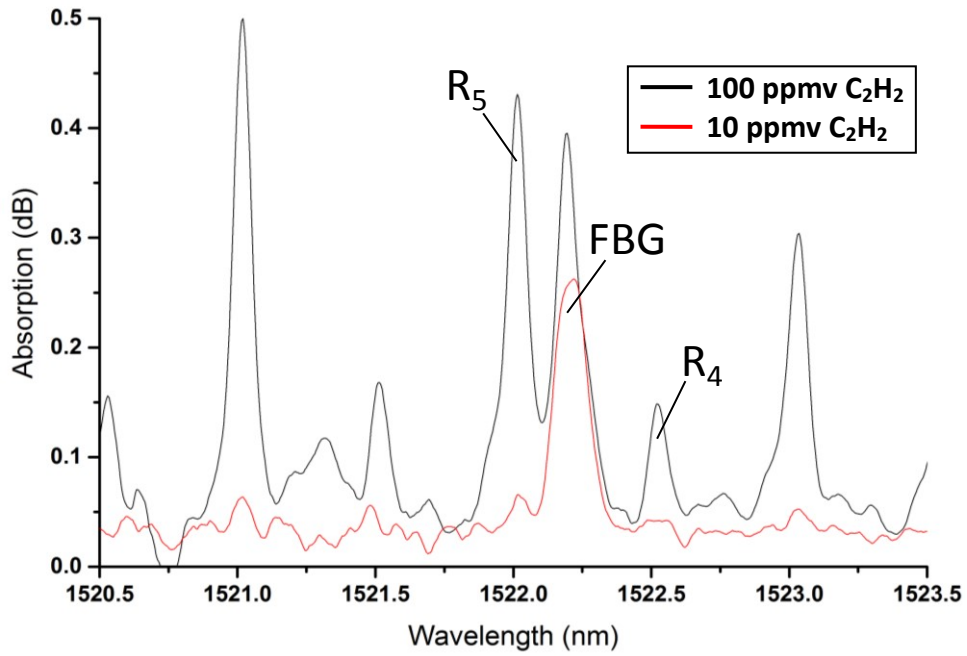
Figure 2.23: Expanded view of the FBG wavelength and R (5) and R (4) rotational transitions in **Figure 2.22**.

The experiment was repeated with the Herriott gas cell which had a coupling efficiency of ~27%. The Herriott cell could be evacuated and filled fairly quickly, since it was a bulk system. Filling was done by evacuating the cell at a rate of 0.5 L/min from one side while allowing the gas to fill from the other. The entire process took ~15 minutes, with 10 minutes for evacuating/filling and 5 minutes for the system to stabilize. Since the inlets were much larger than the HC-PCF core, the cell could be completely flushed with N_2 in minutes.

Figure 2.24 shows the output spectrum obtained from the ICAS system using the Herriott cell filled with a 500 ppbv C_2H_2 gas sample, as well as the N_2 spectra before and after scanning with the sample. **Figure 2.25** shows spectra for C_2H_2 at three different concentrations after the subtraction of the nitrogen spectra. Once again, as the concentration decreases the absorption by the rotational lines is greatly reduced. However, the loss at the FBG wavelength as a result of the absorption of the overlapping R (5) and R (4) absorption lines is still apparent. The minimum concentration detected was 500 ppbv. Lower concentrations were not tested due to the unavailability of C_2H_2 at concentrations below 500 ppbv. However, it is apparent from the noise fluctuations of the system with the Herriott cell, ~0.06 dB, as shown in **Figure 2.26,** and the change in intensity due to absorption of 500 ppbv C_2H_2, ~0.3 dB, (**Figure 2.25**), that concentrations below 500 ppbv should be detectable.

It was found that the Herriott cell produced an interference pattern which was caused by the reflection between the quartz window at the input and the fiber connector. The interference pattern reduced mode-hopping which in turn improved the system stability and reduced background noise in the measurements. A comparison between background fluctuations for the HC-PCF cell and the Herriott cell can be seen in **Figure 2.26**. It is

evident from this figure that the noise level of the HC-PCF cell was more than twice that of the Herriott cell.
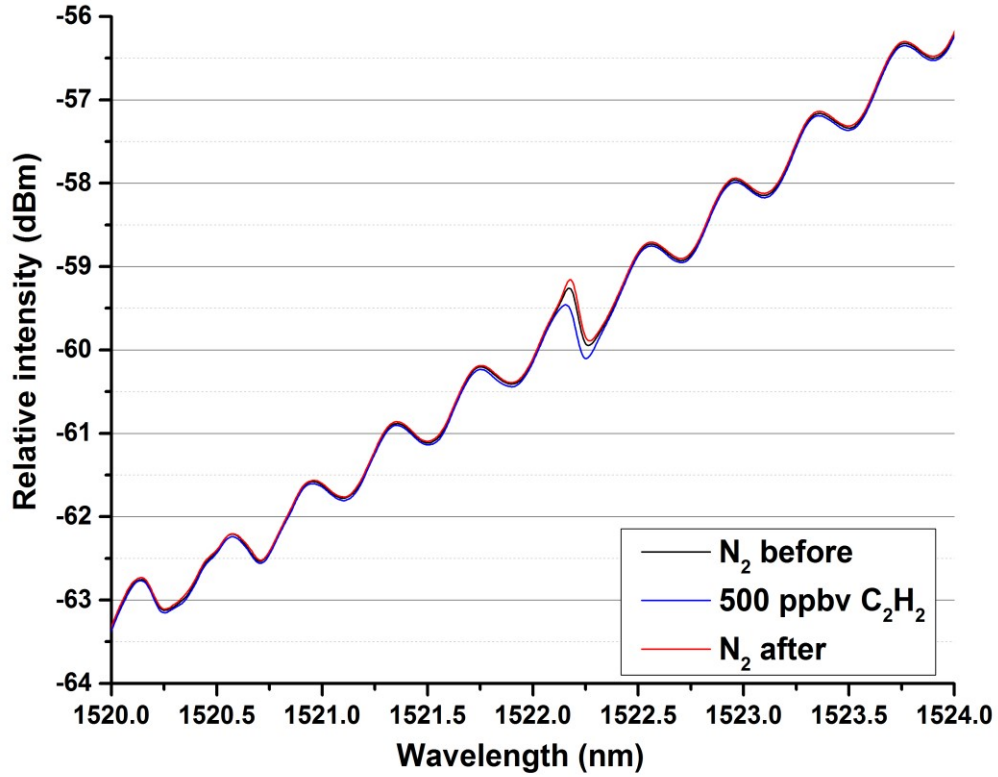
Figure 2.24: Experimental results from 10 scans averaged of 500 ppbv of C_2H_2 compared with 10 scans averaged immediately before and 10 scans averaged after with N_2 in the Herriott cell.
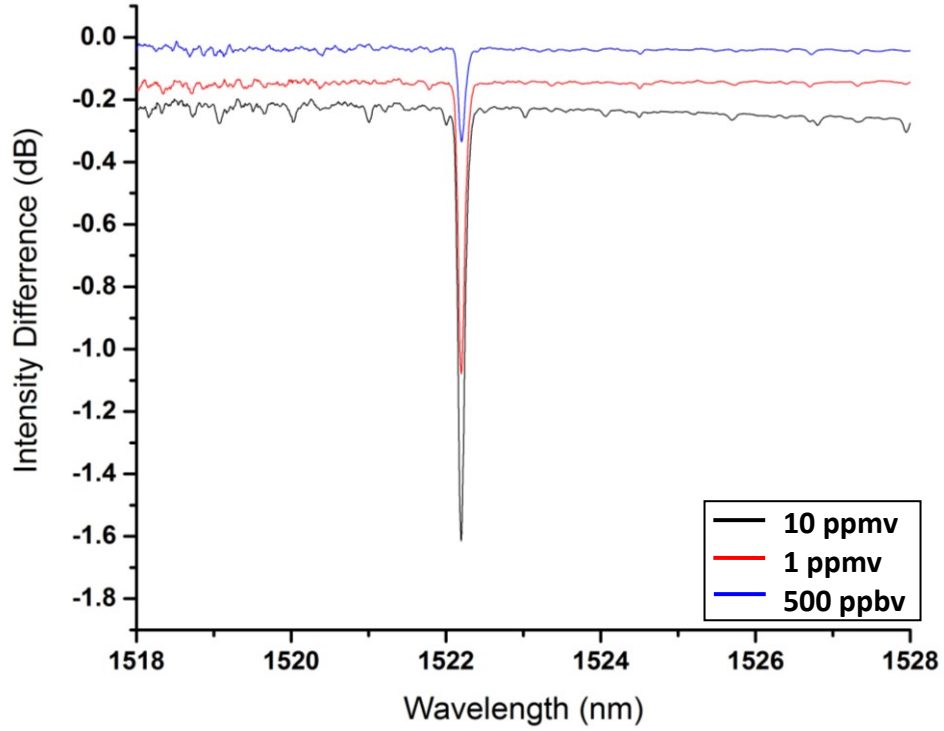
Figure 2.25: Comparison between 3 different C_2H_2 concentrations; 500 ppbv, 1 ppmv, and 10 ppmv after subtraction from their respective N_2 background average scan.
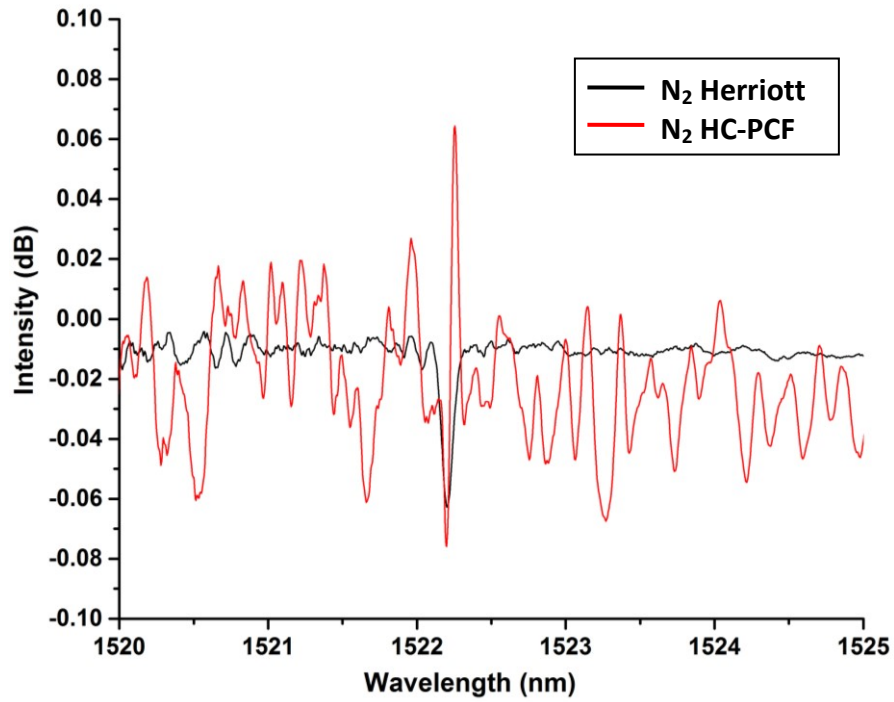
Figure 2.26: Comparison between the noise fluctuations for the Herriott cell (BLACK) and the HC-PCF cell (RED). Each plot is the difference between the two sets of 10 averaged nitrogen scans.

66

2.6 CONCLUSION

The results demonstrated that sub-ppmv concentrations of acetylene could be detected using the developed ICAS system. Inclusion of the saturable absorber with the FBG greatly reduced mode-hopping and improved the overall stability of the system. As well, the use of the FBG showed promising results for the detection of rotational lines which do not correspond to the peak FBG reflection wavelength, one of the unique aspects of the system. This demonstrates that the technique can be applied to different absorbing samples which do not directly coincide with the FBG. Further, this detection system has the advantages of ambient temperature operation and the use of low cost optical components. The application of this technique with absorption lines of nitrous oxide (N_2O) that closely match with the FBG central wavelength will be discussed in Chapters 3 and 4.

Chapter 3

Detection of nitrous oxide (N$_2$O) at sub-ppmv level using an ICAS system

In this chapter, the detection of nitrous oxide (N$_2$O) at sub-ppmv concentrations is reported. This is demonstrated by using the ICAS system with an intracavity multi-pass Herriott cell as demonstrated in Chapter 2. The system was designed for the detection of the P (12) rotational line of N$_2$O gas at ~1522.20 nm. A fiber Bragg grating (FBG) with a wavelength which corresponded with the absorption line was used to enhance the sensitivity of the system.

3.1 INTRODUCTION

N$_2$O is a greenhouse gas (GHG) with an increasing atmospheric concentration due to human activity. As of 2013, the concentration of nitrous oxide in the atmosphere was ~324 ppbv (parts per billion by volume) and is becoming more abundant due to the increased use of nitrogen based fertilizers [77-79]. Since N$_2$O absorbs ~300 times more infrared (IR) radiation than carbon dioxide (CO$_2$), it contributes considerably to the greenhouse effect. The increasing presence of nitrous oxide, and the need for active monitoring was the main motivation for this research. Current greenhouse gas monitoring technology used to quantify the N$_2$O concentrations are typically complex and expensive to deploy in field, specifically in

agriculture settings. In most cases, it involves collecting emitted gases for analysis using gas chromatography (GC) or Fourier Transform Infrared Spectroscopy (FTIR) in a laboratory, or using expensive laser spectroscopy methods such as cryo-cooled Pb-salt tunable diode laser spectroscopy [2]. There is a demand for a compact and cost effective system, which can provide a high sensitivity and real-time analysis of the emitted gases in an agriculture field.

3.2 NITROUS OXIDE (N_2O) GAS

N_2O is a non-toxic, colorless gas with a linear asymmetric structure. N_2O has three fundamental vibrational modes: a symmetric stretching mode at $\nu_1 = 1285$ cm^{-1} = ~ 7.8 μm, a doubly degenerate bending mode at $\nu_2 = 589$ cm^{-1} = ~ 17 μm, and an asymmetric stretching mode at $\nu_3 = 2224$ cm^{-1} = ~ 4.5 μm [65], as shown in **Figure 3.1**. The gas has overtones and combinations of overtones of the fundamental vibrational transitions in the near-infrared (NIR) region (1 - 2 μm). Many of these transitions have been identified using various techniques, such as FTIR [80-85], cavity ring down spectroscopy [86-88] and intracavity laser absorption spectroscopy [89].
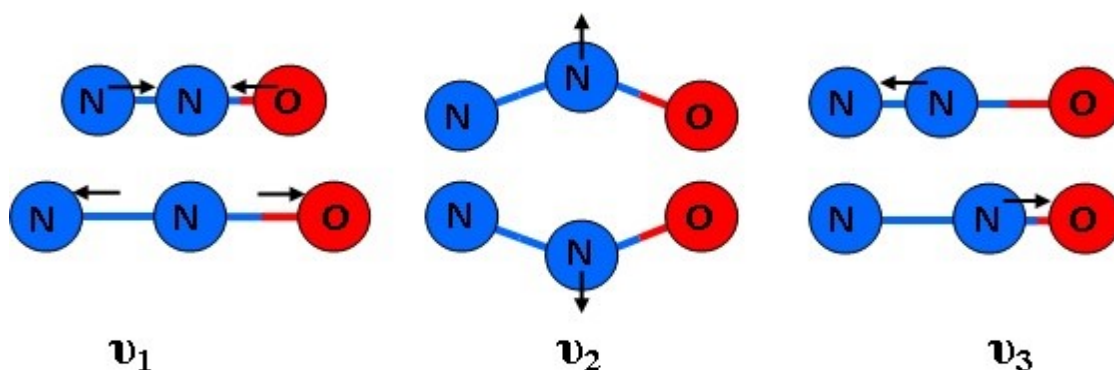
Figure 3.1: Depiction of the 3 fundamental vibrational modes of nitrous oxide; $\upsilon_1 = 1285$ cm^{-1} (symmetric stretching), $\upsilon_2 = 589$ cm^{-1} (doubly degenerate bending), and $\upsilon_3 = 2224$ cm^{-1} (asymmetric stretching).

N_2O has absorption bands in the NIR region, which coincide with the amplified

spontaneous emission (ASE) spectrum (1.5 to 1.6 μm) of erbium-doped fiber. Many compact and inexpensive optical components have been developed for the erbium emission band by the telecom industry, which can be used to develop a real-time N_2O sensor operating at ambient temperature. Furthermore, a system designed using fiber technology would be able to incorporate multiple N_2O sensors through fiber optic networking [90].

The system presented was developed to detect an absorption line in the P-branch of the $3\upsilon_3$ vibrational band of N_2O [41], more specifically the P(12) rotational line at ~1522.20 nm which has a relatively high absorption coefficient (**Figure 3.2**). Further, the absorption from other abundant atmospheric components (e.g., water vapor and carbon dioxide) is comparatively very weak, as is shown in **Figure 3.3**.
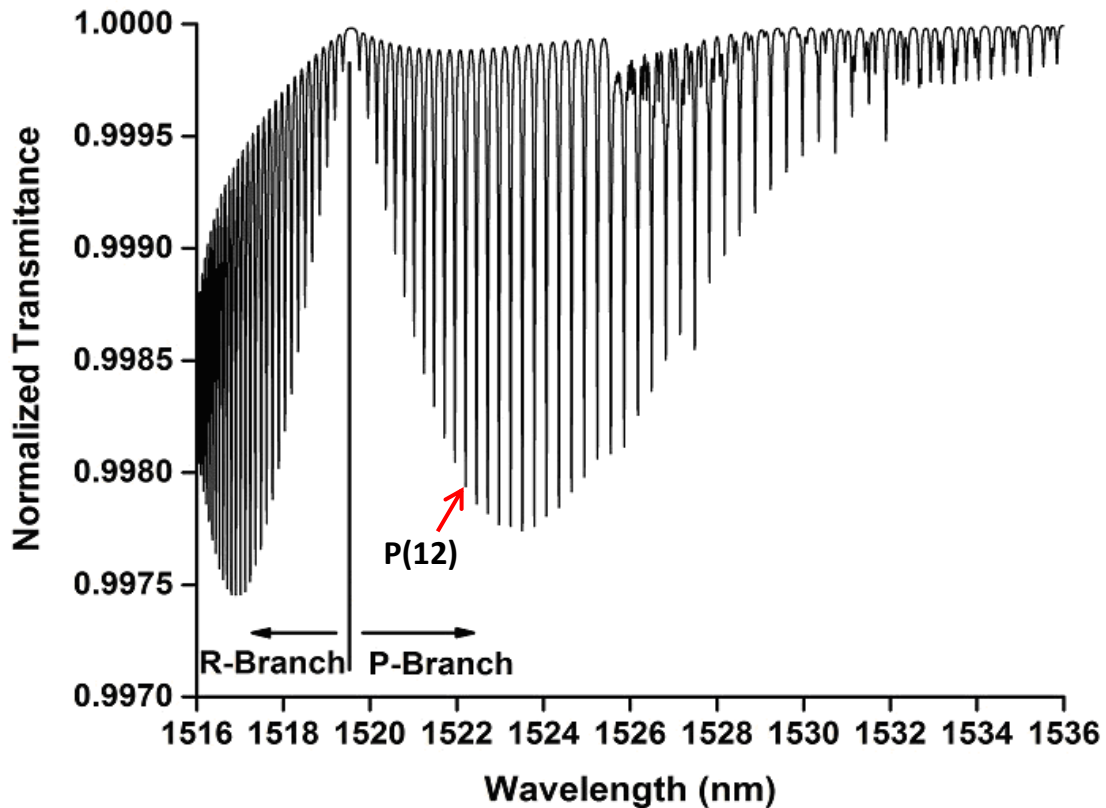
Figure 3.2: Theoretical rotational transitions for N_2O in the $3\upsilon_3$ vibrational band obtained using HITRAN [41].
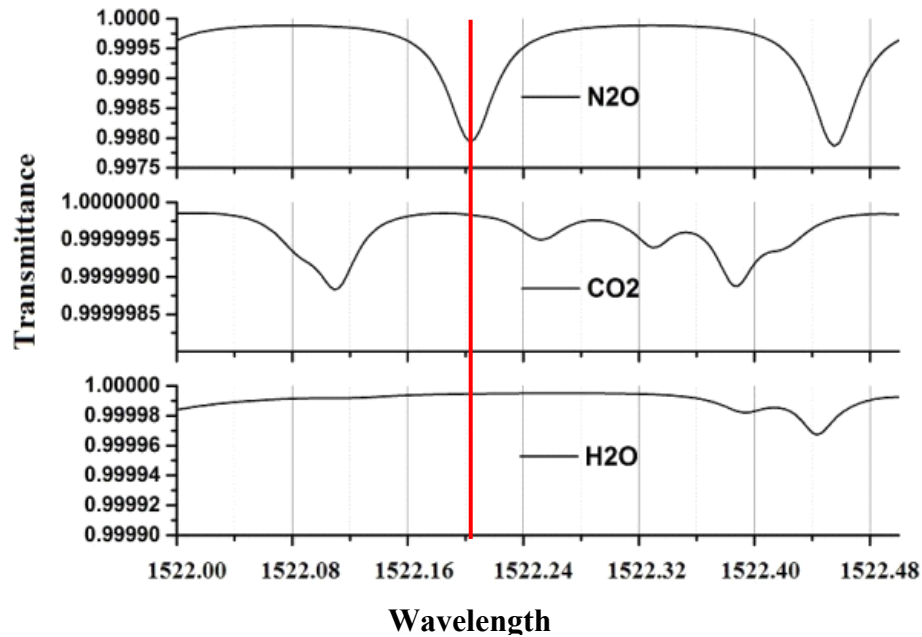
Figure 3.3: Comparison of nitrous oxide (N_2O), carbon dioxide (CO_2) and water (H_2O) transmission in the region of the P(12) rotational line in the $3\upsilon_3$ band of N_2O. The P (12) rotational line is identified with the red line.

At the P(12) wavelength, the absorption coefficient of N_2O is ~150 times greater than H_2O and more than 10000 times greater than CO_2 **(Table 3.1)**. However, the average atmospheric concentration of CO_2 is ~ 395 ppmv which implies there will be a marginal absorption due to carbon dioxide at the P (12) wavelength that needs to be accounted for [91].

Table 3.1: Comparison between of common absorbing atmospheric gases at 1522.2 nm

Molecule	Approx. atmospheric concentration (ppmv)	Absorption coefficient (cm^{-1})	Ratio of N_2O absorption to other molecules
Nitrous Oxide (N_2O)	0.324	1.62025×10^{-3}	1
Carbon Dioxide (CO_2)	395	1.57598×10^{-7}	10281
Water (H_2O)	Varies	1.05197×10^{-5}	154

3.3 RESULTS AND DISCUSSION

An ICAS system based on the ring cavity fiber laser configuration (**Figure 2.18**) and using the ASE present inside the laser cavity was developed as described in Chapter 2. A Herriott gas cell with 30 m effective path length was used. The laser was operated near the threshold condition, which was one of the requirements for the developed method as described in Chapter 2.

The gas cell was flushed with N_2 before and after each N_2O gas concentration was tested. The data collection was started two hours after turning on all of the equipment (e.g. laser, optical spectrum analyzer, and power meter), which reduced possible fluctuations of the laser wavelength due to temperature variation [92]. The Herriott cell was filled at atmospheric pressure by evacuating from one end and allowing the N_2O gas sample in the 10 L Tedlar bag to diffuse in from the other end of the fiber. The evacuation rate, and consequentially fill rate, was maintained at 0.5 L/min. for 10 minutes (i.e. for 5 L of sample). After filling the cell with nitrogen gas and collecting the background spectra, the cell was filled with the N_2O sample and the output spectra were collected. Depending on the spectrum range of the collected data, it could take between 30 - 45 minutes to fill the gas cell and collect a data set for each gas. N_2 and N_2O gas samples were alternated to prevent residual concentrations from influencing one another. In general, the N_2O samples were tested in order of increasing concentrations. It is to be noted however, that experiments were performed with N_2O sample concentrations in an arbitrary order, and experiments were also performed without flushing the cell with N_2 in between analytes. These experimental variations were performed to verify that the results were not attributed some systematic effect.

Figure 3.4 shows a comparison between the theoretical absorption lines of a 2% N_2O gas

with the ASE spectrum of the fiber cavity. It is evident from **Figure 3.4** that N_2O possesses

relatively strong absorption features near 1522 nm. However, the drawback of detecting

absorption at this position is that it does not correspond with the natural flat regions of the

erbium-doped fiber ASE spectrum or high gain regions (C and L bands) of the erbium-doped

fiber ASE spectrum. The ASE in the 1522 nm region has a relatively low intensity.
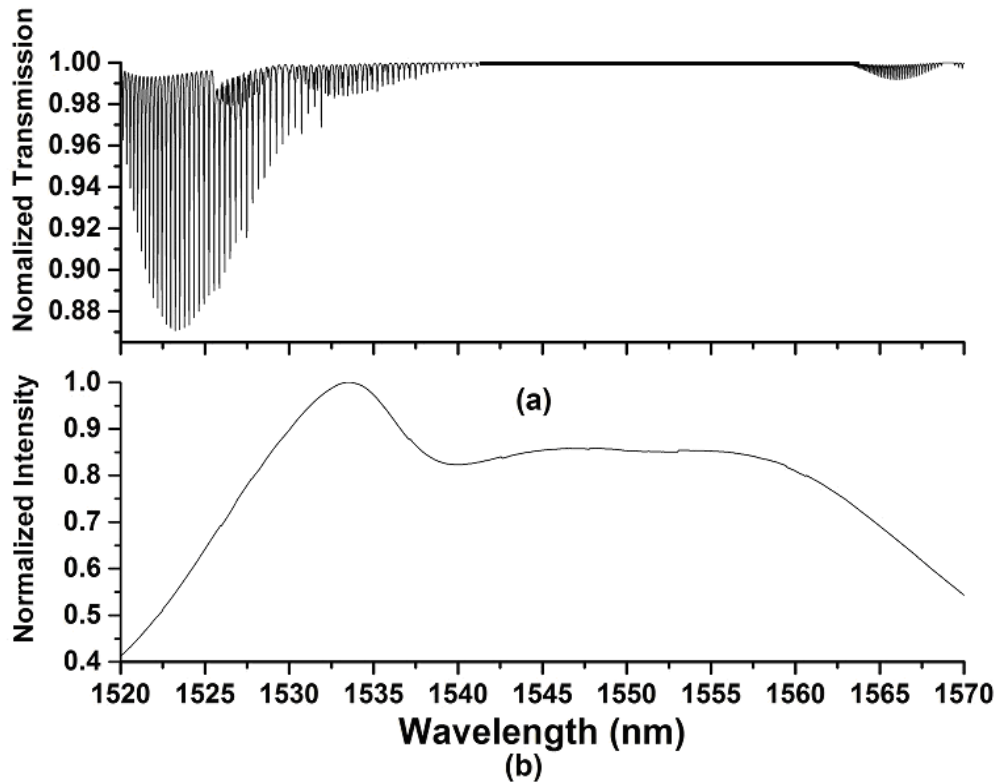
Figure 3.4: (a) Theoretical absorption lines for 2% N_2O and a path length of 30 m obtained using GATS Spectral Calculator (HITRAN 2012); **(b)** ASE spectrum from the PM-EDF used as the gain medium at a 50 mA pump current.

The experiments were performed using the ICAS technique, where the cavity was

operated at the threshold condition. The Herriott cell was incorporated into the simple ring

resonator configuration without the FBG section, as shown in **Figure 2.15** of Chapter 2. In

order to determine the minimum detection limit of this simple ICAS system various

concentrations of N_2O where analyzed, ranging from 0.5% to 10% N_2O. The 10% N_2O gas

73

was a standard concentration provided by Praxair, Canada. The output of the system was monitored using an ANDO AQ6317B optical spectrum analyzer. As previously mentioned in Chapter 2, an interference pattern was visible in the transmission spectrum, which was due to the etalon effect between the connector and quartz windows in the Herriott gas cell. The interference effect greatly improved the cavity stability by reducing mode hopping. **Figure 3.5** shows the interference pattern in the output spectrum of the laser cavity with N_2 gas in the cell. The interference pattern disappeared after subtraction between the N_2 and N_2O spectra was done and the absorption or transmission spectrum recovered.
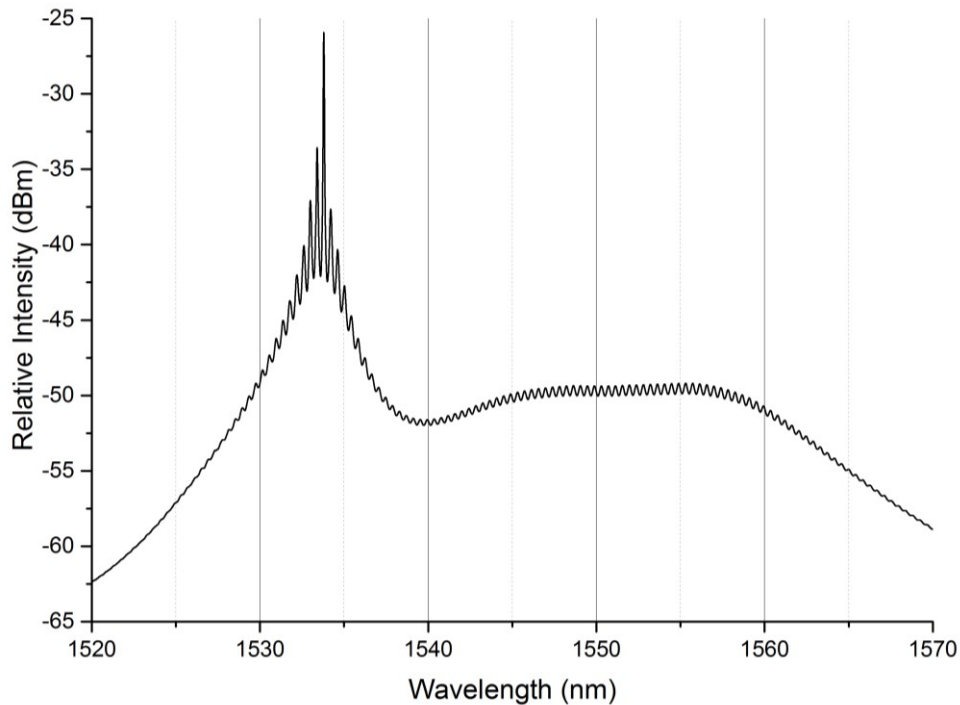
Figure 3.5: Output spectrum from the laser cavity exhibiting the interference pattern from etalon effect at Herriott cell quartz window, with N_2 gas present in the cell.

Using this simple ICAS system the minimum N_2O concentration that could be consistently detected was 2%. **Figure 3.6** shows the transmission spectra obtained from N_2O concentrations of 2%, 5%, and 10%. Further, **Figure 3.7** shows the transmission spectra for N_2 gas and the N_2O gas concentrations of 2%, 4%, 6%, and 8%.
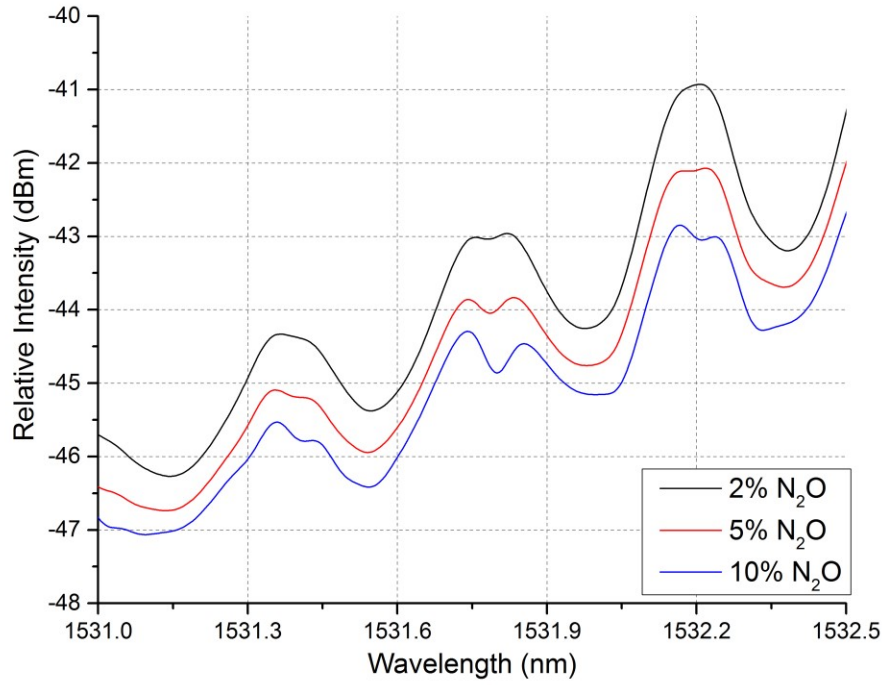
Figure 3.6: Comparison between the spectra for 2%, 5%, and 10% concentrations of N_2O in the ICAS cavity configuration.
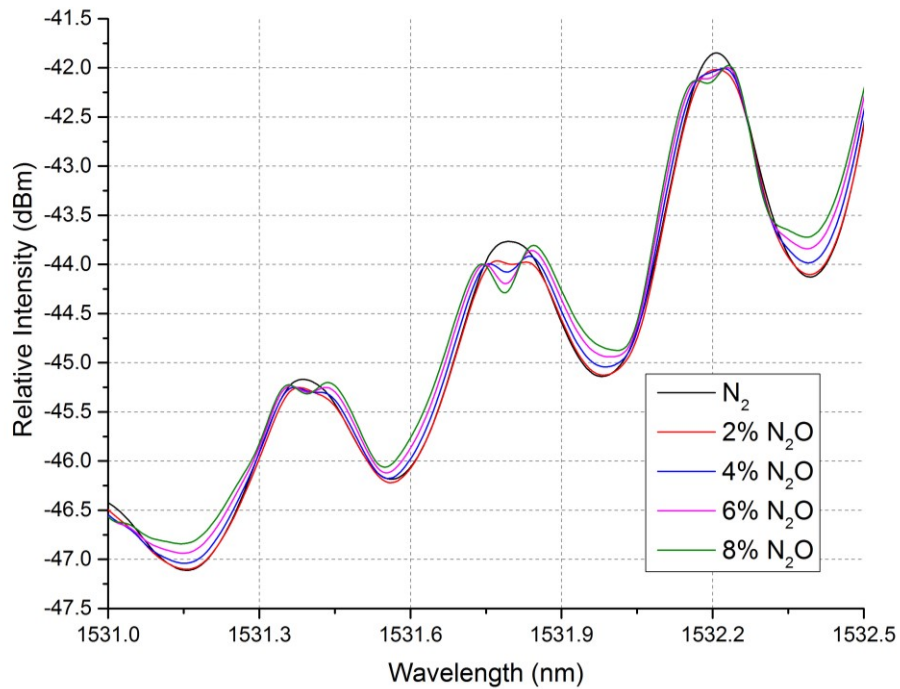
Figure 3.7: Comparison between the nonabsorbent N_2 background gas and 2%, 4%, 6%, and 8% concentrations of N_2O.

The data in **Figure 3.6** and **Figure 3.7** was collected on different days and could not be directly compared as threshold conditions, as well as the operating conditions of other system components, are influenced by the environmental conditions such as temperature [92]. A comparison between the theoretical N_2O absorption spectrum and the experimentally obtained absorption spectra for 2% and 8% N_2O concentrations is shown in **Figure 3.8**. The experimental transmission spectra were recovered by subtracting the N_2O spectra from the N_2 spectra.
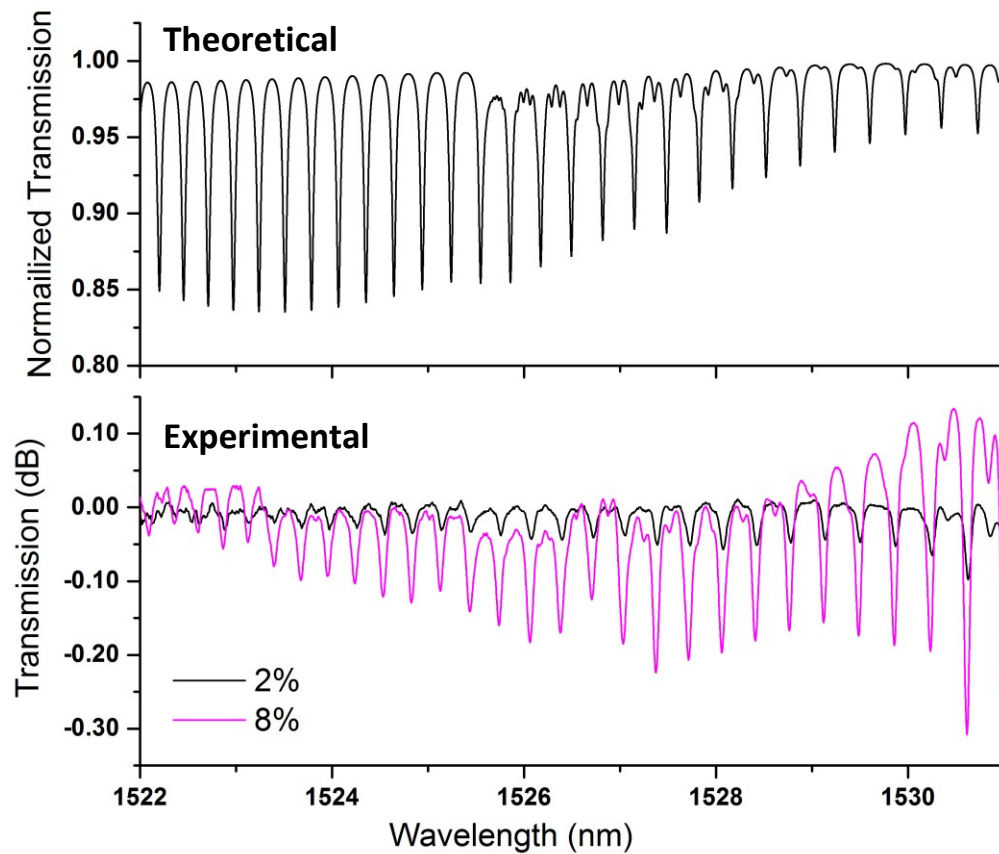
Figure 3.8: Theoretical transmission compared with the experimental transmission for 2% and 8% N_2O concentrations after subtraction from N_2 gas.

In order to improve the systems sensitivity the fiber Bragg grating (FBG) was included in the cavity, as described in **Figure 2.18** in Chapter 2. The FBG peak wavelength was selected

in the 1522 nm band to take advantage of the high absorption coefficient of N_2O in this region. The laser was operated near threshold, so that a number of longitudinal modes within the grating bandwidth were competing. This resulted in nearly equal longitudinal mode intensities in the small portion of the ASE spectrum at 1522.20 nm wavelength. At threshold any loss experienced by the modes within the grating bandwidth results in an exponential decay. Since the system is being operated at threshold, any change in the intensity of the modes is strictly related to sample absorption. This technique is a modification of the method presented by Arsad et al. [46], which used the ASE at threshold conditions for the detection of gas. However, the method presented by Arsad et al. relied on the absorption lines occurring at specific regions (C or L band) of the erbium ASE spectrum. Including a FBG into the cavity allows for the selection of strong absorption lines outside of the C and L band regions and improved detection sensitivity.

The purpose of this experiment was to probe the sensitivity of the system for an absorption feature which falls within the FBG bandwidth (**Figure 3.9**). In this experiment the P (12) rotational line of the $3v_3$ absorption band of N_2O was analyzed. This specific absorption line has a relatively high absorption at a position that corresponds with the resonant modes of the cavity as chosen by the FBG.
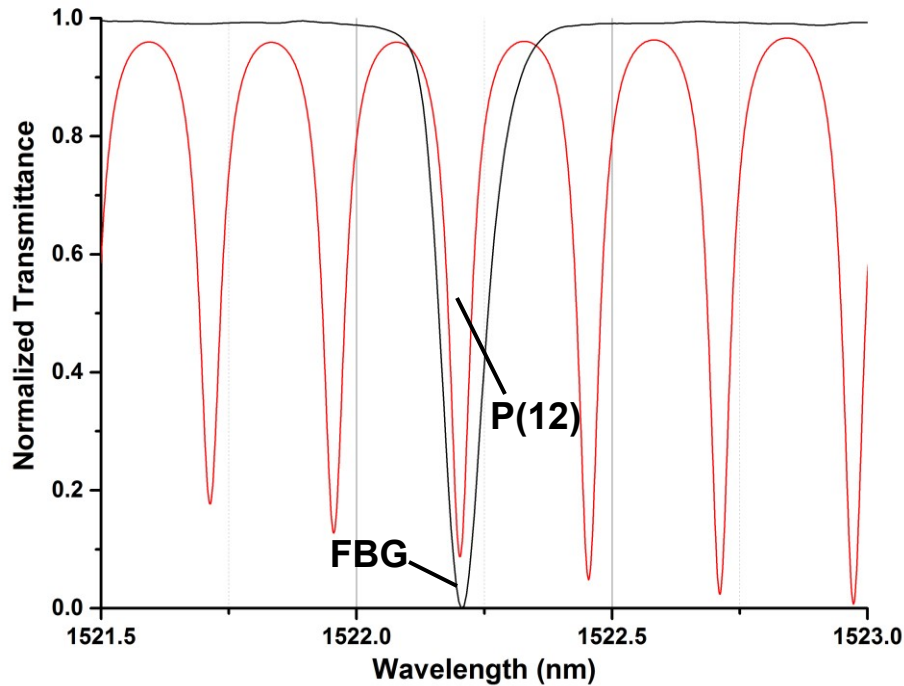
Figure 3.9: Comparison of the theoretical N_2O absorption spectrum for the $3v_3$ band (RED) with the cavity output spectrum with the FBG (BLACK) to demonstrate the overlap of the P(12) rotational absorption line with the fiber Bragg grating.

Figure 2.18 shows the system configuration, which includes the saturable absorber in combination with the FBG to improve system stability, and an optical isolator to prevent back scattering. This configuration allowed the radiation within the FBG reflection bandwidth to make multiple roundtrips in the cavity, enhancing the effective path length.

In order to take advantage of the improved sensitivity the laser was operated at threshold condition, such that the ASE spectrum across the FBG bandwidth was nearly flat in respect to the longitudinal mode intensity. After warming up the system, the Herriott cell was filled with N_2. The system output was set to the threshold position by adjusting the pump current and the variable optical attenuator. For measurements of very low concentrations the polarization controller (PC) plates were finely adjusted to obtain a highly stable output. When the system reached the optimum stability the ASE modes within the FBG became very

sensitive to the changes attributed to N_2O absorption. After the initial adjustments were made to achieve the threshold condition no more alterations were made to the pump current, VOA, or polarization controller for the duration of the experiment. **Figure 3.10** demonstrates the stability that could be achieved with the system and is the difference between averages of two N_2 spectra sets collected ~2 hours apart with N_2O samples tested in between.
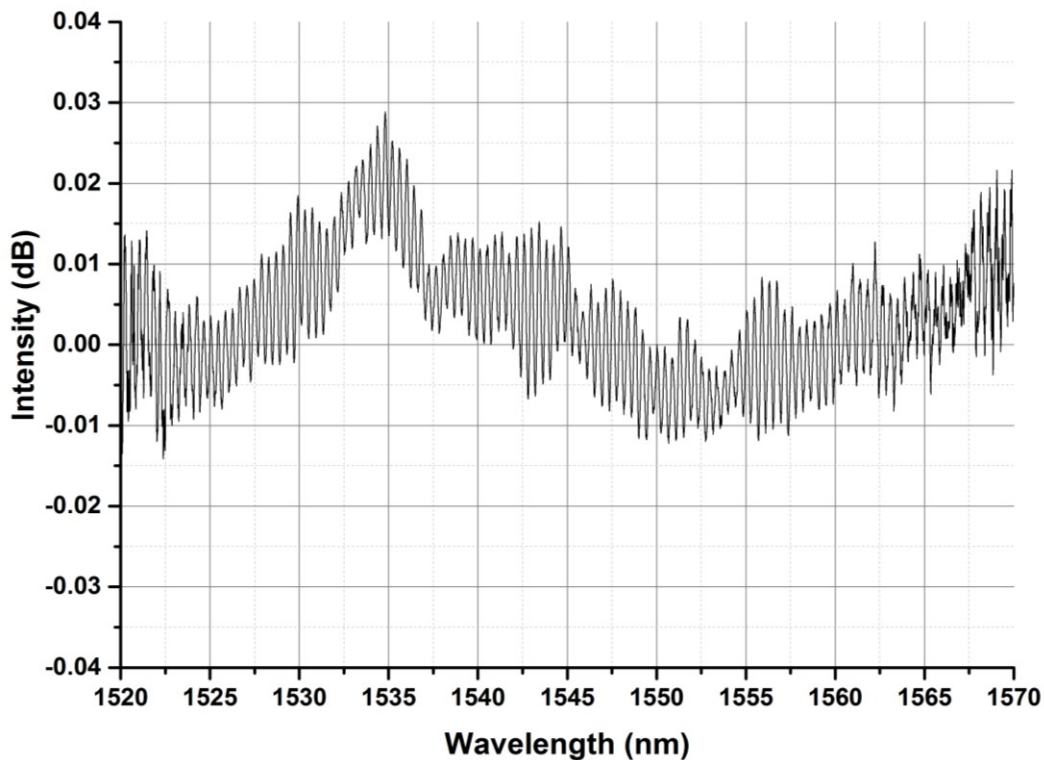
Figure 3.10: System stability obtained from the difference between averaged N_2 spectra sets collected ~ 2 hours apart.

The Herriott cell was flushed and filled with N_2 before and after each N_2O sample at different concentration, so that background spectra could be collected. Collecting N_2 spectra between each analyte sample provided the added benefits of being able to monitor the stability of the system, as well as indicating whether any residual N_2O gas was still present.

The majority of the systems instability was due to sudden changes in environmental conditions (e.g., temperature). If there was an abrupt and substantial fluctuation in temperature, typically more than $2^{\circ}C$, the grating wavelength would shift due to the temperature dependence of the FBG, and alter the resonant condition of the cavity. However, these fluctuations could be addressed by maintaining the FBG at a fixed temperature or through an active stabilization scheme [93].

The total length of the laser cavity was approximately 50 m, this corresponds to a longitudinal mode spacing of ~ 4 MHz. Since the longitudinal-mode spacing is quite close, thousands of modes are supported in the FBG bandwidth. **Figure 3.11** shows the theoretical N_2O absorption lines compared with the actual laser output spectrum of the FBG above and at threshold.
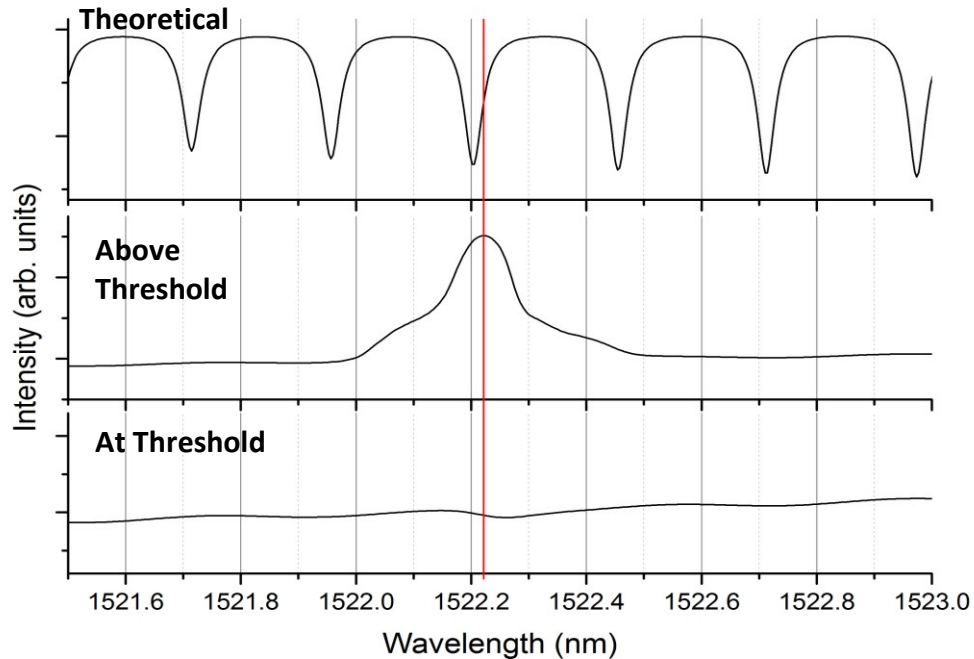
Figure 3.11: Comparison between the theoretical P (12) absorption line and the FBG above the lasing threshold and at the lasing threshold. The Bragg wavelength is identified by the RED line.

As the erbium-doped fiber is a homogeneous gain medium at room temperature, any small loss in a cavity mode will change the cavity resonance condition. It has been demonstrated by Baev et al. [48] that a multimode laser with a homogeneously broadened gain medium offers a very high sensitivity due to absorption by the longitudinal modes. Thus, the system sensitivity was enhanced by the multiple roundtrips the light would make inside the cavity, as well as the multi-longitudinal modes which coincide with the P (12) absorption line [94].

N_2O spectra for various concentrations are displayed in **Figure 3.12**, for high concentrations the absorption effect appeared to become saturated. **Figure 3.13** shows the transmission spectra of the N_2 reference gas, and 10 ppmv N_2O gas at the FBG wavelength. The transmission spectra for the different N_2 scans are given as N_2^{Before} and N_2^{After}. The various concentrations were derived from the certified concentrations of 1 ppm, 10 ppm, and 1001 ppm following the method described in **Appendix A**.
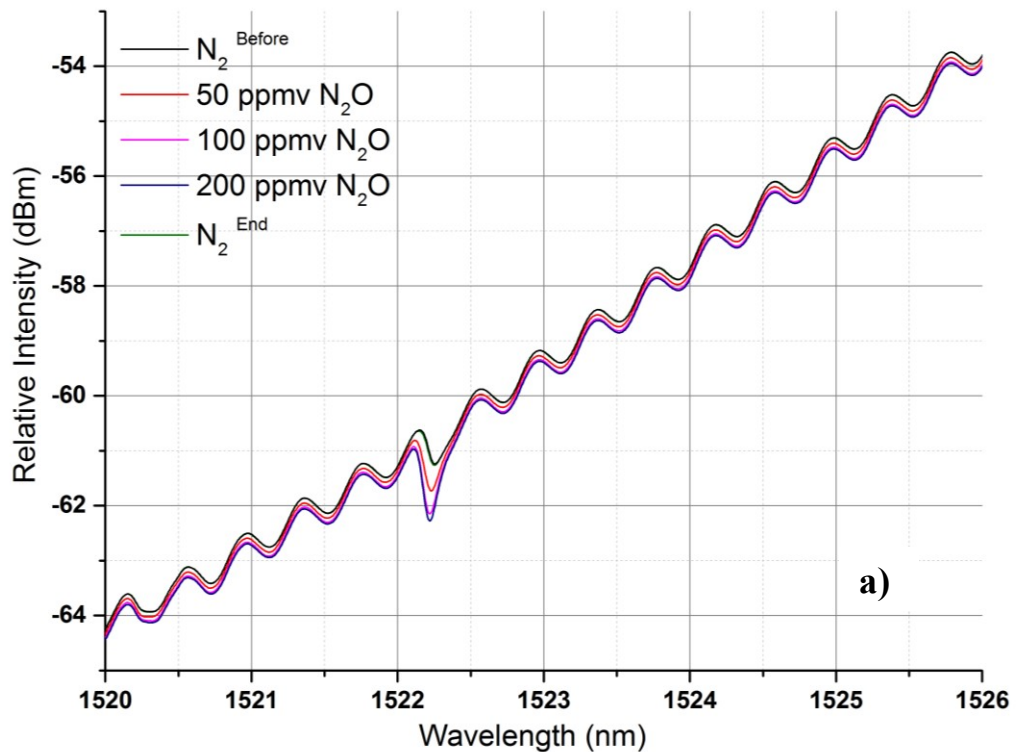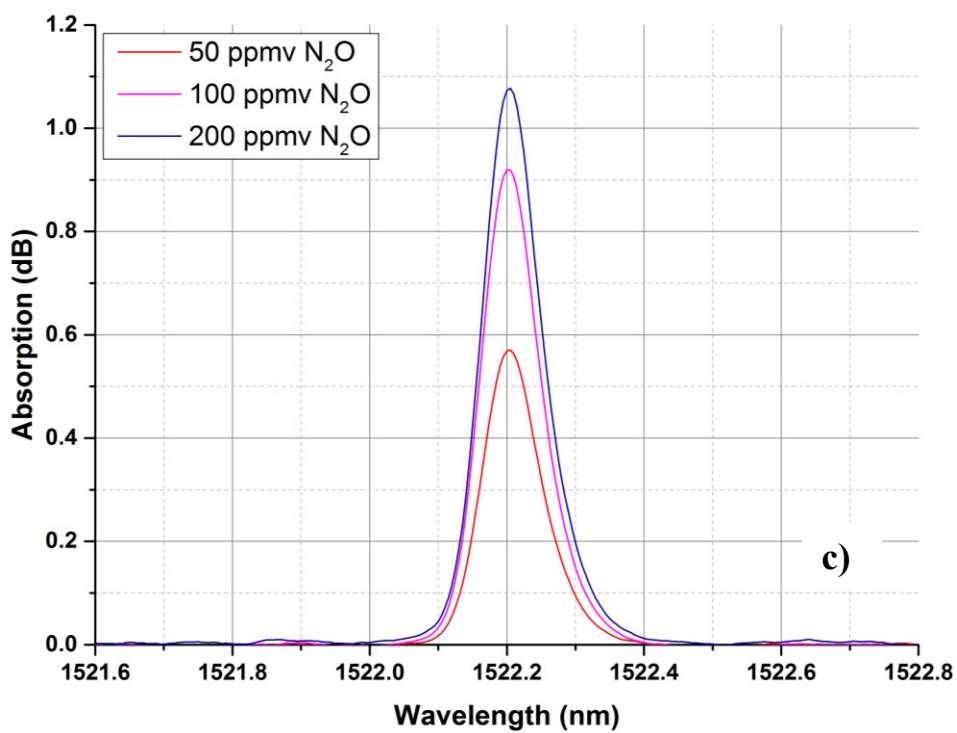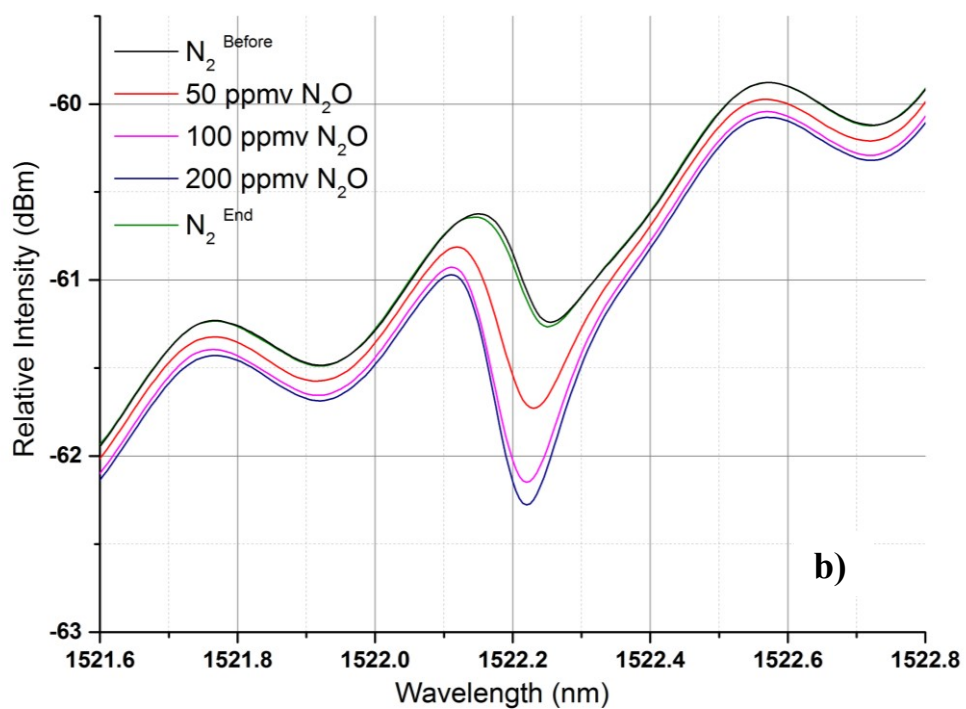
Figure 3.12: (a) Spectra for N_2 gas samples before and after the 50 ppmv, 100 ppmv, and 200 ppmv of N_2O samples; **(b)** is a zoomed in view of the same raw spectra; and **(c)** is absorption spectra for each of the N_2O concentrations after subtraction from the averaged (before and after) N_2 data.
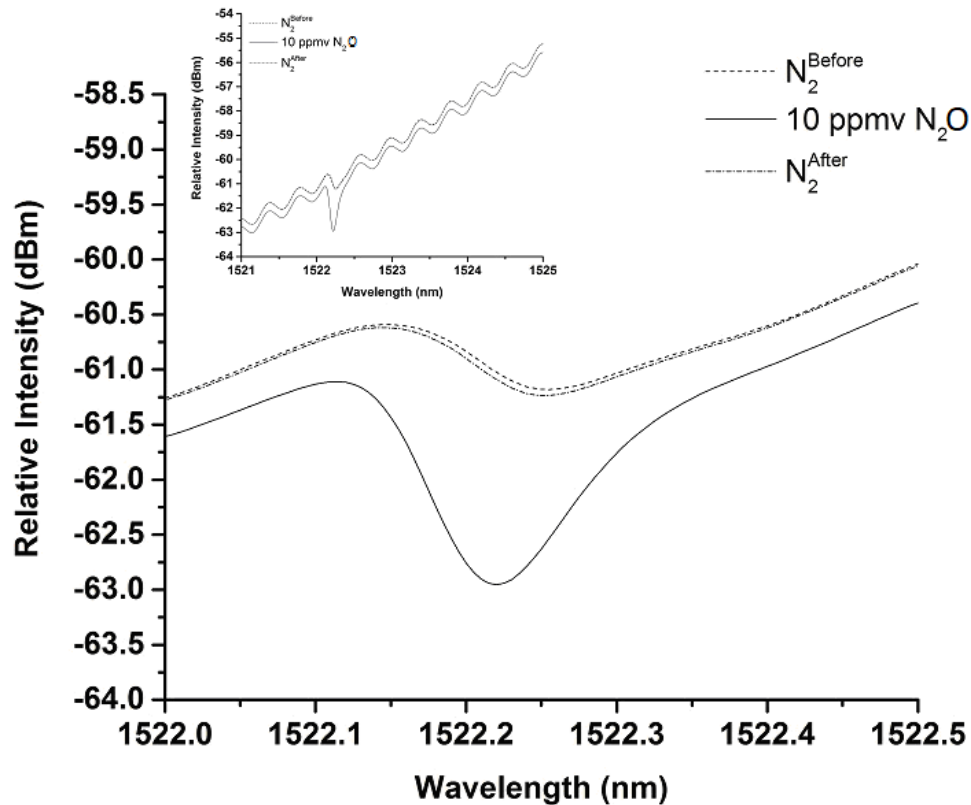
Figure 3.13: Transmission spectra of the ASE at the FBG wavelength with reference gas N_2, before and after, with 10 ppmv of N_2O. The inset of the figure is an expanded view of the spectrum.

Figure 3.14 shows the transmission spectra of reference gas N_2 and N_2O gas of concentration 100 ppbv. A comparison between the transmission spectrum for 100 ppbv, 500 ppbv, and 1 ppmv N_2O concentrations is shown in **Figure 3.15**. Each transmission spectra was recovered by subtracting the N_2O spectra from the averaged N_2 spectra taken before and after sample. The 100 ppbv gas mixture was prepared from a 10 ppmv standard. To confirm that the N_2O mixtures were close to the desired concentrations they were measured using gas chromatography (GC). The actual gas concentration for 100 ppbv was found to be ~127 ppbv. Attempts were made to mix and test concentrations of 50 ppbv, but such low concentrations could not be produced consistently.
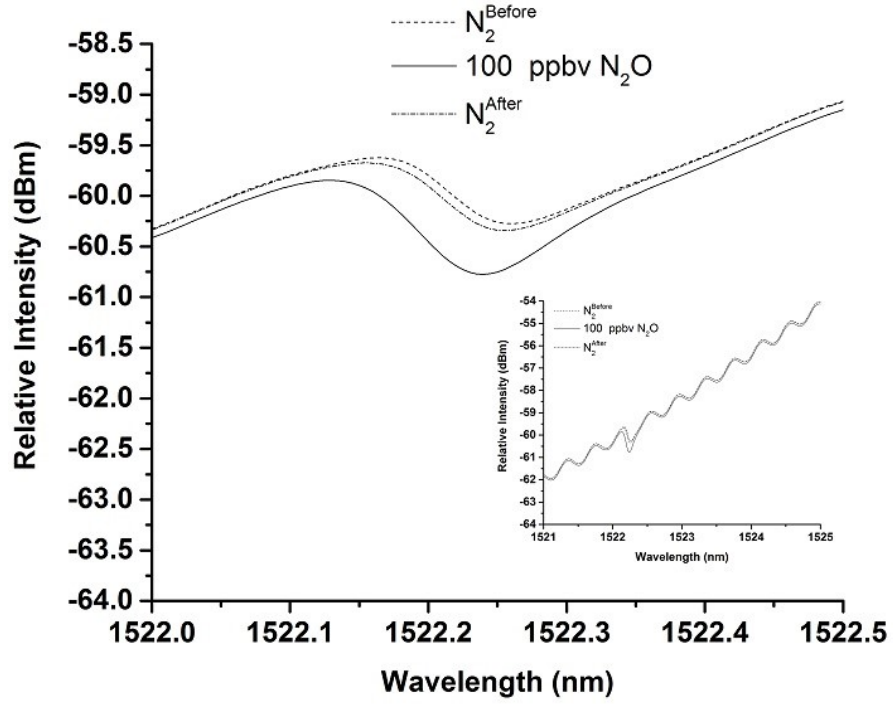
Figure 3.14: Transmission spectra of the ASE at the FBG wavelength with reference gas N_2, before and after, with 100 ppbv of N_2O. The inset of the figure is an expanded view of the spectrum.
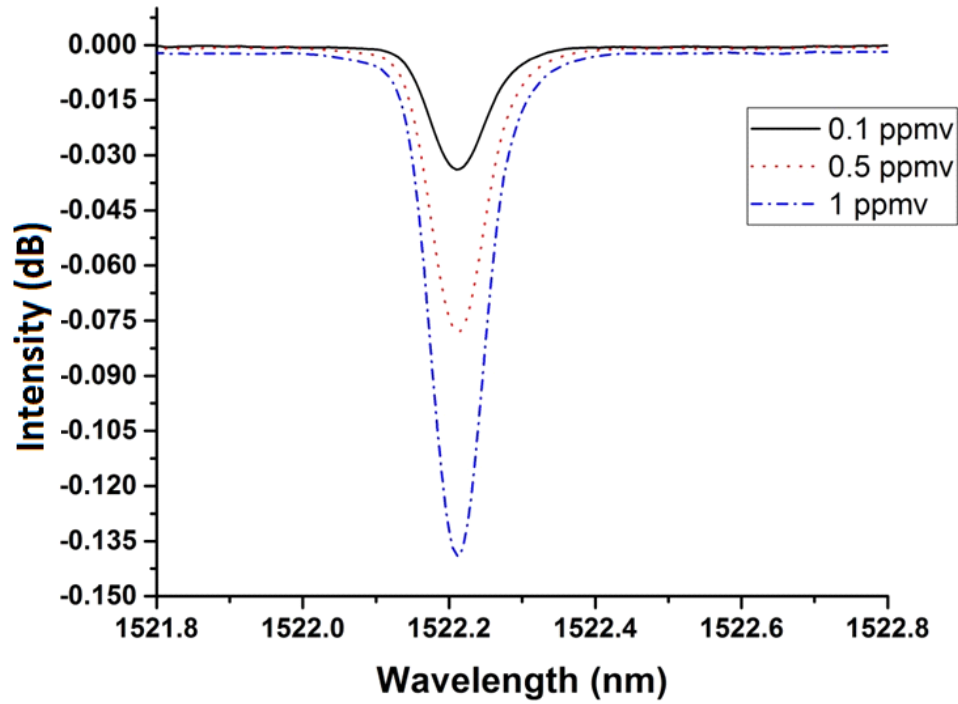
Figure 3.15: Transmission spectra after subtraction from N_2 gas for 0.1 ppmv, 0.5 ppmv, and 1 ppmv concentrations of N_2O.

3.4 CONCLUSION

It was found that this fiber laser system was capable of detecting N_2O concentrations in the ppbv levels. This was accomplished by incorporating a FBG into an ICAS system such that a strong absorption line could be selected for detection. Further, by operating the system at the threshold condition enhanced the effect of the sample absorption. The system demonstrated a very high stability against mode-hopping as a saturable absorber was used, which also improved the minimum detection limit. The Herriott cell had a quick fill time which would make this system appealing for monitoring N_2O emissions from fertilized agriculture fields. It is expected that further work will reduce the minimum detectable concentration to even lower values.

Chapter 4

A hollow-core photonic crystal fiber gas cell used for the detection of nitrous oxide (N$_2$O)

This chapter is focused on the application of a hollow-core photonic crystal fiber (HC-PCF) based gas cell for the detection of nitrous oxide (N$_2$O) gas. The gas cell was tested using the direct absorption spectroscopy (DAS) technique and the intracavity absorption spectroscopy (ICAS) technique. The lengths of hollow-core fiber tested in the gas cell were 20 m and 40 m. The HC-PCF gas cell (**Gas Cell 2**) was incorporated into the ICAS system as described in Section 2.4.2 of Chapter 2. The sensitivity of the system was enhanced when the laser was operated near the threshold, which is one of the requirements for the new ICAS method. The ICAS system based on the new HC-PCF gas cell was capable of detecting N$_2$O gas at sub-ppmv concentration level. The efficiency of the device has been explored with the two different lengths of HC-PCF.

4.1   INTRODUCTION

HC-PCF is very attractive for many applications due to its low attenuation, dispersion, nonlinearity, and bending loss [95-97]. Further, HC-PCF can guide a fundamental mode over a wide spectral range without any leakage [98;99]. Light propagates through the

hollow-core of the fiber by photonic band gap effects, which is due to the periodic distribution of air holes in the cladding [100], as shown in **Figure 4.1**. A gas cell which requires a small amount of gas (~mL) is an important characteristic for an efficient laser absorption spectroscopy system. In this respect, HC-PCF is appealing as a gas cell since it requires a very small sample volume, as well HC-PCF provides highly efficient interaction between the laser and analyte [101-103]. A device based on HC-PCF would not only be compact, but also cost effective [18;104;105].
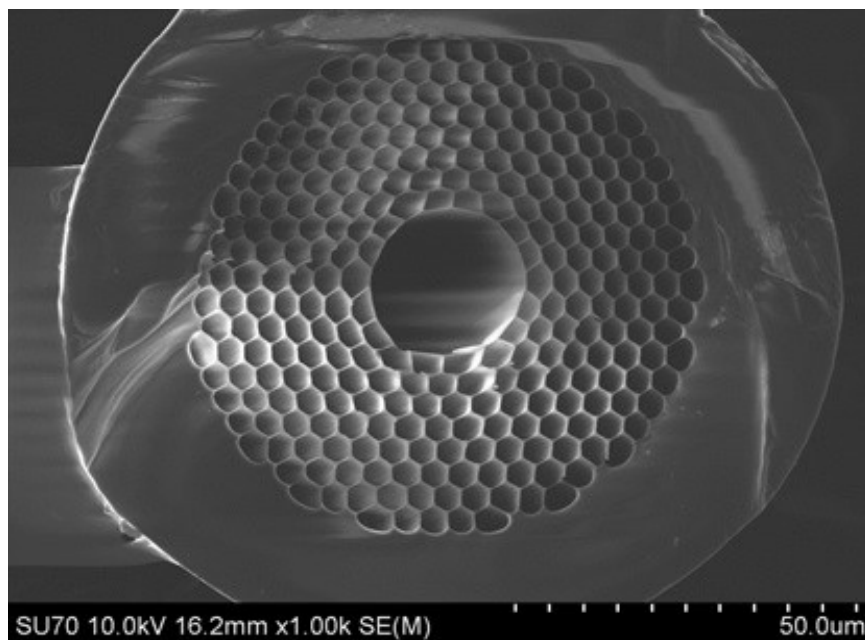
Figure 4.1: Scanning electron microscope image of the HC-PCF.

The idea of using a HC-PCF for gas and liquid sensing is relatively new, although a number of recent articles have been published using a HC-PCF gas cell with various spectroscopy techniques, such as Cavity Ring-Down Spectroscopy (CRDS) [106;107], wavelength modulation spectroscopy (WMS) [108], ICAS [109], and Raman spectroscopy [110]. One of the main drawbacks of gas cells based on HC-PCF is the time required to

evacuate and fill longer lengths of the hollow core fiber [71;111-113]. Many techniques have been proposed to reduce evacuation and filling times, such as splicing the HC-PCF to a normal single-mode fiber and filling the core at a higher pressure [18], or drilling holes along the length of the HC-PCF allowing the gas to diffuse quicker [72;73;114]. In addition, techniques have been investigated to simplify coupling light into and out of the HC-PCF, such as using specially designed mechanical splices [115;116], or specially designed fibers for gas access after splicing [117]. Types of HC-PCF based gas cell are commercially available but they are fixed in length and costly (e.g., HC-PCF gas cells from GLO Photonics, UK for developing gas based lasers).

4.2 RESULTS AND DISCUSSIONS

The following experimental results were obtained using **Gas Cell 2**, described in section 2.4.2 of Chapter 2. Experiments were first performed using the direct absorption spectroscopy (DAS) technique for a comparison between the absorbed signals for the different lengths of HC-PCF. The source for the DAS measurements was the ASE from the erbium-doped fiber which was coupled into the HC-PCF based gas cell, using the configuration shown in **Figure 2.14**. The gas sample was allowed to diffuse through one end of the fiber while the other end was maintained at constant vacuum level of 0.2 mbar or below. The output from the gas cell was coupled to a single mode fiber (SMF) and directly connected to the optical spectrum analyzer (OSA) for monitoring. As discussed in Chapter 3, N_2O possesses relatively high absorption lines in the ~ 1522 nm region, however the gain-coefficient of erbium-doped fiber in this region is much lower compared to that of the 1535 nm and 1555 nm regions. **Figure 4.2** shows the rotational lines in the $3\upsilon_3$ overtone band for

N$_2$O, obtained using Spectral Calculator, GATS [41;85], which was overlaid with the erbium doped fiber ASE from 1516 nm to 1536 nm. Since erbium-doped fiber is a homogeneous gain medium at normal temperatures the lasing wavelength is determined by the local maximum of the gain curve, this means that a laser cavity without a FBG would typically lase in the 1535 nm region.
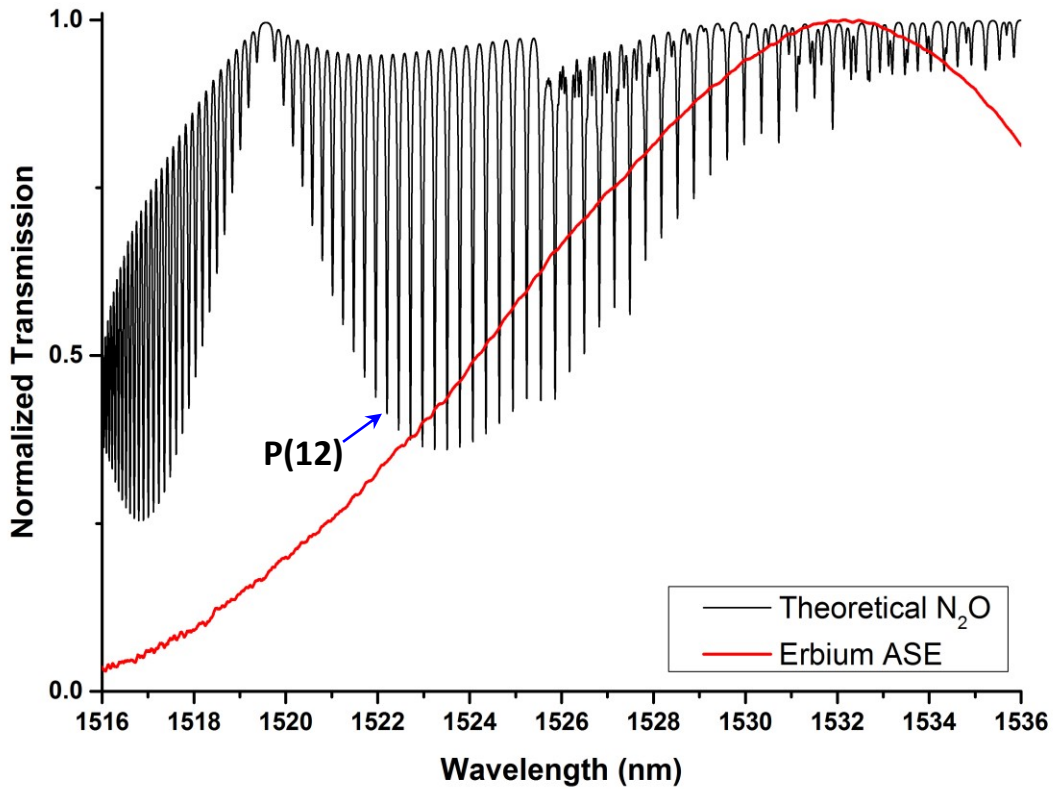
Figure 4.2: A section of the experimentally obtained emission spectrum of erbium with the theoretical absorption spectrum of $3\upsilon_3$ absorption band of N$_2$O superimposed.

Figure 4.3 and **Figure 4.4** shows the absorption spectra from the direct absorption measurements from 10% N$_2$O gas using a 20 m and 40 m long HC-PCF respectively, after subtracting the N$_2$ reference scans. **Figure 4.5** shows the transmission spectrum with the N$_2$ gas in the cell and 10 % N$_2$O in the cell with 40 m long HC-PCF. When evacuating the

higher concentration gas samples from the HC-PCF, such as 10% N_2O, multiple cycles of evacuating and filling with N_2 were required to ensure there was no residual gas left in both the core and the surrounding cladding holes, as shown in **Figure 4.1**. However, it is anticipated that the majority of the laser power is confined to the core of HC-PCF and the effect of absorption due to gas inside the cladding holes is minimal, if not insignificant, for low concentrations.
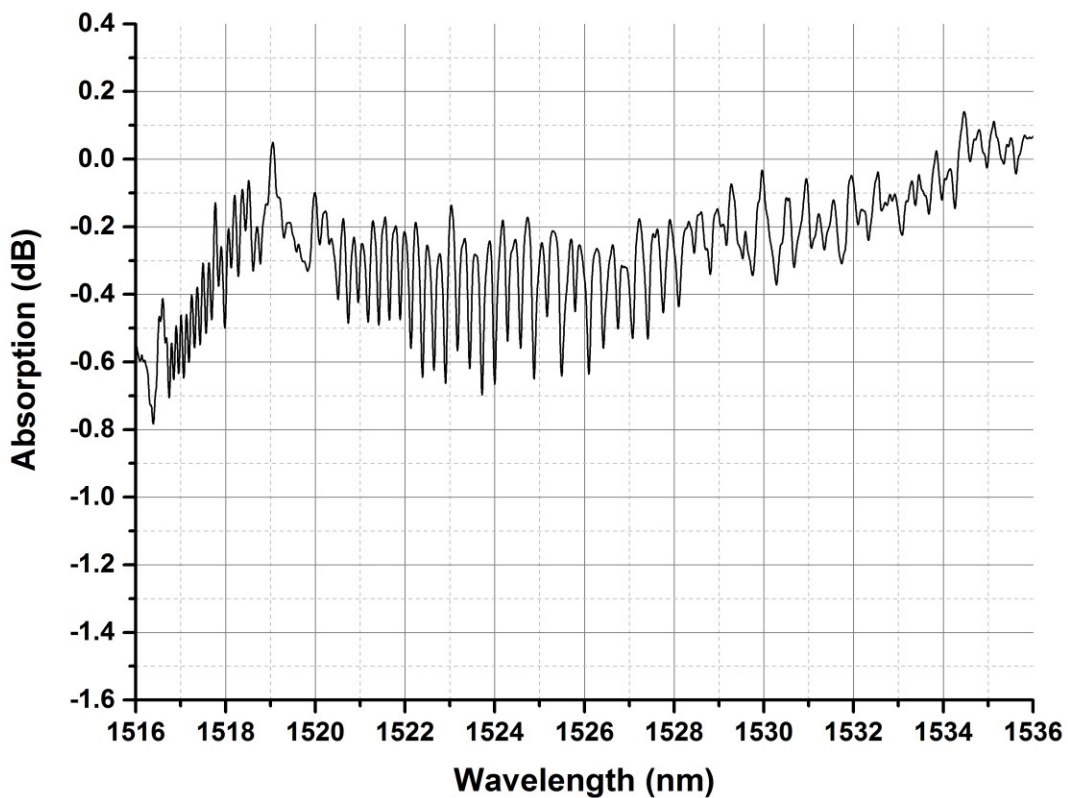
Figure 4.3: Direct absorption spectrum of 10% N_2O gas in the 20 m of HC-PCF after subtraction from the background (N_2 gas) spectra.
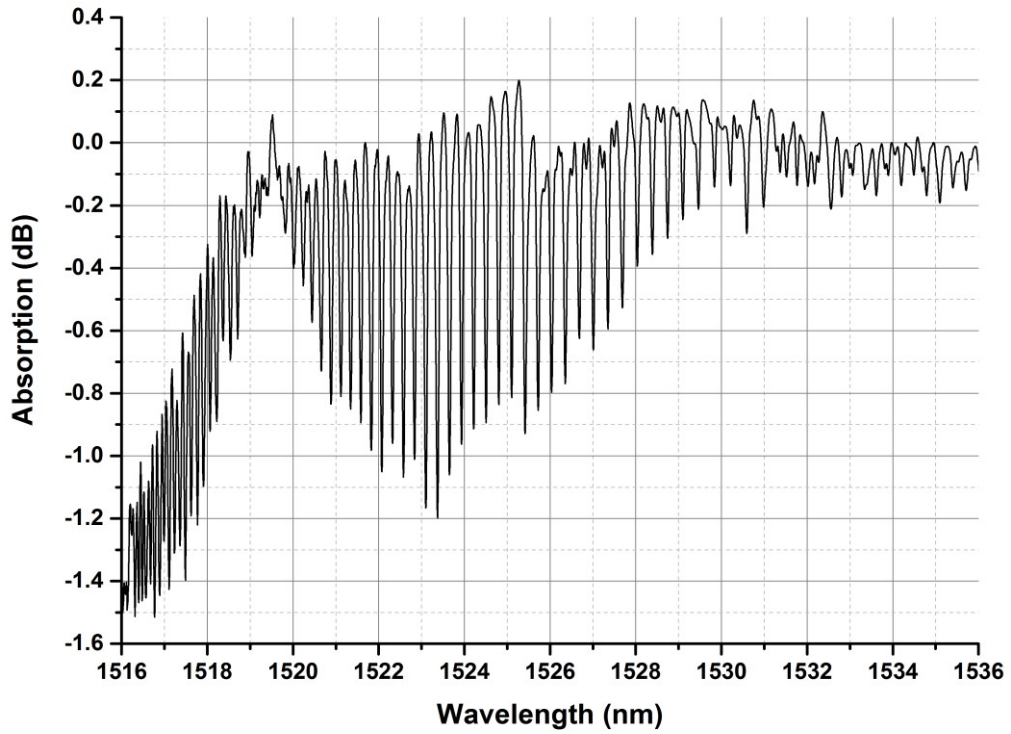
Figure 4.4: Direct absorption spectrum of 10% N_2O gas in the 40 m of HC-PCF after subtraction from the background (N_2 gas) spectra.
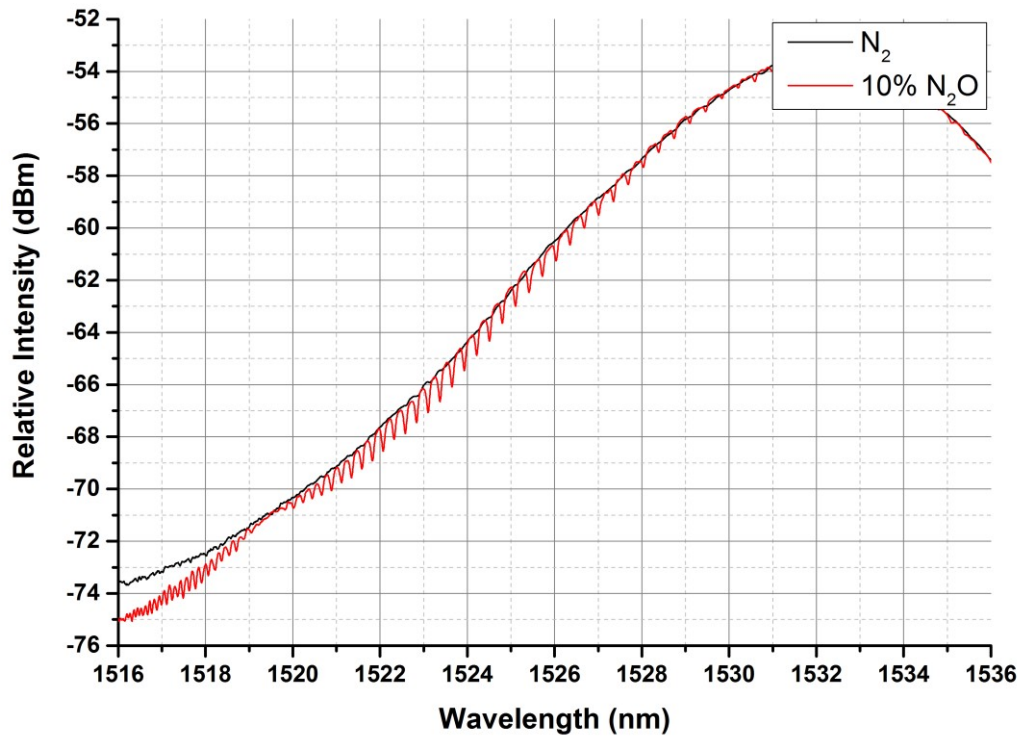
Figure 4.5: Transmission spectrum with N_2 (BLACK) in the gas cell and with 10 % N_2O in the gas cell (RED).

After the DAS measurements were completed the HC-PCF gas cell was incorporated into the laser cavity as shown in **Figure 2.18**. The experimental configuration produced a multi-longitudinal mode laser output, which was selected by the FBG. The laser was kept near the threshold condition, so that the ASE at the FBG wavelength was also close to the threshold condition. Thus, the longitudinal modes which fell within the FBG bandwidth made multiple passes around the cavity, and enhanced the effective path length. Further, the complete interaction of the laser radiation with the sample gas inside the fiber core helps to improve the detection sensitivity. **Figure 4.6** shows the transmission spectra of the N_2 reference gas, 0.1% N_2O, and 10% N_2O using a 40 m length of HC-PCF. All of the experimental data was collected and processed as describe in **Appendix B**. The gas cell was flushed with N_2 before and after filling the cell with the N_2O gas samples at different concentrations, spectrum data was also collected with the N_2 gas in the cell during this process. The absorption spectrum in **Figure 4.7** was obtained from the data for N_2O (10%) and N_2 shown in **Figure 4.6**. The experiment was repeated with 20 m long hollow core fiber, the absorption spectrum with 10% N_2O in the 20 m fiber is shown in **Figure 4.8.**
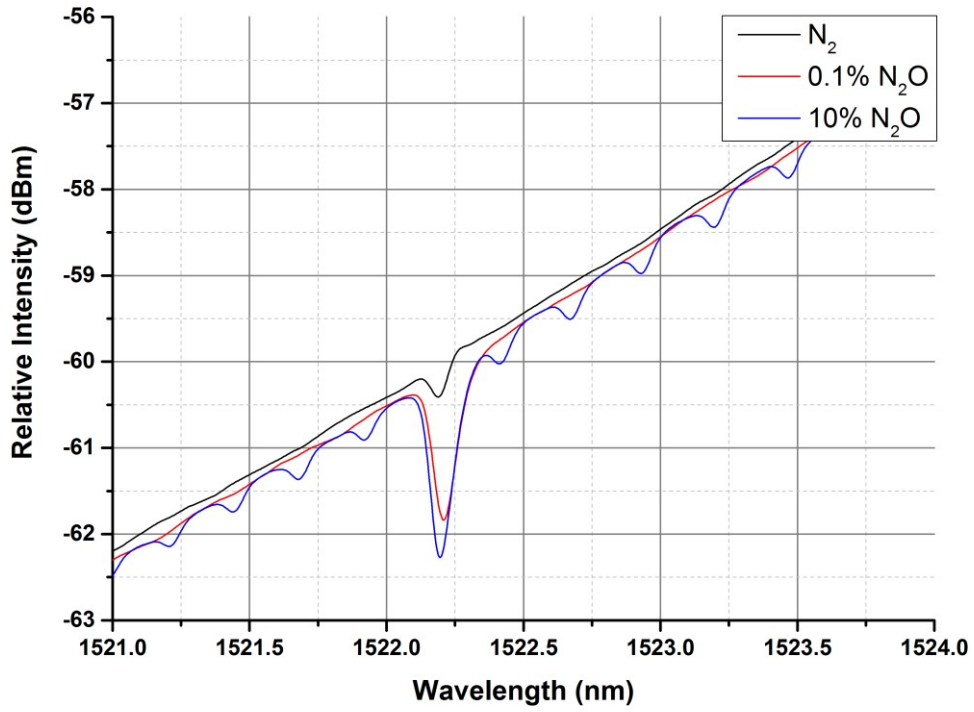
Figure 4.6: Transmission spectrum for the background N_2, 0.1% N_2O, and 10% N_2O using ICAS configuration with the 40 m HC-PCF.
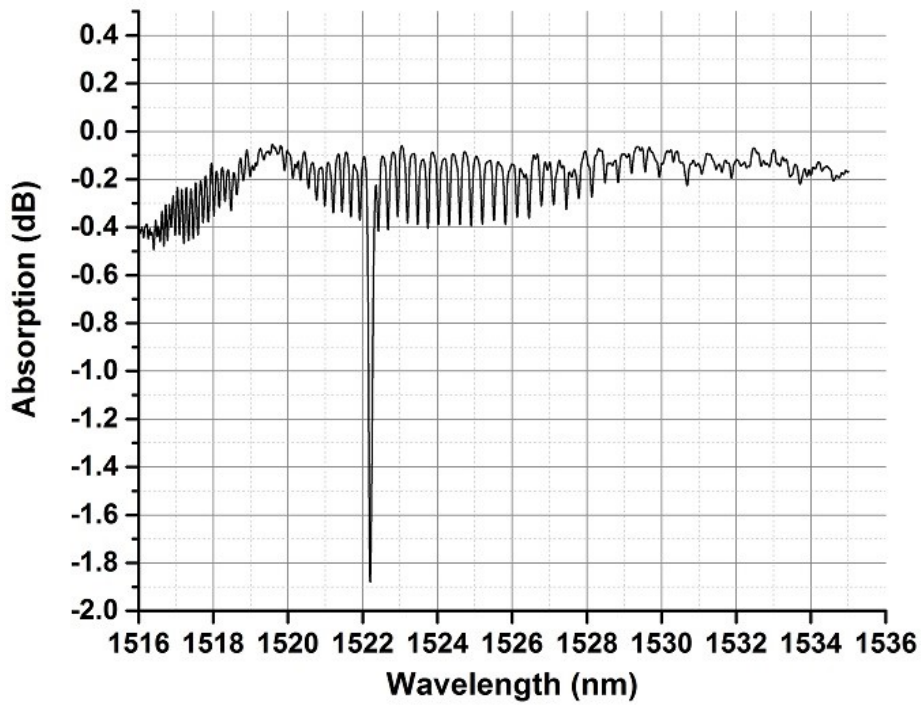
Figure 4.7: Absorption spectrum from 10% N_2O in the 40 m HC-PCF in the ICAS system.

93
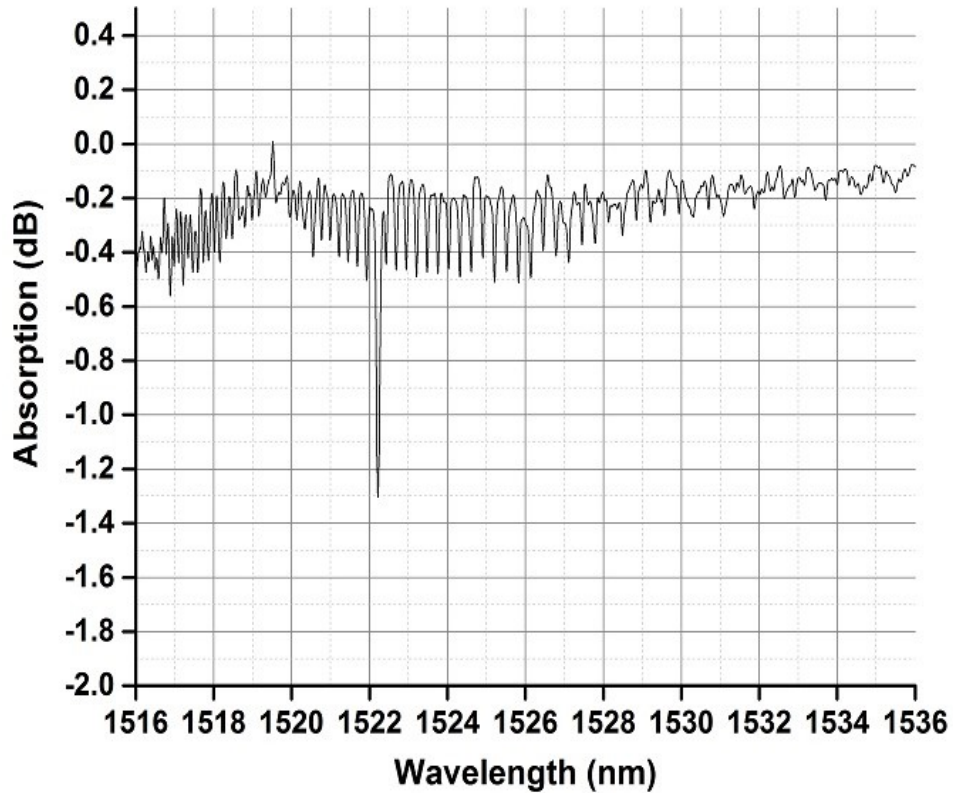
Figure 4.8: Absorption spectrum from 10% N_2O in the 20 m HC-PCF in the ICAS system.

It is evident from the absorption spectra obtained with the 20 m and 40 m long HC-PCF using both the DAS technique (**Figure 4.3** and **Figure 4.4**) and the ICAS technique (**Figure 4.8** and **Figure 4.7**) that the detection sensitivity increases at the FBG location. In order to determine the minimum detectable concentration, different concentrations of N_2O gas were tested in the system with the 40 m length of HC-PCF. **Figure 4.9** is the transmission spectra of the background N_2 and for 10 ppmv N_2O and the resulting absorption spectrum is shown in **Figure 4.10**.
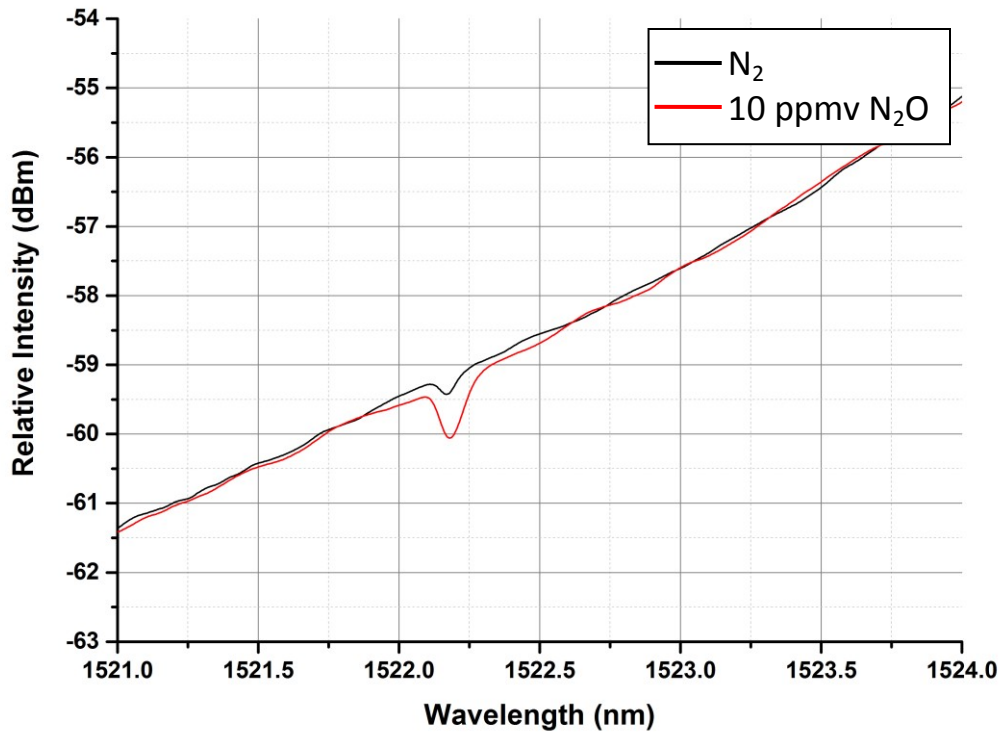
Figure 4.9: Transmission spectrum of N_2 and 10 ppmv N_2O in the 40 m HC-PCF gas cell.
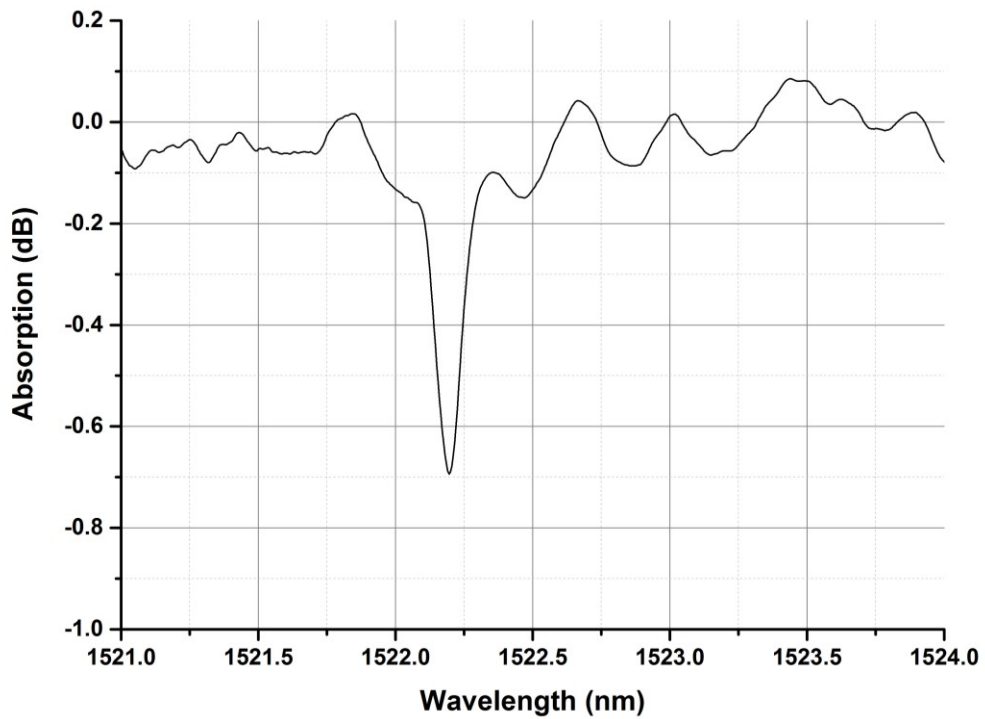
Figure 4.10: Absorption spectrum due to 10 ppmv concentration of N_2O in the 40 m HC-PCF gas cell.

The minimum concentration the system could detect was ~ 500 ppbv (**Figure 4.11**) with

the 40 m length of HC-PCF. The 500 ppbv concentration was a standard provided by

Praxair, Canada, and was a certified concentration of $520 \pm 5\%$ ppbv with a N_2 balance.
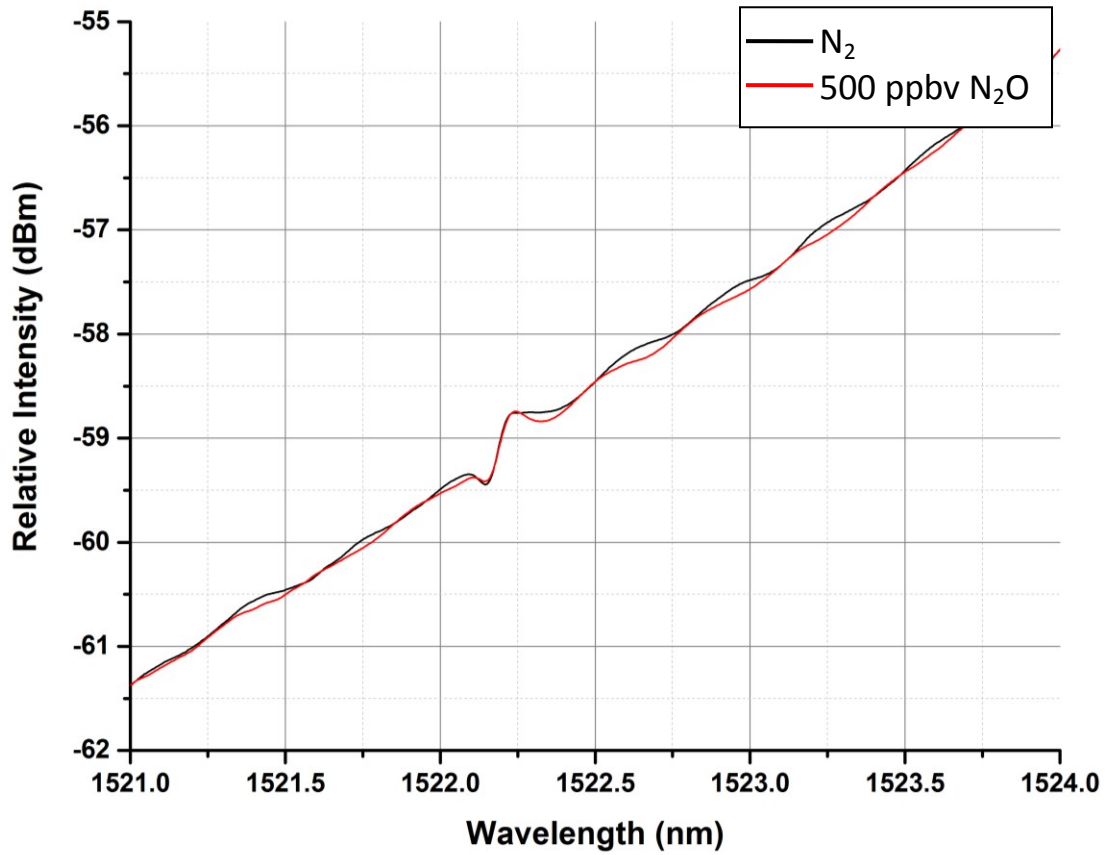
Figure 4.11: Transmission spectrum of N_2 background and ~500 ppbv concentration of N_2O in the 40 m HC-PCF using the ICAS configuration.

4.3 CONCLUSIONS

This chapter discussed the application of the in house fabricated HC-PCF gas cell for the detection of nitrous oxide gas. The gas cell was incorporated inside a ring cavity as an intracavity gas cell. Since the system was formed using only fiber components, a very compact design can be achieved. In addition, the laser cavity supported multi-longitudinal modes within the FBG bandwidth, which increased the sensitivity. The HC-PCF based gas cell shows promise for very low concentration detection but with a long evacuation and filling time. Hence, this gas cell with long lengths of HC-PCF would have limited uses where a fast response time is desired. The efficiency of the system can be increased by reducing gas evacuation and filling times by reducing the fiber length or through previously mentioned techniques. The system was capable of detecting gases at sub-ppmv levels while operating at room temperature.

Chapter 5

Preliminary investigation: Detection of nitrous oxide (N$_2$O) gas from agriculture fields

The research presented in this thesis was done for the development of a portable gas detection system to monitor nitrous oxide (N$_2$O) emissions from agricultural fields. A static gas chamber was constructed and deployed in field for N$_2$O sample collection *in situ* after the application of fertilizer. The procedure was done to assist in determining the flux of N$_2$O gas emitted from a soil treated with urea based fertilizer. This chapter will discuss some preliminary work done using the static gas chamber.

5.1 INTRODUCTION

Nitrous oxide (N$_2$O) is naturally produced in soils as a result of the nitrification and denitrification processes in the nitrogen cycle. Denitrification occurs when nitrates in the soil are broken down by denitrifying micro organisms resulting in nitrogen based gases (e.g., NO, N$_2$O, and N$_2$) being emitted [118;119]. The amount of nitrogen gases produced is dependent on the soil and climate conditions, as oxygen starved soil results in more denitrification [120]. Furthermore, the use of a nitrogen based fertilizer increases the amount of N$_2$O

released [121]. Hence, measuring the N_2O concentration or flux is important to help determine the amount of N_2O being produced due to the application of fertilizer.

Some of the more prominent methods for greenhouse gas (GHG) monitoring are the gradient method, micro-meteorological eddy covariance method, and chamber methods [122]. The gradient method is used to determine the gas flux through a vertical concentration gradient in a soil profile. This can be done in many different ways, one of which involves inserting sample tubes into the soil to different depths and monitoring the analyte concentrations.

The eddy covariance is a technique used to estimate the net flux of the gases emitted from the soil of an agricultural field or ecosystem. This method considers the soil surface to be either the source or sink of the flux and determines the net flux above the soil surface through the covariance of the vertical velocity of eddies and instantaneous gas concentrations. Eddies are the result of turbulent motion (wind) in the atmospheric boundary layer. Eddy covariance flux measurements rely on these turbulent motions to determine net flux; hence, if there is little to no wind accurate flux measurements cannot be made. Furthermore, the flux is determined assuming that measurements are made up wind on terrain which is flat and uniform such that the horizontal flux divergences are negligible [123]. Since turbulence can change very rapidly, anemometers and gas analyzers with fast response times are required to limit the error in the calculated net flux. The eddy covariance method has the benefit of continuous net flux estimations on a landscape scale area based on different sources of flux (i.e., soil flux, plant respiration) [124].

There are many different types of chamber methods and in this preliminary work the static chamber technique was employed for gas collection [125]. A static chamber is installed into

the soil at the location of interest so that as the gases are emitted they are collected within the chamber. The concentration of the emitted gas in the chamber will gradually increase. By extracting gas samples from the chamber at regular intervals the flux from the soil can be determined by the expression [126],

$$F = \frac{V}{A}\frac{dC}{dt} \qquad (5.1)$$

where V is the volume of gas enclosed by the chamber, A is the surface area of the enclosed soil, and $\frac{dC}{dt}$ is the rate of change of the analyte (N_2O) concentration in the chamber. A static chamber is made of a non-reactive material and composed of two parts; an anchor (base) and a lid (**Figure 5.1**). The anchor is permanently installed $2.5 - 13$ cm into the soil [127] and the lid is only placed on the anchor when samples are being collected. The lid is equipped with a valve for withdrawing a gas sample, as well as with a small vent hole to accommodate any changes in pressure due to temperature change or gas emission in the chamber during sample collection [128]. Though the chamber method is excellent for determining localized soil emissions, their presence can disturb the micro-climate which can potentially alter the amount of gas produced [122;128].

5.2 FIELD SETUP

In order to test the sensitivity of the developed N_2O detection system for in-field operation a static gas chamber was constructed and deployed in-field for sample collection. A 1.35 m x 0.75 m x 0.2 m (L x W x H) gas chamber was constructed and installed in a soil research plot located in the Lakehead University community garden (**Figure 5.1**). The gas chamber base was pressed into the soil to a depth of ~5 cm. When the chamber was sealed with the lid it

would encompass a volume of ~150 L. The anchor had an inner rim for mounting the lid and was filled with water to form an air tight seal, as described by Christiansen et al. [129].

Figure 5.1: The installed static gas chamber.

A urea fertilizer, provide by Agrium, was applied to the soil in the gas chamber. This specific fertilizer (ESN Smart Nitrogen) was coated with a polymer which allows for the release of the urea above a specific temperature and moisture level. The soil was lightly watered after the fertilizer was applied and an initial single sample was collected (for Day 0). Soil gas samples were collected every 6 days over the course of a 31 day period, starting on Day 1. On each day 4 gas samples were collected. The gas samples were collected at 15 minute intervals giving samples at 0 min, 15 min, 30 min, and 45 min. Each gas sample was collected over the duration of 2 minutes and had a total volume of ~7 L per sample (**Figure 5.2**). Furthermore, gas collection was done in the mid morning and the atmospheric and soil

conditions were recorded [130]. This experiment was carried out from mid-July to mid-August.

Figure 5.2: Vacuum pump draws a sample from the sealed static gas chamber.

5.3 RESULTS AND DISCUSSION

All of the samples collected from the static gas chamber were analyzed in a Varian 450 gas chromatography (GC) system. The GC results showed that there was no variation between the N_2O levels in the collected gas samples, i.e. all N_2O sample were at atmospheric

levels. This could be attributed to overly dry soil conditions. However, denitrification (N_2O production) is dependent on many variables related to soil conditions such as moisture, temperature, oxygen levels, pH levels, and nitrate and ammonia levels [120]. The experiment will be repeated and a thorough investigation will be done in the future.

5.4 CONCLUSION

Gas sampling using a static chamber system was conducted. The chamber was deployed in a research plot with urea mixed into the soil. Multiple soil gas samples were collected over the course of 31 days with all of the samples showing no variation in N_2O concentration. This work was done as preliminary step towards implementing the developed system in the field.

Chapter 6

Summary

The basis of this dissertation was the development of a fiber laser for trace gas detection. The research presented demonstrated the detection of concentrations in sub parts-per-million by volume (ppmv) of nitrous oxide (N_2O) and acetylene (C_2H_2) gases using the fiber laser system based on the intracavity absorption spectroscopy technique (ICAS). The system incorporated a fiber Bragg grating (FBG) which improved the ICAS sensitivity. A saturable absorber was incorporated inside the cavity in order to reduce the mode-hopping of the laser. The system can be stabilized further by using an active stabilization technique. The efficiency and sensitivity was investigated with two gas cells: a Herriott multi-pass cell and an in-house developed gas cell based on hollow-core photonic crystal fiber (HC-PCF). Both cell configurations demonstrated the capability of sub-ppmv concentration detection. The Herriott cell provided a higher sensitivity and a quicker fill time than the HC-PCF cell, however the HC-PCF cell has the benefit requiring very small space and sample volume. Although, this research only demonstrated the systems application for the detection of N_2O or C_2H_2, the ICAS system developed has the potential to be applied to any absorption feature which falls within the erbium emission spectrum by simply changing the FBG or by incorporating a tunable FBG.

The research presented was completed as the foundation for developing a portable real-time N_2O detection system for monitoring emissions in agriculture fields. This system has the potential to replace some of the more labor intensive, large and expensive flux measurement methods with a small and robust system. Based on the experimental results using the Herriott cell, an ICAS detection system will have the capability of offering real-time concentration measurements that would be appealing for monitoring N_2O emissions for fertilization application optimization.

Appendix

APPENDIX A – GAS SAMPLE PREPARATION

The gas samples used throughout the experimental investigation were either certified concentrations commercially available (PRAXAIR, Canada) or concentrations produced in house from the certified gas concentrations. This section outlines the procedures undertaken to achieve the various nonstandard gas concentrations. The different gas concentrations were produced by diluting a certified gas with a balance of research grade 6.0 nitrogen (99.9999% N_2). N_2 was used since it has no near infrared (NIR) absorption band. These mixtures were produced using a computer controlled mass flow controller (OMEGA, model: FMA 5412). A standard gas concentration and the N_2 gas were combined in a 10 L Tedlar bag in specific volumes to obtain the desired gas concentration **(Figure A.1)**. Tedlar bags are made of an inert film and are fitted with a polypropylene valve with septum. Nano-filters were used in order to eliminate contaminants (dust or other debris), as the contaminants could deposit on the mirrors of the Herriott cell, or clog the core of the HC-PCF. In the case of HC-PCF, dust or debris could prevent the gas sample or light from effectively being transmitted through the fiber.
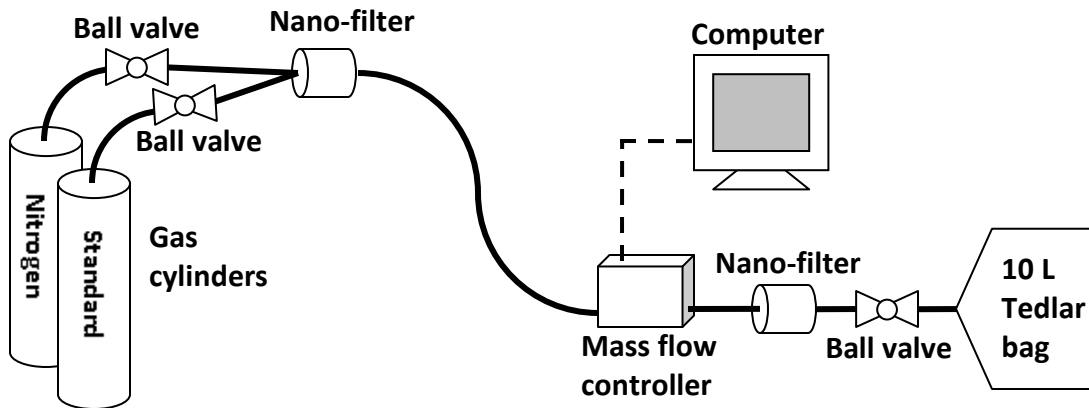
Figure A.1: The gas mixing schematic.

Figure A.1 shows the gas mixing system, which was flushed with N_2 gas before each concentration was mixed. Once this was completed a Tedlar bag was connected to the mass flow controller. The mass flow controller allowed for flow rates from 0.1 L/min – 0.5 L/min. The durations and flow rates used were based on the concentration being prepared. When preparing different gas concentrations the sample bag was first filled with the N_2 gas. The system was then flushed with the standard gas prior to filling the sample bag. For example, to prepare a 6 L sample of a 0.1 ppmv N_2O concentration, a sample bag was filled with 5.92 L of N_2 at 0.5 L/min. for 11 minutes 50 seconds, and 0.08 L of 9.95 ppmv N_2O at 0.1 L/min. for 48 seconds.

All gas concentrations prepared in house could confidently be produced to a hundredth of the standard concentration, though they were generally only made to a twentieth of standard concentration. Lower concentration mixtures were verified by gas chromatography (Varian 450-GC).

APPENDIX B - DATA ACQUISITION

All of the data collected in this dissertation was done using an automated acquisition program written in LabVIEW 2013 SP1. All of the output spectra were recorded with an ANDO AQ6317B optical spectrum analyzer (OSA). The OSA had a spectral resolution of 0.01 nm. After the gas filling process was complete, 10 spectra were recorded on the OSA and collected by the LabVIEW program. A set of 10 scans would typically be taken over the course of 10 minutes, but depending on the spectrum width each set might be taken over the duration of 6 to 20 minutes. Spectra for both the gas sample and the background N_2 gas were recorded. In order to minimize the random intensity fluctuations that occur in the individual outputs, each set of 10 spectrums were averaged before data processing. Once they were averaged they could be used to recover the change in intensity due to absorption. The transmission/absorption spectrums were recovered by subtracting an averaged data set of the sample gas from an averaged set of the background N_2 spectrums, or vice versa. Background N_2 spectrums were collected before and after each analyte gas.

References

[1] F. P. Kapron, D. B. Keck, and R. D. Maurer, "Radiation losses in glass optical waveguides," *Applied Physics Letters*, vol. 17, no. 10, pp. 423-425, 1970.

[2] R. Mary, D. Choudhury, and A. K. Kar, "Applications of Fiber Lasers for the Development of Compact Photonic Devices," *Ieee Journal of Selected Topics in Quantum Electronics*, vol. 20, no. 5 Sept.2014.

[3] G. Keiser, *Optical Fiber Communications*, 3 ed. Boston, MA: McGraw Hill, 2000.

[4] A. K. Ghatak and K. Thyagarajan, *An Introduction to Fiber Optics*, illustrated, reprint ed Cambridge University Press, 1998.

[5] S. D. Jackson and G. Anzueto-Sanchez, "Chalcogenide glass Raman fiber laser," *Applied Physics Letters*, vol. 88, no. 22 May2006.

[6] D. Gloge, "Weakly guiding fibers," *Appl. Opt.*, vol. 10, no. 10, pp. 2252-2258, Oct.1971.

[7] R. Mossadegh, J. S. Sanghera, D. Schaafsma, B. J. Cole, V. Q. Nguyen, P. E. Miklos, and I. D. Aggarwal, "Fabrication of single-mode chalcogenide optical fiber," *Journal of Lightwave Technology*, vol. 16, no. 2, pp. 214-217, Feb.1998.

[8] R. H. Stolen, V. Ramaswamy, P. Kaiser, and W. Pleibel, "Linear Polarization in Birefringent Single-Mode Fibers," *Applied Physics Letters*, vol. 33, no. 8, pp. 699-701, 1978.

[9] Y. Fujii and K. Sanos, "Polarization transmission characteristics of optical fibers with elliptical cross section," *Electron. Comm. Jpn.*, vol. 63, no. 8, pp. 87-93, 1980.

[10] M. N. Zervas and C. A. Codemard, "High Power Fiber Lasers: A Review," *Ieee Journal of Selected Topics in Quantum Electronics*, vol. 20, no. 5 Sept.2014.

[11] R. J. Mears, L. Reekie, S. B. Poole, and D. N. Payne, "Neodymium-Doped Silica Single-Mode Fiber Lasers," *Electronics Letters*, vol. 21, no. 17, pp. 738-740, 1985.

[12] N. Simakov, A. Hemming, W. A. Clarkson, J. Haub, and A. Carter, "A cladding-pumped, tunable holmium doped fiber laser," *Optics Express*, vol. 21, no. 23, pp. 28415-28422, Nov.2013.

[13] J. C. Knight, J. Broeng, T. A. Birks, and P. S. J. Russel, "Photonic band gap guidance in optical fibers," *Science*, vol. 282, no. 5393, pp. 1476-1478, Nov.1998.

[14] S. G. Johnson and J. D. Joannopoulos, *Photonic Crystals: The Road from Theory to Practice* Kluwer Academic Publishers, 2001.

[15] F. Benabid, J. C. Knight, G. Antonopoulos, and P. S. J. Russell, "Stimulated Raman scattering in hydrogen-filled hollow-core photonic crystal fiber," *Science*, vol. 298, no. 5592, pp. 399-402, Oct.2002.

[16] F. Couny, F. Benabid, and P. S. Light, "Subwatt threshold cw raman fiber-gas laser based on H-2-filled hollow-core photonic crystal fiber," *Physical Review Letters*, vol. 99, no. 14 Oct.2007.

[17] A. Jones, A. V. Nampoothiri, T. Fiedler, R. Kadel, W. Hageman, N. Wheeler, F. Couny, F. Benabid, W. Rudolph, K. Corwin, and B. Washburn, "Mid-IR fiber lasers based on molecular gas-filled hollow-core photonic crystal fiber," 2011.

[18] T. Ritari, J. Tuominen, H. Ludvigsen, J. C. Petersen, T. Sorensen, T. P. Hansen, and H. R. Simonsen, "Gas sensing using air-guiding photonic bandgap fibers," *Optics Express*, vol. 12, no. 17, pp. 4080-4087, Aug.2004.

[19] J. L. Zhang and J. W. Y. Lit, "Erbium-Doped Fiber Compound-Ring Laser with A Ring Filter," *Ieee Photonics Technology Letters*, vol. 6, no. 5, pp. 588-590, May1994.

[20] G. A. Ball, W. W. Morey, and W. H. Glenn, "Standing-Wave Monomode Erbium Fiber Laser," *Ieee Photonics Technology Letters*, vol. 3, no. 7, pp. 613-615, July1991.

[21] W. H. Loh, D. Atkinson, P. R. Morkel, M. Hopkinson, A. Rivers, A. J. Seeds, and D. N. Payne, "All-Solid-State Subpicosecond Passively Mode-Locked Erbium-Doped Fiber Laser," *Applied Physics Letters*, vol. 63, no. 1, pp. 4-6, July1993.

[22] D. J. Richardson, J. Nilsson, and W. A. Clarkson, "High power fiber lasers: current status and future perspectives," *Journal of the Optical Society of America B-Optical Physics*, vol. 27, no. 11, p. B63-B92, Nov.2010.

[23] H. C. Lefevre, "Single-Mode Fiber Fractional Wave Devices and Polarization Controllers," *Electronics Letters*, vol. 16, no. 20, pp. 778-780, 1980.

[24] M. J. F. Digonnet and H. J. Shaw, "Analysis of A Tunable Single-Mode Optical Fiber Coupler," *Ieee Journal of Quantum Electronics*, vol. 18, no. 4, pp. 746-754, 1982.

[25] H. Ishio, J. Minowa, and K. Nosu, "Review and Status of Wavelength-Division-Multiplexing Technology and Its Application," *Journal of Lightwave Technology*, vol. 2, no. 4, pp. 448-463, 1984.

[26] K. O. Hill, Y. Fujii, D. C. Johnson, and B. S. Kawasaki, "Photosensitivity in Optical Fiber Waveguides - Application to Reflection Filter Fabrication," *Applied Physics Letters*, vol. 32, no. 10, pp. 647-649, 1978.

[27] R. M. Atkins, V. Mizrahi, and T. Erdogan, "248 nm Induced Vacuum UV Spectral Changes in Optical-Fiber Preform Cores - Support for A Color Center Model of Photosensitivity," *Electronics Letters*, vol. 29, no. 4, pp. 385-387, Feb.1993.

[28] S. J. Frisken, "Transient Bragg Reflection Gratings in Erbium-Doped Fiber Amplifiers," *Optics Letters*, vol. 17, no. 24, pp. 1776-1778, Dec.1992.

[29] T. Y. Tsai and Y. C. Fang, "A saturable absorber Q-switched all-fiber ring laser," *Optics Express*, vol. 17, no. 3, pp. 1429-1434, Feb.2009.

[30] Z. Medendorp, J. Valiunas, and G. Das, "Wavelength-Switchable fiber laser," *Microwave and Opt. Technol. Lett.*, vol. 49, no. 6, pp. 1231-1233, 2007.

[31] Y. Cheng, J. T. Kringlebotn, W. H. Loh, R. I. Laming, and D. N. Payne, "Stable Single-Frequency Traveling-Wave Fiber Loop Laser with Integral Saturable-Absorber-Based Tracking Narrow-Band-Filter," *Optics Letters*, vol. 20, no. 8, pp. 875-877, Apr.1995.

[32] X. Y. Fan, Z. Y. He, Y. Mizuno, and K. Hotate, "Bandwidth-adjustable dynamic grating in erbium-doped fiber by synthesis of optical coherence function," *Optics Express*, vol. 13, no. 15, pp. 5756-5761, July2005.

[33] B. Lee, "Review of the present status of optical fiber sensors," *Optical Fiber Technology*, vol. 9, no. 2, pp. 57-79, Apr.2003.

[34] *Optical Sensors: Industrial Environmental and Diagnostic Applications* Springer, 2004.

[35] J. H. van der Maas, *Basic infrared spectroscopy* Heyden & Son, 1972.

[36] J. D. J. Ingle and S. R. Couch, *Spectrochemical Analysis*. Old Tappan, NJ: Prentice Hall College Book Division, 1988.

[37] T. Engel, *Quantum Chemistry & Spectroscopy*, 2nd ed. Upper Saddle River, NJ: Pearson, 2009.

[38] D. J. Griffiths, *Introduction to Quantum Mechanics*, 2 ed. Upper Saddle River, NJ: Pearson Prentice Hall, 2005.

[39] J. M. Hollas, *Modern Spectroscopy*, 4th ed. Hoboken, NJ: J. Wiley, 2004.

[40] A. D. Bykov, O. V. Naumenko, M. A. Smirnov, L. N. Sinitsa, L. R. Brown, J. Crisp, and D. Crisp, "The Infrared-Spectrum of H2S from 1 to 5 Mu-M," *Canadian Journal of Physics*, vol. 72, no. 11-12, pp. 989-1000, Nov.1994.

[41] L. S. Rothman, I. E. Gordon, Y. Babikov, A. Barbe, D. C. Benner, P. F. Bernath, M. Birk, L. Bizzocchi, V. Boudon, L. R. Brown, A. Campargue, K. Chance, E. A. Cohen, L. H. Coudert, V. M. Devi, B. J. Drouin, A. Fayt, J. M. Flaud, R. R. Gamache, J. J. Harrison, J. M. Hartmann, C. Hill, J. T. Hodges, D. Jacquemart, A. Jolly, J. Lamouroux, R. J. Le Roy, G. Li, D. A. Long, O. M. Lyulin, C. J. Mackie, S. T. Massie, S. Mikhailenko, H. S. P. Muller, O. V. Naumenko, A. V. Nikitin, J. Orphal, V. Perevalov, A. Perrin, E. R. Polovtseva, C. Richard, M. A. H. Smith, E. Starikova, K. Sung, S. Tashkun, J. Tennyson, G. C. Toon, V. G. Tyuterev, and G. Wagner, "The HITRAN 2012 molecular spectroscopic database," *Journal of Quantitative Spectroscopy & Radiative Transfer*, vol. 130, pp. 4-50, Nov.2013.

[42] P. Werle, "A review of recent advances in semiconductor laser based gas monitors," *Spectrochimica Acta Part A-Molecular and Biomolecular Spectroscopy*, vol. 54, no. 2, pp. 197-236, Feb.1998.

[43] P. Werle and F. Slemr, "Signal-To-Noise Ratio Analysis in Laser-Absorption Spectrometers Using Optical Multipass Cells," *Applied Optics*, vol. 30, no. 4, pp. 430-434, Feb.1991.

[44] S. Schilt, L. Thevenaz, and P. Robert, "Wavelength modulation spectroscopy: combined frequency and intensity laser modulation," *Applied Optics*, vol. 42, no. 33, pp. 6728-6738, Nov.2003.

[45] A. Yariv, *Optical Electronics in Modern Communications*, 5 ed. New York: Oxford University Press, 1997.

[46] N. Arsad, M. Li, G. Stewart, and W. Johnstone, "Intra-Cavity Spectroscopy Using Amplified Spontaneous Emission in Fiber Lasers," *Journal of Lightwave Technology*, vol. 29, no. 5, pp. 782-788, Mar.2011.

[47] J. Hodgkinson and R. P. Tatam, "Optical gas sensing: a review," *Measurement Science and Technology*, vol. 24, no. 1 Jan.2013.

[48] V. M. Baev, Latz T., and Toschek P.E., "Laser Intracavity absorption spectroscopy," *Applied Physics B*, vol. 69, pp. 171-202, 1999.

[49] G. Stewart, A. Mencaglia, W. Philp, and W. Jin, "Interferometric signals in fiber optic methane sensors with wavelength modulation of the DFB laser source," *Journal of Lightwave Technology*, vol. 16, no. 1, pp. 43-53, Jan.1998.

[50] J. Reid and D. Labrie, "Second-Harmonic Detection with Tunable Diode Lasers - Comparison of Experiment and Theory," *Applied Physics B-Photophysics and Laser Chemistry*, vol. 26, no. 3, pp. 203-210, 1981.

[51] G. Stewart, W. Johnstone, J. R. P. Bain, K. Ruxton, and K. Duffin, "Recovery of Absolute Gas Absorption Line Shapes Using Tunable Diode Laser Spectroscopy With Wavelength Modulation-Part I: Theoretical Analysis," *Journal of Lightwave Technology*, vol. 29, no. 6, pp. 811-821, Mar.2011.

[52] R. Engelbrecht, "A compact NIR fiber-optic diode laser spectrometer for CO andCO(2): analysis of observed 2f wavelength modulation spectroscopy line shapes," *Spectrochimica Acta Part A-Molecular and Biomolecular Spectroscopy*, vol. 60, no. 14, pp. 3291-3298, Dec.2004.

[53] G. Stewart, K. Atherton, H. B. Yu, and B. Culshaw, "An investigation of an optical fibre amplifier loop for intra-cavity and ring-down cavity loss measurements," *Measurement Science & Technology*, vol. 12, no. 7, pp. 843-849, July2001.

[54] Z. X. Li, W. G. Ma, X. F. Fu, W. Tan, G. Zhao, L. Dong, L. Zhang, W. B. Yin, and S. T. Jia, "Continuous-wave cavity ringdown spectroscopy based on the control of cavity reflection," *Optics Express*, vol. 21, no. 15, pp. 17961-17971, July2013.

[55] A. W. Liu, S. Kassi, P. Malara, D. Romanini, V. I. Perevalov, S. A. Tashkun, S. M. Hu, and A. Campargue, "High sensitivity CW-cavity ring down spectroscopy of N2O near 1.5 mu m (I)," *Journal of Molecular Spectroscopy*, vol. 244, no. 1, pp. 33-47, July2007.

[56] A. Elia, P. M. Lugara, C. Di Franco, and V. Spagnolo, "Photoacoustic Techniques for Trace Gas Sensing Based on Semiconductor Laser Sources," *Sensors*, vol. 9, no. 12, pp. 9616-9628, Dec.2009.

[57] G. A. West, J. J. Barrett, D. R. Siebert, and K. V. Reddy, "Photoacoustic Spectroscopy," *Review of Scientific Instruments*, vol. 54, no. 7, pp. 797-817, 1983.

[58] P. Patimisco, G. Scamarcio, F. K. Tittel, and V. Spagnolo, "Quartz-Enhanced Photoacoustic Spectroscopy: A Review," *Sensors*, vol. 14, no. 4, pp. 6165-6206, Apr.2014.

[59] M. E. Webber, M. Pushkarsky, and C. K. N. Patel, "Fiber-amplifier-enhanced photoacoustic spectroscopy with near-infrared tunable diode lasers," *Applied Optics*, vol. 42, no. 12, pp. 2119-2126, Apr.2003.

[60] B. Lohden, S. Kuznetsova, K. Sengstock, V. M. Baev, A. Goldman, S. Cheskis, and B. Palsdottir, "Fiber laser intracavity absorption spectroscopy for in situ multicomponent gas analysis in the atmosphere and combustion environments," *Applied Physics B-Lasers and Optics*, vol. 102, no. 2, pp. 331-344, Feb.2011.

[61] T. Ueda, N. Kato, A. Takemura, H. Koishi, and A. Morinaga, "Intracavity absorption spectroscopy with a tunable multimode traveling-wave ring Ti:sapphire laser," *Applied Optics*, vol. 51, no. 20, pp. 4660-4666, July2012.

[62] J. Ye, L. S. Ma, and J. L. Hall, "Ultrasensitive detections in atomic and molecular physics: demonstration in molecular overtone spectroscopy," *Journal of the Optical Society of America B-Optical Physics*, vol. 15, no. 1, pp. 6-15, Jan.1998.

[63] F. M. Schmidt, A. Foltynowicz, W. G. Ma, T. Lock, and O. Axner, "Doppler-broadened fiber-laser-based NICE-OHMS - Improved detectability," *Optics Express*, vol. 15, no. 17, pp. 10822-10831, Aug.2007.

[64] P. Kluczynski, M. Jahjah, L. Nahle, O. Axner, S. Belahsene, M. Fischer, J. Koeth, Y. Rouillard, J. Westberg, A. Vicet, and S. Lundqvist, "Detection of acetylene impurities in ethylene and polyethylene manufacturing processes using tunable diode laser spectroscopy in the 3-mu m range," *Applied Physics B-Lasers and Optics*, vol. 105, no. 2, pp. 427-434, Nov.2011.

[65] T. Shimanouchi, *Tables of Molecular Vibrational Frequencies Consolidated Volume 1*, 6 ed 1972.

[66] S. L. Gilbert and W. C. Swann, "Acetylene $^{12}C_2H_2$ Absorption Reference for 1510 nm to 1540 nm Wavelength Calibration - SRM 2517a," *NIST Special Publication*, vol. 260, no. 133 2001.

[67] W. J. Miniscalco, "Erbium-Doped Glasses for Fiber Amplifiers at 1500-Nm," *Journal of Lightwave Technology*, vol. 9, no. 2, pp. 234-250, Feb.1991.

[68] W. L. Barnes, R. I. Laming, E. J. Tarbox, and P. R. Morkel, "Absorption and Emission Cross-Section of Er3+ Doped Silica Fibers," *Ieee Journal of Quantum Electronics*, vol. 27, no. 4, pp. 1004-1010, Apr.1991.

[69] P. C. Becker, N. A. Olsson, and J. R. Simpson, *Erbium-Doped Fiber Amplifiers: Fundamentals and Technology*, 1 ed. San Diego: Academic Press, 2010.

[70] R. Kashyap, *Fiber Bragg Gratings*, 2nd ed Academic Press, 2010.

[71] J. Henningsen and J. Hald, "Dynamics of gas flow in hollow core photonic bandgap fibers," *Applied Optics*, vol. 47, no. 15, pp. 2790-2797, May2008.

[72] A. van Brakel, C. Grivas, M. N. Petrovich, and D. J. Richardson, "Micro-channels machined in microstructured optical fibers by femtosecond laser," *Optics Express*, vol. 15, no. 14, pp. 8731-8736, July2007.

[73] C. J. Hensley, D. H. Broaddus, C. B. Schaffer, and A. L. Gaeta, "Photonic band-gap fiber gas cell fabricated using femtosecond micromachining," *Optics Express*, vol. 15, no. 11, pp. 6690-6695, May2007.

[74] J. P. Parry, B. C. Griffiths, N. Gayraud, E. D. McNaghten, A. M. Parkes, W. N. MacPherson, and D. P. Hand, "Towards practical gas sensing with micro-structured fibres," *Measurement Science and Technology*, vol. 20, no. 7 July2009.

[75] Q. Kou, G. Guelachvili, M. A. Temsamani, and M. Herman, "The Absorption-Spectrum of C2H2 Around Nu(1)+Nu(3) - Energy Standards in the 1.5 Mu-M Region and Vibrational Clustering," *Canadian Journal of Physics*, vol. 72, no. 11-12, pp. 1241-1250, Nov.1994.

[76] Z. J. Chaboyer, P. J. Moore, and G. Das, "Medium power single-mode single-wavelength fiber laser," *Optics Commun.*, vol. 282, pp. 3100-3103, 2009.

[77] M. L. Cayuela, L. van Zwieten, B. P. Singh, S. Jeffery, A. Roig, and M. A. Sanchez-Monedero, "Biochar's role in mitigating soil nitrous oxide emissions: A review and meta-analysis," *Agriculture Ecosystems & Environment*, vol. 191, pp. 5-16, June2014.

[78] F. A. Phillips, R. Leuning, R. Baigenta, K. B. Kelly, and O. T. Denmead, "Nitrous oxide flux measurements from an intensively managed irrigated pasture using micrometeorological techniques," *Agricultural and Forest Meteorology*, vol. 143, no. 1-2, pp. 92-105, Mar.2007.

[79] A. J. Glenn, M. Tenuta, B. D. Amiro, S. E. Maas, and C. Wagner-Riddle, "Nitrous oxide emissions from an annual crop rotation on poorly drained soil on the Canadian Prairies," *Agricultural and Forest Meteorology*, vol. 166, pp. 41-49, Dec.2012.

[80] A. Campargue, D. Permogorov, M. Bach, M. A. Temsamani, J. V. Auwera, M. Herman, and M. Fujii, "Overtone Spectroscopy in Nitrous-Oxide," *Journal of Chemical Physics*, vol. 103, no. 14, pp. 5931-5938, Oct.1995.

[81] L. Wang, V. I. Perevalov, S. A. Tashkun, B. Gao, L. Y. Hao, and S. M. Hu, "Fourier transform spectroscopy of N2O weak overtone transitions in the 1-2 mu m region," *Journal of Molecular Spectroscopy*, vol. 237, no. 2, pp. 129-136, June2006.

[82] B. Gao, C. Y. Wang, Y. Lu, A. W. Liu, and S. M. Hu, "High-resolution infrared spectroscopy of N-15(2) O-16 in the 3500-9000 cm(-1) region," *Journal of Molecular Spectroscopy*, vol. 259, no. 1, pp. 20-25, Jan.2010.

[83] K. F. Song, A. W. Liu, H. Y. Ni, and S. M. Hu, "Fourier-trans form spectroscopy of (NNO)-N-15-N-14-O-16 in the 3500-9000 cm(-1) region," *Journal of Molecular Spectroscopy*, vol. 255, no. 1, pp. 24-31, May2009.

[84] H. Y. Ni, K. F. Song, V. I. Perevalov, S. A. Tashkun, A. W. Liu, L. Wang, and S. M. Hu, "Fourier-transform spectroscopy of (NNO)-N-14-N-15-O-16 in the 3800-9000 cm(-1) region and global modeling of its absorption spectrum," *Journal of Molecular Spectroscopy*, vol. 248, no. 1, pp. 41-60, Mar.2008.

[85] R. A. Toth, "Line positions and strengths of N2O between 3515 and 7800 cm(-1)," *Journal of Molecular Spectroscopy*, vol. 197, no. 2, pp. 158-187, Oct.1999.

[86] A. W. Liu, S. Kassi, P. Malara, D. Romanini, V. I. Perevalov, S. A. Tashkun, S. M. Hu, and A. Campargue, "High sensitivity CW-cavity ring down spectroscopy of N2O near 1.5 mu m (I)," *Journal of Molecular Spectroscopy*, vol. 244, no. 1, pp. 33-47, July2007.

[87] A. W. Liu, S. Kassi, V. I. Perevalov, S. A. Tashkun, and A. Campargue, "High sensitivity CW-cavity ring down spectroscopy of N2O near 1.5 mu m (II)," *Journal of Molecular Spectroscopy*, vol. 244, no. 1, pp. 48-62, July2007.

[88] A. M. Parkes, A. R. Linsley, and A. J. Orr-Ewing, "Absorption cross-sections and pressure broadening of rotational lines in the 3 nu(3) band of N2O determined by diode laser cavity ring-down spectroscopy," *Chemical Physics Letters*, vol. 377, no. 3-4, pp. 439-444, Aug.2003.

[89] E. Bertseva, A. Campargue, V. I. Perevalov, and S. A. Tashkun, "New observations of weak overtone transitions of N2O by ICLAS-VeCSEL near 1.07 mu m," *Journal of Molecular Spectroscopy*, vol. 226, no. 2, pp. 196-200, Aug.2004.

[90] G. Whitenett, G. Stewart, H. B. Yu, and B. N. Culshaw, "Investigation of a tuneable mode-locked fiber laser for application to multipoint gas spectroscopy," *Journal of Lightwave Technology*, vol. 22, no. 3, pp. 813-819, Mar.2004.

[91] S. Basu, J. B. Miller, and S. Lehman, "Separation of biospheric and fossil fuel fluxes of CO2 by atmospheric inversion of CO2 and (CO2)-C-14 measurements: Observation System Simulations," *Atmospheric Chemistry and Physics*, vol. 16, no. 9, pp. 5665-5683, 2016.

[92] D. A. Burns and E. W. Ciurczak, *Handbook of near-infrared analysis*, 1st ed. New York: M. Dekker, 1992.

[93] Arsad N. and Stewart G., "Stable, tunable, and single-mode operation of an erbium-doped fibre laser system using a saturable absorber for gas spectroscopy applications,"*, SPIE 7195 ed 2009, pp. 719525-1-719525-10.

[94] T. Hansch, A. L. Schawlow, and P. Toschek, "Ultrasensitive Response of a CW Dye Laser to Selective Extinction," *Quantum Electronics, IEEE Journal of*, vol. 8, no. 10, pp. 802-804, Oct.1972.

[95] J. M. Fini, J. W. Nicholson, R. S. Windeler, E. M. Monberg, L. L. Meng, B. Mangan, A. DeSantolo, and F. V. DiMarcello, "Low-loss hollow-core fibers with improved single-modedness," *Optics Express*, vol. 21, no. 5, pp. 6233-6242, Mar.2013.

[96] M. N. Petrovich, F. Poletti, A. van Brakel, and D. J. Richardson, "Robustly single mode hollow core photonic bandgap fiber," *Optics Express*, vol. 16, no. 6, pp. 4337-4346, Mar.2008.

[97] T. P. Hansen, J. Broeng, C. Jakobsen, G. Vienne, H. R. Simonsen, M. D. Nielsen, P. M. W. Skovgaard, R. Folkenberg, and A. Bjarklev, "Air-guiding photonic bandgap fibers: Spectral properties, macrobending loss, and practical handling," *Journal of Lightwave Technology*, vol. 22, no. 1, pp. 11-15, Jan.2004.

[98] F. Benabid and P. St. J. Russell, "Hollow core photonic crystal fibers: progress and prospects," *Proceedings of SPIE: Photonic Crystal Materials and Devices III*, vol. 5733, pp. 176-189, 2005.

[99] M. N. Petrovich, F. Poletti, and D. J. Richardson, "Control of Modal Properties and Modal Effects in Air Guiding Photonic Bandgap Fibres," IEEE, 2009.

[100] J.C.Knight, J.Broeng, T.A.Birks, and P.St.J.Russell, "Photonic Band gap guidance in optical fibers," *Science*, vol. 282, pp. 1476-1478, 1998.

[101] A. Lancia, "Hollow core fiber guides as gas analysis cells for laser spectroscopy," *Optical Sensors and Microsystems: New Concepts, Materials, Technologies*, pp. 235-240, 2000.

[102] T. Ritari, H. Ludvigsen, and J. C. Petersen, "Photonic bandgap fibers in gas detection," *Spectroscopy*, vol. 20, no. 4, p. 30-+, Apr.2005.

[103] J. P. Parry, B. C. Griffiths, N. Gayraud, E. D. McNaghten, A. M. Parkes, W. N. MacPherson, and D. P. Hand, "Towards practical gas sensing with micro-structured fibres," *Measurement Science & Technology*, vol. 20, no. 7 July2009.

[104] M. N. Petrovich, A. van Brakel, F. Poletti, K. Mukasa, E. Austin, V. Finazzi, P. Petropoulos, E. O'Driscoll, M. Watson, T. DelMonte, J. P. Dakin, and D. J. Richardson, "Microstructured fibres of sensing applications," *Proceedings of SPIE: Photonic Crystals and Photonic Crystal Fibers for Sensing Applications*, vol. 6005, pp. 78-92, 2005.

[105] A. Duval, M. Lhoutellier, J. B. Jensen, P. E. Hoiby, V. Missier, L. H. Pedersen, T. P. Hansen, A. Bjarklev, and O. Bang, "Photonic crystal fiber based antibody detection," *Proceedings of IEEE: Sensors*, vol. 3, pp. 1222-1225, 2004.

[106] A. van Brakel, C. Jauregui, T. T. Ng, P. Petropoulos, J. P. Dakin, C. Grivas, M. N. Petrovich, and D. J. Richardson, "Cavity ring-down in a photonic bandgap fiber gas cell," IEEE, 2008.

[107] D. Munzke, M. Bohm, and O. Reich, "Gaseous Oxygen Detection Using Hollow-Core Fiber-Based Linear Cavity Ring-Down Spectroscopy," *Journal of Lightwave Technology*, vol. 33, no. 12, pp. 2524-2529, June2015.

[108] F. Magaelhaes, J. P. Carvalho, L. A. Ferreira, F. M. Araujo, and J. L. Santos, "Methane Detection System Based on Wavelength Modulation Spectroscopy and Hollow-Core Fibers," 2008, pp. 1277-1280.

[109] H. W. Zhang, Y. Lu, L. C. Duan, Z. Q. Zhao, W. Shi, and J. Q. Yao, "Intracavity absorption multiplexed sensor network based on dense wavelength division multiplexing filter," *Optics Express*, vol. 22, no. 20, pp. 24545-24550, Oct.2014.

[110] D. S. Bomse and M. N. Ediger, "Simultaneous detection of multiple gases by Raman spectroscopy with hollow-core fibers," 2014.

[111] I. Dicaire, J. C. Beugnot, and L. Thevenaz, "Analytical modeling of the gas-filling dynamics in photonic crystal fibers," *Applied Optics*, vol. 49, no. 24, pp. 4604-4609, Aug.2010.

[112] Y. L. Hoo, W. Jin, H. L. Ho, J. Ju, and D. N. Wang, "Gas diffusion measurement using hollow-core photonic bandgap fiber," *Sensors and Actuators B-Chemical*, vol. 105, no. 2, pp. 183-186, Mar.2005.

[113] I. Dicaire, J. C. Beugnot, and L. Thevenaz, "Optimized conditions for gas light interaction in photonic crystal fibres,"*, 7653 ed 2010, p. 76530L.

[114] M. Amanzadeh, E. Sheridan, S. M. Aminossadati, M. S. Kizil, and W. P. Bowen, "Microfabricated hollow core fibres for gas sensing using wavelength modulation spectroscopy," 2013.

[115] R. Dhawan, M. M. Khan, N. Panwar, U. Tiwari, R. Bhatnagar, and S. C. Jain, "A low loss mechanical splice for gas sensing using Hollow-Core Photonic Crystal Fibre," *Optik*, vol. 124, no. 18, pp. 3671-3673, 2013.

[116] J. M. Lazaro, A. M. Cubillas, M. Silva-Lopez, O. M. Conde, M. N. Petrovich, and J. M. Lopez-Higuera, "Methane sensing using multiple-coupling gaps in hollow-core photonic bandgap fibers,"*, 7004 ed 2008.

[117] S. H. Kassani, J. Park, Y. Jung, J. Kobelke, and K. Oh, "Fast response in-line gas sensor using C-type fiber and Ge-doped ring defect photonic crystal fiber," *Optics Express*, vol. 21, no. 12, pp. 14074-14083, June2013.

[118] E. J. Bateman and E. M. Baggs, "Contributions of nitrification and denitrification to N2O emissions from soils at different water-filled pore space," *Biology and Fertility of Soils*, vol. 41, no. 6, pp. 379-388, Aug.2005.

[119] A. Vallejo, U. M. Skiba, L. Garcia-Torres, A. Arce, S. Lopez-Fernandez, and L. Sanchez-Martin, "Nitrogen oxides emission from soils bearing a potato crop as influenced by fertilization with treated pig slurries and composts," *Soil Biology & Biochemistry*, vol. 38, no. 9, pp. 2782-2793, Sept.2006.

[120] A. F. Bouwman, "Direct emission of nitrous oxide from agricultural soils," *Nutrient Cycling in Agroecosystems*, vol. 46, no. 1, pp. 53-70, 1996.

[121] M. J. Eichner, "Nitrous-Oxide Emissions from Fertilized Soils - Summary of Available Data," *Journal of Environmental Quality*, vol. 19, no. 2, pp. 272-280, Apr.1990.

[122] M. Maier and H. Schack-Kirchner, "Using the gradient method to determine soil gas flux: A review," *Agricultural and Forest Meteorology*, vol. 192, pp. 78-95, July2014.

[123] X. Lee, W. Massman, and B. Law, *Handbook of Micrometeorology: A Guide for Surface Flux Measurement and Analysis* Springer Netherlands, 2005.

[124] A. J. Glenn, M. Tenuta, B. D. Amiro, S. E. Maas, and C. Wagner-Riddle, "Nitrous oxide emissions from an annual crop rotation on poorly drained soil on the Canadian Prairies," *Agricultural and Forest Meteorology*, vol. 166, pp. 41-49, Dec.2012.

[125] M. K. D. Hall, A. J. Winters, and G. S. Rogers, "Variations in the Diurnal Flux of Greenhouse Gases from Soil and Optimizing the Sampling Protocol for Closed Static Chambers," *Communications in Soil Science and Plant Analysis*, vol. 45, no. 22, pp. 2970-2978, Dec.2014.

[126] G. Borjesson, A. Danielsson, and B. H. Svensson, "Methane fluxes from a Swedish landfill determined by geostatistical treatment of static chamber measurements," *Environmental Science & Technology*, vol. 34, no. 18, pp. 4044-4050, Sept.2000.

[127] S. M. Collier, M. D. Ruark, L. G. Oates, W. E. Jokela, and C. J. Dell, "Measurement of Greenhouse Gas Flux from Agricultural Soils Using Static Chambers," *Jove-Journal of Visualized Experiments*, no. 90 Aug.2014.

[128] P. Rochette, "Towards a standard non-steady-state chamber methodology for measuring soil N2O emissions," *Animal Feed Science and Technology*, vol. 166-67, pp. 141-146, June2011.

[129] J. R. Christiansen, J. F. J. Korhonen, R. Juszczak, M. Giebels, and M. Pihlatie, "Assessing the effects of chamber placement, manual sampling and headspace mixing on CH4 fluxes in a laboratory experiment," *Plant and Soil*, vol. 343, no. 1-2, pp. 171-185, June2011.

[130] B. J. R. Alves, K. A. Smith, R. A. Flores, A. S. Cardoso, W. R. D. Oliveira, C. P. Jantalia, S. Urquiaga, and R. M. Boddey, "Selection of the most suitable sampling time for static chambers for the estimation of daily mean N2O flux from soils," *Soil Biology & Biochemistry*, vol. 46, pp. 129-135, Mar.2012.